

BACTERIUM *E. COLI*- AND PHAGE P22-TEMPLATED SYNTHESIS OF  
SEMICONDUCTOR NANOSTRUCTURES

by

LIMING SHEN

A DISSERTATION

Submitted in partial fulfillment of the requirements  
for the degree of Doctor of Philosophy  
in Materials Science  
in the Graduate School of  
The University of Alabama

TUSCALOOSA, ALABAMA

2010

Copyright Liming Shen 2010  
ALL RIGHTS RESERVED

## ABSTRACT

The properties of inorganic materials in the nanoscale are found to be size- and shape-dependent due to quantum confinement effects, and thereby nanomaterials possess properties very different from those of single molecules as well as those of bulk materials. Assembling monodispersed nanoparticles into highly ordered hierarchical architectures is expected to generate novel collective properties for potential applications in catalysis, energy, biomedicine, etc. The major challenge in the assembly of nanoparticles lies in the development of controllable synthetic strategies that enable the growth and assembly of nanoparticles with high selectivity and good controllability. Biological matter possesses robust and precisely ordered structures that exist in a large variety of shapes and sizes, providing an ideal platform for synthesizing high-performance nanostructures.

The primary goal of this thesis work has been to develop rational synthetic strategies for high-performance nanostructured materials using biological templates, which are difficult to achieve through traditional chemical synthetic methods. These approaches can serve as general bio-inspired approaches for synthesizing nanoparticle assemblies with desired components and architectures.

CdS- and TiO<sub>2</sub>-binding peptides have been identified using phage display biopanning technique and the mechanism behind the specific affinity between the selected peptides and inorganic substrates are analyzed. The ZnS- and CdS-binding peptides, identified by the phage display biopanning, are utilized for the selective nucleation and growth of sulfides over self-assembled genetically engineered P22 coat proteins, resulting in ordered nanostructures of

sulfide nanocrystal assemblies. The synthetic strategy can be extended to the fabrication of a variety of other nanostructures.

A simple sonochemical route for the synthesis and assembly of CdS nanostructures with high yield under ambient conditions has been developed by exploiting the chemical characteristics and structure of permeabilized *E. coli* bacteria. The crystal phase, morphology, micro/nanostructure, optical absorption, and photocatalytic properties of the CdS nanostructures are tailored over a wide range by merely changing the synthetic conditions. Photoanodes fabricated using the nanoporous hollow CdS microrods exhibit excellent performance for the photocatalytic hydrogen production. This facile approach has been extended to the synthesis and assembly of other semiconducting sulfides, including PbS, ZnS, and HgS.

## LIST OF ABBREVIATIONS AND SYMBOLS

<i>M</i>	Magnetization
<i>H</i>	Magnetic field
$E_{el}$	Electrostatic energy
<i>C</i>	Capacitance
$k_B T$	Thermal Energy
<i>CIGS</i>	Copper indium gallium selenide
<i>MRI</i>	Magnetic resonance imaging
<i>QD</i>	Quantum dots
<i>E. coli</i>	<i>Escherichia coli</i>
<i>CCMV</i>	Cowpea chlorotic mottle virus
<i>TMV</i>	Tobacco mosaic virus
<i>DNA</i>	Deoxyribonucleic acid
<i>RNA</i>	Ribonucleic acid
<i>IPTG</i>	Isopropyl $\beta$ -D-1-thiogalactopyranoside
<i>EDTA</i>	Ethylenediaminetetraacetic acid
<i>SEM</i>	Scanning electron microscopy
<i>EDS</i>	Energy-dispersive X-ray spectroscopy
<i>HRTEM</i>	Transmission electron microscopy coupled with high resolution
<i>CLSM</i>	Confocal laser scanning fluorescence microscopy
<i>XRD</i>	X-ray diffraction
<i>UV-Vis</i>	Ultraviolet-visible spectroscopy

<i>d</i>	Interplanar distance
$\lambda$	Wavelength
<i>FWHM</i>	Full width at half maximum intensity of the peak
<i>OD</i>	Optical density
<i>ITO</i>	Indium tin oxide
<i>AM 1.5</i>	Air mass 1.5
<i>A</i>	Alanine
<i>R</i>	Arginine
<i>N</i>	Asparagine
<i>D</i>	Aspartic acid
<i>C</i>	Cysteine
<i>E</i>	Glutamic acid
<i>Q</i>	Glutamine
<i>G</i>	Glycine
<i>H</i>	Histidine
<i>I</i>	Isoleucine
<i>L</i>	Leucine
<i>K</i>	Lysine
<i>M</i>	Methionine
<i>F</i>	Phenylalanine
<i>P</i>	Proline
<i>S</i>	Serine
<i>T</i>	Threonine

<i>W</i>	Tryptophan
<i>Y</i>	Tyrosine
<i>V</i>	Valine
<i>CFU</i>	Colony-forming unit
<i>K<sub>sp</sub></i>	Solubility product constant

## ACKNOWLEDGMENTS

I am pleased to have this opportunity to thank the faculty members and colleagues who have helped me with this research project. My deepest gratitude goes to Professor Arunava Gupta, my supervisor, for his wise guidance, considerable patience, and constant encouragement. Without his expert instruction in research and English writing, my dissertation could not have reached the present form.

I am also greatly indebted to Professor Peter E. Prevelige Jr. of The University of Alabama at Birmingham for his consistent guidance and assistance in the biological work and Professor Ningzhong Bao at the Nanjing University of Technology for his assistance in the photoelectrochemical analysis and invaluable discussions.

Many thanks to all of my committee members, Professor Gregg J. Janowski, Professor Gregory Thompson, Professor Martin G. Bakker, and Professor Yuping Bao, for their valuable input and inspiring questions.

I would also like to thank my friends and colleagues who listened to me and provided help whenever I had difficulty during the past five years.

This research would not have been possible without the support of my family who never stopped encouraging me to persist. I specially thank Will and Annie; their innocent smiles brightened me at hard times.

Finally I thank the Tricampus Material Science Ph.D. Program at The University of Alabama and all of the faculty members who instructed me in the courses.

## CONTENTS

ABSTRACT.....	ii
LIST OF ABBREVIATIONS AND SYMBOLS .....	iv
ACKNOWLEDGMENTS .....	vii
LIST OF TABLES .....	xii
LIST OF FIGURES .....	xiii
1. INTRODUCTION .....	1
1.1 Properties of Nanomaterials.....	4
1.1.1 Optical Properties.....	4
1.1.2 Electrical Properties .....	6
1.1.3 Magnetic Properties .....	7
1.2 Applications of Nanomaterials .....	9
1.2.1 Catalysis.....	9
1.2.2 Energy .....	11
1.2.3 Nanodevices.....	13
1.2.4 Biotechnology .....	14
1.3 Synthetic Methods of Nanomaterials.....	16
1.3.1 Solution Methods.....	17
1.3.1.1 Coprecipitation.....	17
1.3.1.2 Microemulsion .....	18
1.3.1.3 Thermal Decomposition Method .....	19
1.3.1.4 Hydrothermal/Solvothermal Synthesis .....	20

1.3.2 Templating Methods .....	21
1.3.2.1 Inorganic Hard Templates.....	21
1.3.2.2 Organic Soft Templates .....	22
1.3.3 Biological Synthetic Methods.....	23
1.3.3.1 Biomolecules.....	24
1.3.3.2 Microorganisms .....	25
1.3.3.3 Viruses .....	26
1.4 Research Objective .....	27
1.5 References.....	28
<b>2. EXPERIMENTAL TECHNIQUES.....</b>	<b>33</b>
2.1 Preparation of Biotemplates.....	33
2.2 General Synthetic Procedure of Bio-Templated CdS and ZnS Nanostructures .....	35
2.3 Scanning Electron Microscopy.....	36
2.4 Transmission Electron Microscopy .....	37
2.5 Confocal Laser Scanning Fluorescence Microscopy .....	39
2.6 X-Ray Powder Diffraction.....	41
2.7 Ultraviolet-Visible Spectroscopy.....	42
2.8 Photoelectrochemical Cell .....	43
2.9 References.....	44
<b>3. PEPTIDE SELECTION USING PHAGE DISPLAY BIOPANNING AND FABRICATION OF ORDERED NANOSTRUCTURES OF SULFIDE NANOCRYSTAL ASSEMBLIES OVER SELF-ASSEMBLED GENETICALLY ENGINEERED P22 COAT PROTEIN.....</b>	<b>45</b>
3.1 Introduction.....	45

3.2 Peptide Selection Using Phage Display Biopanning .....	47
3.2.1 Experimental .....	49
3.2.1.1 Materials .....	49
3.2.1.2 Preparation of Inorganic Substrates .....	50
3.2.1.3 Peptide Selection.....	50
3.2.1.4 Affinity Assay.....	51
3.2.1.5 Genetically Engineering Main Coat Protein of M13 Phage ....	51
3.2.1.6 Synthesis of CdS Nanowires on Genetically Engineered M13 Phage.....	52
3.2.2 Results and Discussion .....	52
3.2.3 Conclusion .....	61
3.3 Fabrication of Ordered Nanostructures of Sulfide Nanocrystal Assemblies over Self-Assembled Genetically Engineered P22 Coat Protein.....	62
3.3.1 Experimental .....	63
3.3.1.1 Materials .....	63
3.3.1.2 Preparation of Genetically Engineered Bacteriophage P22 Coat Protein Assemblies.....	64
3.3.1.3 Inorganic Synthesis over Genetically Engineered Bacteriophage P22 Coat Protein Assemblies.....	64
3.3.2 Results and Discussion .....	65
3.3.3 Conclusion .....	75
3.4 References.....	76
<b>4. BACTERIUM E. COLI-TEMPLATED SYNTHESIS OF NANOPOROUS CADMIUM SULFIDE HOLLOW MICRORODS FOR EFFICIENT PHOTOCATALYTIC HYDROGEN PRODUCTION .....</b>	<b>80</b>
4.1 Introduction.....	80

4.2 Experimental .....	84
4.2.1 Preparation of Cells.....	84
4.2.2 Synthesis of CdS Nanostructures.....	84
4.2.3 Characterization of Materials.....	85
4.2.4 Photoelectrochemical Characterization .....	85
4.3 Results and Discussion .....	86
4.4 Conclusion .....	99
4.5 References.....	100
5. SUMMARY AND FUTURE PLAN .....	103

## LIST OF TABLES

3.1 CdS-specific peptide sequences after three rounds (R3) of biopanning.....	56
3.2 CdS-specific peptide sequences after five rounds (R5) of biopanning.....	56
3.3 TiO <sub>2</sub> (110)-specific peptide sequences after five rounds (R5) of biopanning. The peptide sequence in Clone 1 was observed in 13 clones.....	58
3.4 TiO <sub>2</sub> (100)-specific peptide sequences after five rounds (R5) of biopanning. The peptide sequence in Clone 4 was observed in 10 clones.....	58

## LIST OF FIGURES

1.1	The percentage of surface atom changes with the diameter of palladium clusters.....	3
1.2	Relationship between the melting points and the sizes of gold .....	3
1.3	Optical spectra of samples consisting of CdS nanocrystals with different mean diameters (Å): (a) 6.4, (b) 7.2, (c) 8.0, (d) 9.3, (e) 11.6, (f) 19.4, (g) 28, and (h) 48. The excitonic transition shifts to higher energy values along with an increase in the molar absorption coefficient, as the particle size decrease .....	5
1.4	A Coulomb staircase measured at room temperature, from a chip fabricated using ~10-nm gold colloid .....	6
1.5	(a) Temperature dependence of the magnetization measured after zero- field cooling (ZFC) and field cooling (FC) at 100 Oe for 4, 6, 8, 9, 11, 12, 13, and 15 nm particles. (b) Size dependence of the blocking temperature, $T_B$ , obtained from $M(T)$ in Figure 1.5a .....	8
1.6	Shape-dependent catalytic activity. TEM images, shape distributions, and Arrhenius plots obtained with dominantly tetrahedral (a-b), cubic (c-d), and spherical (e-f) platinum nanoparticles. It is observed that the tetrahedral platinum nanoparticles have the lowest activation energy, the cubic platinum nanoparticles have the highest activation energy, and the spherical platinum nanoparticles have an intermediate activation energy .....	10
1.7	(a) Schematics and (b) corresponding SEM images of device fabrication of p(core)-i(shell)-n(shell) nanostructures. Scale bars in b are 100 nm (left), 200 nm (middle), and 1.5 mm (right). (c) Dark I–V curves of a p-i-n device with contacts on core–core, shell–shell, and different core–shell combinations. (d) Semi-log scale I–V curves of p-i-n and p-n diodes.....	12
1.8	Quantum dot and solid-state dopant qubits. (a) An electrostatically confined quantum dot; the structure shown is several mm across. 2DEG: two-dimensional electron gas. (b) A self-assembled quantum dot. Scale bar is 5 nm .....	14
1.9	(a) Schematic representation of the preparation of QDs with a paramagnetic micellular coating. (b) Fluorescence microscopy of HUVEC incubated with RGD-pQDs and bare pQDs. (c) T1-weighted image of cells that were incubated with RGD-pQDs, pQDs, or without contrast agent.....	16
2.1	Interactions between electrons and a sample .....	37

2.2 A schematic diagram of a transmission electron microscope .....	38
2.3 Ray path in a confocal laser scanning microscope .....	40
2.4 Schematic demonstration of the measurement of the optical density on a spectrophotometer .....	43
3.1 (a) Schematic bacteriophage M13 and (b) biopanning with phage display peptide library .....	48
3.2 Schematic affinity assay .....	53
3.3 Confocal fluorescent microscope images of (a) a glass slide and (b-d) a CdS substrate treated with selected phages and antibodies .....	54
3.4 Schemes of (a) the wurtzite CdS and (b) the interaction between CdS substrate and amino acids with positively charged R groups. ....	57
3.5 Schemes of the interaction between the hydroxyl groups on the TiO <sub>2</sub> substrate and the amino acids with polar side chains .....	59
3.6 TEM images of (a) filamentous bacteriophage stained by 2 % uranyl acetate. (b) CdS nanowires grown on the engineered phage; insert: one single nanowire. (c) CdS agglomerates obtained in the presence of wild phage. (d) CdS nanoparticles obtained in the absence of any type of phage .....	61
3.7 (a) Assembly pathway of bacteriophage P22 showing the proteins involved and the nucleation, elongation and maturation reactions. (b) Structural transformation of empty P22 procapsid .....	63
3.8 (a) Three-dimensional surface representation of P22 procapsid viewed along a 3-fold axis; (b) TEM image of stained protein assemblies of genetically engineered P22 coat protein; (c) Schematic illustration of the formation of ordered nanocrystal assemblies over self-assembled genetically engineered P22 coat proteins. Step 1: assembly of P22 coat proteins (gray) genetically engineered with specific peptide (red). Step 2: protein-directed nucleation and growth of nanocrystals (yellow) on the protein assembly. (d, e) Sulfide nanocrystal assemblies grown on the self-assembled protein templates shown in Figure 3.8b. All scale bars represent 50 nm .....	67
3.9 (a) TEM image of two connected ZnS nanostructures formed after 2 h; magnified TEM images of (b) the bottom-left and (c) the top-right nanostructures shown in Figure 3.9a. Protein-templated nanocrystal subunits are marked in red. All scale bars represent 20 nm .....	69

3.10 (a) TEM image of a spherical ZnS nanostructure and (b) HRTEM image of one crystal subunit; (c) Simulated structure of P22 coat protein assembly generated by PyMOL molecular visualization system, showing protein residue 182. The red dots indicate the center of the hexamers and pentamers. (d) Superimposed simulated structure of Figure 3.10c on synthesized ZnS nanostructure. The scale bar in Figure 3.10a and 3.10d represents 10 nm.....	70
3.11 (a) Two-dimensional projection of a simulated P22 coat protein assembly generated by PyMOL molecular visualization system, only showing the individual protein residue 182 as a white dot. The red dots indicate the center of the hexamers and pentamers. (b) Matching (a) with a ZnS nanostructure. The scale bar represents 10 nm.....	71
3.12 (a-c) TEM and (d) HRTEM images of nearly monodisperse CdS nanocrystal assemblies formed over genetically engineered P22 coat protein assemblies after a short reaction time of 2 hours at a low reactant concentration (1 mM) .....	72
3.13 (a) Two-dimensional projection of a simulated P22 coat protein assembly generated by PyMOL molecular visualization system, only showing the individual protein residue 182 as a white dot. The red dots indicate the center of the hexamers and pentamers. (b) Matching (a) with a CdS nanostructure. The scale bar represents 10 nm.....	72
3.14 TEM images of nearly monodisperse CdS nanocrystal assemblies formed over genetically engineered P22 coat protein assemblies after a longer reaction time of 5 hours at the low reactant concentration .....	73
3.15 TEM images of nearly monodisperse spherical hollow nanostructures of CdS nanocrystals assembled over genetically engineered P22 coat protein assemblies after an even longer reaction time of 12 hours and at a higher reactant concentration (2 mM).....	74
3.16 TEM images of nearly monodisperse ZnS nanocrystal assemblies formed over genetically engineered P22 coat protein assemblies after a short reaction time of 2 hours .....	74
3.17 TEM images of nearly monodisperse spherical hollow nanostructures of ZnS nanocrystals assembled over genetically engineered P22 coat protein assemblies after a longer reaction time of 12 hours.....	75
3.18 TEM image of (a) ZnS product prepared in the presence of wild P22 procapsids; (b) CdS product prepared in the presence of self-assembled P22 coat proteins engineered with ZnS-specific peptide; and (c) ZnS product prepared in the absence of any type of P22 coat protein .....	75

4.1 A schematic diagram illustrating the concept of <i>E. coli</i> -templated synthesis and assembly of nanoporous hollow CdS nanostructures.....	83
4.2 SEM and TEM images of <i>E. coli</i> -templated nanoporous hollow CdS microrods formed after 4 h. (a) Low-magnification and (b) high-magnification SEM images of the hollow structures showing the high yield of product with the desired shape. TEM image of hollow CdS microrods with (c) closed ends, and (d) an open end. The magnified TEM images of (e) the cross section and (f) the body of a rod-like hollow CdS structure show the uniform wall thickness and the nanoporous structure of the wall, respectively.....	88
4.3 TEM and HRTEM images of synthesized CdS nanomaterials as a function of reaction time. (a, b) Monodisperse quantum dots formed after 1 min; (c, d) nearly monodisperse nanocrystals formed after 10 min; (e) continuous nanoparticle agglomerates formed after 2 h; and (f) uniform porous coating formed after 4 h.....	89
4.4 TEM images of (a, b) crystalline CdS nanoparticles sonochemically synthesized after 4 h in the absence of <i>E. coli</i> bacteria, and CdS nanoparticles formed in the reaction solution and on the cell surface of untreated <i>E. coli</i> bacteria (c) after 1 min and (d) 2 h .....	90
4.5 TEM and HRTEM image of nanoporous hollow CdS microrod-supported nanorods synthesized after 4 h using <i>E. coli</i> with pili as templates. (a, b) Low-magnification and (c) high-magnification TEM images of the CdS nanostructures show the morphology and structure of the whole CdS assembly, the basic hollow microrod, and the attached nanorods. (d) HRTEM image of the CdS nanorods showing crystal lattice fringes.....	92
4.6 Optical images and UV-Vis spectra of <i>E. coli</i> -templated CdS nanostructures in solution after (a) 0 min, (b) 1 min, (c) 10 min, (d) 2 h, and (e) 4 h of reaction .....	93
4.7 XRD patterns of <i>E. coli</i> -templated CdS nanostructures with (a) hexagonal, (b) mixture of hexagonal and cubic CdS nanocrystals, and (c) cubic phase structures, obtained with decreasing sulfur/cadmium molar ratio from 2.5, 1 and 0.25, respectively .....	95
4.8 (a) Low-magnification and (b) high-magnification SEM images of <i>E. coli</i> -templated hollow CdS microrods after annealing at 300 °C for 0.5 h .....	97
4.9 (a) Photocurrent density, (b) dark current, and corresponding photoconversion efficiency (the inset) of a photoelectrode fabricated using <i>E. coli</i> -templated nanoporous CdS hollow microrods with the hexagonal phase structure .....	98

4.10 XRD patterns and TEM images of <i>E. coli</i> -templated nanoporous hollow microrods of (a) PbS, (b) HgS, and (c) ZnS sonochemically synthesized after 4 h of reaction .....	99
5.1 A schematic core-shell nanostructure grown over the genetically modified P22 procapsid .....	106
5.2 (a) Monolayered and (b) multilayered films of the core-shell nanostructures grown over the genetically modified P22 procapsid.....	107

# CHAPTER 1

## INTRODUCTION

A primary focus of nanomaterials research is the development of rational synthetic strategies for the design of nanomaterials with desired properties targeted towards various applications in catalysis, energy, device fabrication, biology, biomedicine, etc.<sup>1-5</sup> Nanomaterials refer to materials having a characteristic length scale with at least one dimension in the nanometer length scale, typically 1-100 nm. As the size of the materials decreases to the nanometer scale, the percentage of atoms located on the surface increases very rapidly.<sup>6</sup> For example, the percentage of surface atoms in 63  $\mu\text{m}$  palladium clusters is near 0 %, as shown in Figure 1.1. However, the percentage dramatically increases to 76 % as the diameter of the clusters decreases to 1.2 nm. The surface atoms, as compared to the atoms in the bulk, exhibit significantly altered properties in terms of relative orientation, interaction, and electronic structure. As a result, the properties of nanomaterials, such as their mechanical, electrical, optical, and magnetic properties can be very different from those of single molecules as well as those of bulk materials that can be considered to be essentially infinite.<sup>7-9</sup>

Assembly of nanoparticles has been shown to be one of the most effective methods for the formation of nanostructures. A variety of nanostructures have been fabricated in the form of nanowires, nanotubes, hollow nanoparticles, and complex nanoarchitectures.<sup>10-12</sup> Compared to spherical nanoparticles, those that are shape-controlled, particularly ordered architectures of assembled nanoparticles, have exhibited novel properties and enhanced performance. For example, the electron migration rate within nanowire arrays is estimated to be several orders of magnitude higher than that of nanoparticle agglomerates, which result in enhanced solar energy

conversion efficiency in solar cell applications.<sup>13</sup> However, it is challenging to simultaneously control the synthesis and assembly of building blocks in the nanometer-scale. Nanoparticles and nanomaterials possess very large surface energy due to the large number of coordinatively unsaturated atoms exposed on their surface. As a consequence there is a depression in the melting point, enough to melt stepped surfaces with high-energy edge and corner atoms. Accordingly, nanomaterials tend to form a spherical structure during synthesis. It is reasonable that smaller the nanoparticle, the larger the contribution made by the surface energy to the overall energy of the system, and thereby the more dramatic the melting temperature depression.<sup>14</sup> The decrease in melting temperature can be of the order of tens to hundreds of degrees for metals with nanometer dimensions, as seen in Figure 1.2.<sup>15</sup> To prevent the nanomaterials from further growth and minimize the surface energy, surface protection has to be considered for maintaining the size, shape, and structure. This normally results in the formation of monodisperse single crystalline nanocrystals with simple shapes, instead of formation of complex structures and architectures. Therefore, the fabrication of ordered nanoparticle assemblies with desired components and architectures remains a great challenge.

The primary goal of this thesis has been to develop rational biological synthetic strategies for designing nanostructured materials with desired properties, in particular controlled crystalline phases and assembled architectures, which are difficult to achieve through traditional chemical synthetic methods. Before getting into the details of our research work, we will briefly introduce the general aspects of the properties, applications, and methods of synthesizing nanoparticles.

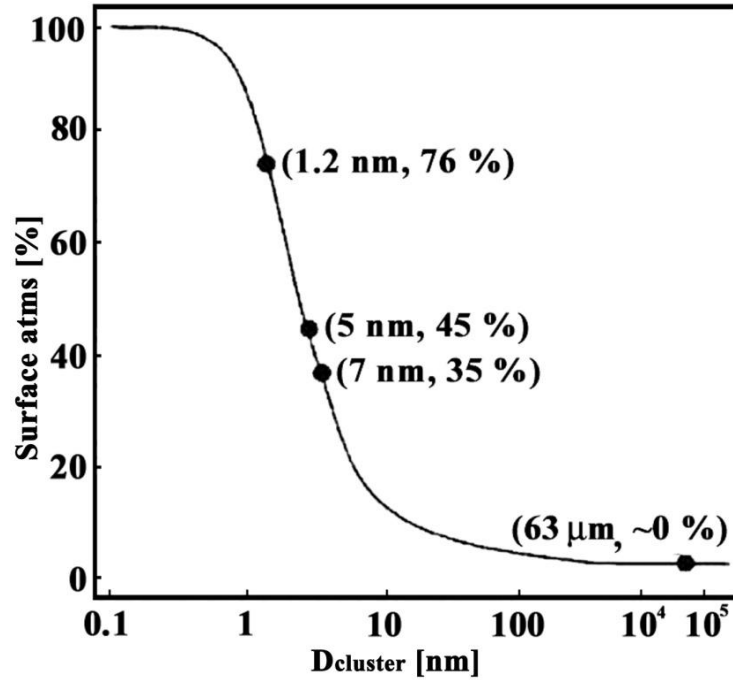


**Figure 1.1** The percentage of surface atom changes with the diameter of palladium clusters. Reproduced with permission from ref. 6.

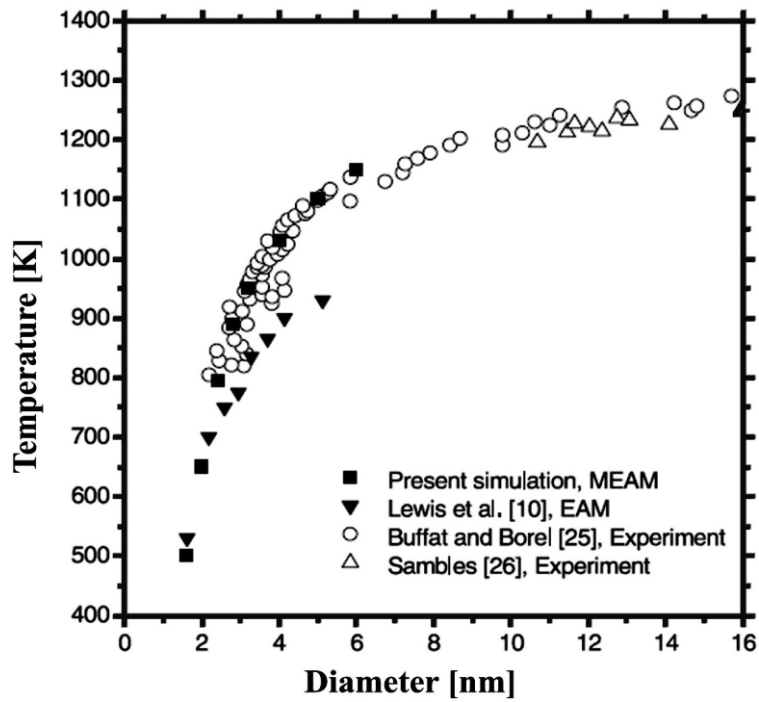


**Figure 1.2** Relationship between the melting points and the sizes of gold. Reproduced with permission from ref. 15.

## **1.1 Properties of Nanomaterials**

As the size of materials decreases to nanometer length scale, their basic properties such as optical, electrical, and magnetic properties can significantly differ from that in the bulk and is strongly dependent on the composition, size, shape, and self-assembly structures.<sup>7-9</sup>

### **1.1.1 Optical Properties**

The unique optical properties of very small metal particles were first discovered in the 1850's by Michael Faraday who found the color of gold colloids changing from gold to blue, purple, and ruby red upon decreasing the particle size.<sup>16</sup> Such intensive visible adsorption is not observed in bulk gold. Gustav Mie explained the phenomena in 1908 by developing the theory of localized surface plasmon resonance, the collective oscillation of free electrons as a consequence of incident electromagnetic radiation polarizing the metallic spheres embedded in a dielectric matrix.<sup>17,18</sup> Recently, the absorption and scattering properties of gold nanospheres and non-spherical nanostructures (silica-gold nanoshells and gold nanorods) have been calculated using Mie's theory and the discrete dipole approximation method. The calculated spectra clearly reflect the well-known dependence of the optical properties, including the resonance wavelength, the extinction cross-section, and the ratio of scattering to absorption, on the size of the nanoparticles.<sup>19</sup>

Similar optical absorption changes have been observed for a wide variety of semiconductor nanomaterials.<sup>9</sup> For semiconductor nanoparticles, the color variation is caused by the changes in the bandgap between the conduction band and the valence band. When the size of the semiconductor particles becomes smaller than their exciton Bohr radius (the average distance that the electron spends away from the hole/nucleus), the energy spectrum turns discrete along

with widening of the bandgap as the particle size decreases. As a result, the corresponding absorption band progressively blue-shifts and becomes sharper, which can be observed in the optical absorption spectrum. As an example of quantum size effects, Figure 1.3 shows the optical spectra of CdS nanocrystals with different and well-defined size distributions. With decreasing the size of CdS nanocrystals, the excitonic peak shifts to higher energies along with an increase in the molar absorption coefficient.<sup>20</sup>

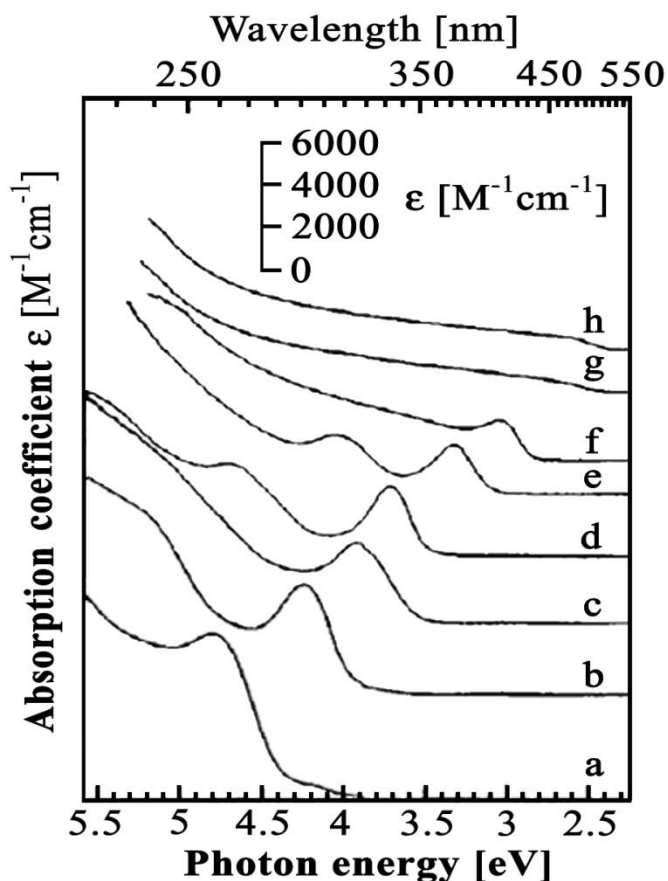


**Figure 1.3** Optical spectra of samples consisting of CdS nanocrystals with different mean diameters (Å): (a) 6.4, (b) 7.2, (c) 8.0, (d) 9.3, (e) 11.6, (f) 19.4, (g) 28, and (h) 48. The excitonic transition shifts to higher energy values along with an increase in the molar absorption coefficient, as the particle size decreases. Reproduced with permission from ref. 18.

### 1.1.2 Electrical Properties

In bulk metals, the  $I$ - $V$  (current-voltage) curve exhibits a linear dependence because electrons can drift freely through the continuous energy bands in metals. This behavior changes as the energy band turns to discrete, which is normally caused by a decrease in the particle size. When the particles decrease below a critical size, they are no longer electrically conducting, which is termed as “size-induced metal-insulator transition”.<sup>21</sup> In nanoscale metal particles, the electron-transfer process is different from that in bulk. One electron can be either incorporated into a nanoparticle or removed away by single electron transfer steps when the Coulomb energy of the particle is compensated by an external voltage. Over a range of bias voltage, the repetition of this single electron transfer process appears as the Coulomb staircase, as shown in Figure 1.4.<sup>21</sup>

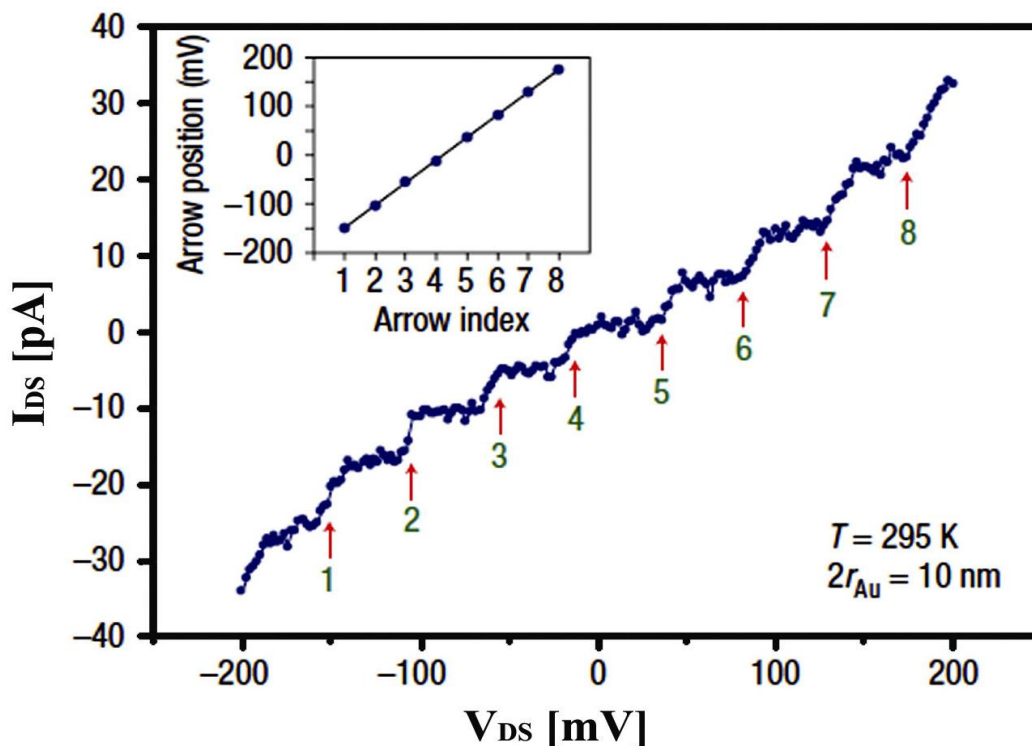


**Figure 1.4** A Coulomb staircase measured at room temperature, from a chip fabricated using ~10- nm gold colloid. Reproduced with permission from ref. 22.

The electrostatic energy ( $E_{el}$ ) required to incorporate an electron into a nanoparticle (or to remove an electron) can be quantified by the equation:  $E_{el} = e^2/2C$ , where  $e$  is the charge of the electron ( $1.6 \times 10^{-19}$  coulomb) and  $C$  is the effective capacitance of the particle. The capacitance changes with the particle size. When  $E_{el}$  becomes greater than the thermal energy ( $k_B T$ ), excess charge will accumulate on the nanoparticle. Metal nanoparticles can thus function as a tunnel junction (a thin insulating barrier between two conducting electrodes) with the electrical resistance exponentially dependent on the barrier thickness. At low temperatures, an increase of the device resistance at small bias voltages will occur (the resistance increases to infinity at zero bias), which is known as the Coulomb blockade.<sup>23</sup>

### 1.1.3 Magnetic Properties

Large magnetic particles display multidomain structure with individual domains separated by domain walls (Bloch walls). The formation of domain walls is a process driven by the balance between the magnetostatic energy (the interaction of the magnetic field created by the magnetization in some part of the sample on other parts of the same sample and thus determined by the volume of the material) and the domain-wall energy (the difference between the magnetic moments before and after the domain wall is created and determined by the interfacial area of domains).<sup>24</sup> Multiple domains exist in large magnetic particles with spins re-orientating from  $0^\circ$  to  $180^\circ$  between two domains through the domain walls. When the particle size is of the same magnitude as the domain size or below this critical size, it costs more energy to create a domain wall than to support the external magnetostatic energy of the single-domain state. As a result, the particle can only accommodate a single domain. Such single-domain particles possess a large magnetic moment because all the spins are uniformly aligned in the same direction and behave

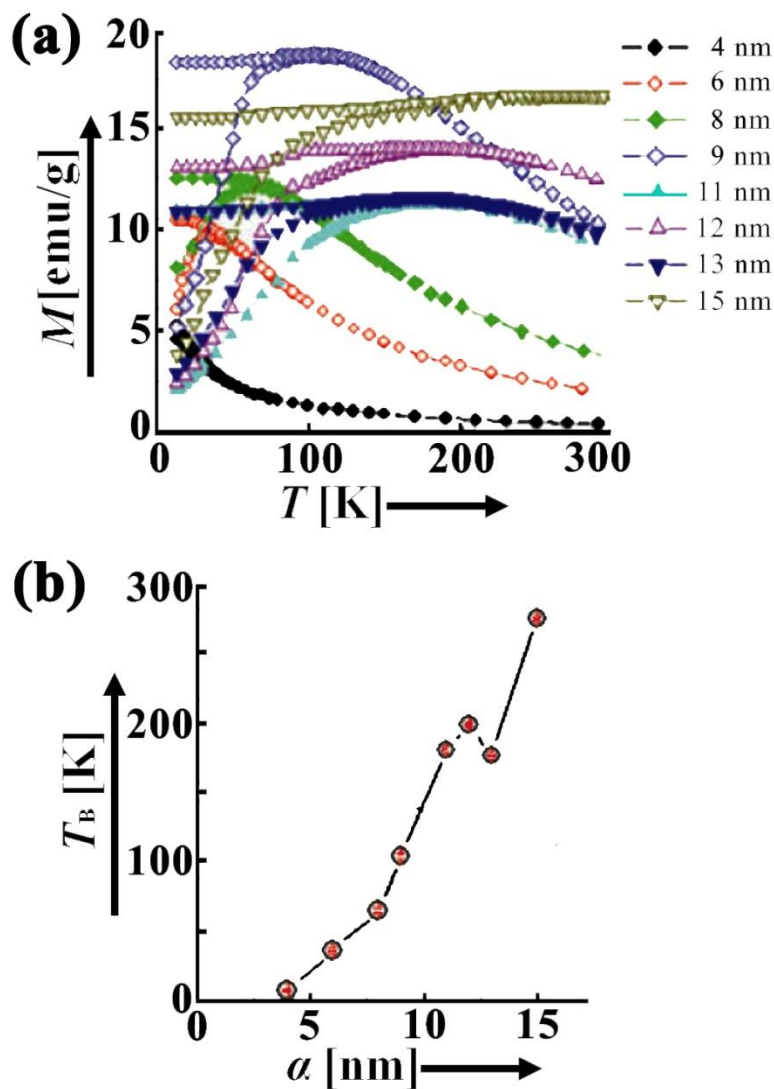


**Figure 1.5** (a) Temperature dependence of the magnetization measured after zero-field cooling (ZFC) and field cooling (FC) at 100 Oe for 4, 6, 8, 9, 11, 12, 13, and 15 nm particles. (b) Size dependence of the blocking temperature,  $T_B$ , obtained from  $M(T)$  in Figure 1.5a. Reproduced with permission from ref. 26.

like a giant paramagnetic atom that can respond rapidly to an applied magnetic field, with negligible remanent magnetism and coercivity.<sup>25</sup> Such superparamagnetic behavior disappears when the temperature is below the blocking temperature (the temperature below which the relaxation of the magnetisation becomes slow), and ferromagnetism sets in. The blocking temperature is dependent on the size of nanoparticles, as seen in Figure 1.5.<sup>26</sup> The critical diameter enabling the appearance of superparamagnetic behavior typically lies in the range of a

few tens of nanometers and sensitively depends on the nature of the material. For example, the critical diameter for some typical magnetic materials Fe, Ni, SmCo, and Fe<sub>3</sub>O<sub>4</sub> is found to be 5, 55, 750, and 128 nm, respectively.<sup>27</sup>

## **1.2 Applications of Nanomaterials**

The interest in nanoscale materials stems from their unprecedented size- and shape-dependent properties. A variety of novel nanostructures including nanoparticles, nanowires, nanotubes, nanocapsules, nanoporous solids, etc., have been synthesized using different techniques. These nanomaterials have the potential of revolutionizing materials design for numerous applications in the field of catalysis, energy, nanodevice, and biotechnology.

### **1.2.1 Catalysis**

The catalytic activity of inorganic materials is strongly influenced by their surface properties. Compared with bulk materials, nanostructures possess a very large surface area, which results in their ability for enhanced surface adsorption and increased number of surface active sites. Nanoparticles have been utilized in both homogeneous catalysis in solution and heterogeneous catalysis on a surface. In homogeneous catalysis, the colloidal nanoparticles are dispersed in an organic or aqueous solution, or in a solvent mixture. Hydrogenation reaction is a type of homogeneous catalysis using transition metal nanoparticles in colloidal solution. The catalytic activity of nanocatalysts has been found to be shape-dependent. Narayanan *et al.* demonstrated that the activities of platinum nanoparticles of different shapes are indeed different for the same electron-transfer reaction in colloidal solution, as shown in Figure 1.6.<sup>28</sup> The primary concerns regarding the use of nanoparticles in homogeneous catalysis include the aggregation of particles

and poor recyclability. Alternatively, nanoparticles can be supported on various substrates for easy separation, which is called heterogeneous catalysis. For example, transition metal nanoparticles on various forms of carbon substrates have been widely used in catalyzing reactions associated with direct methanol and ethanol fuel cells.<sup>29</sup>

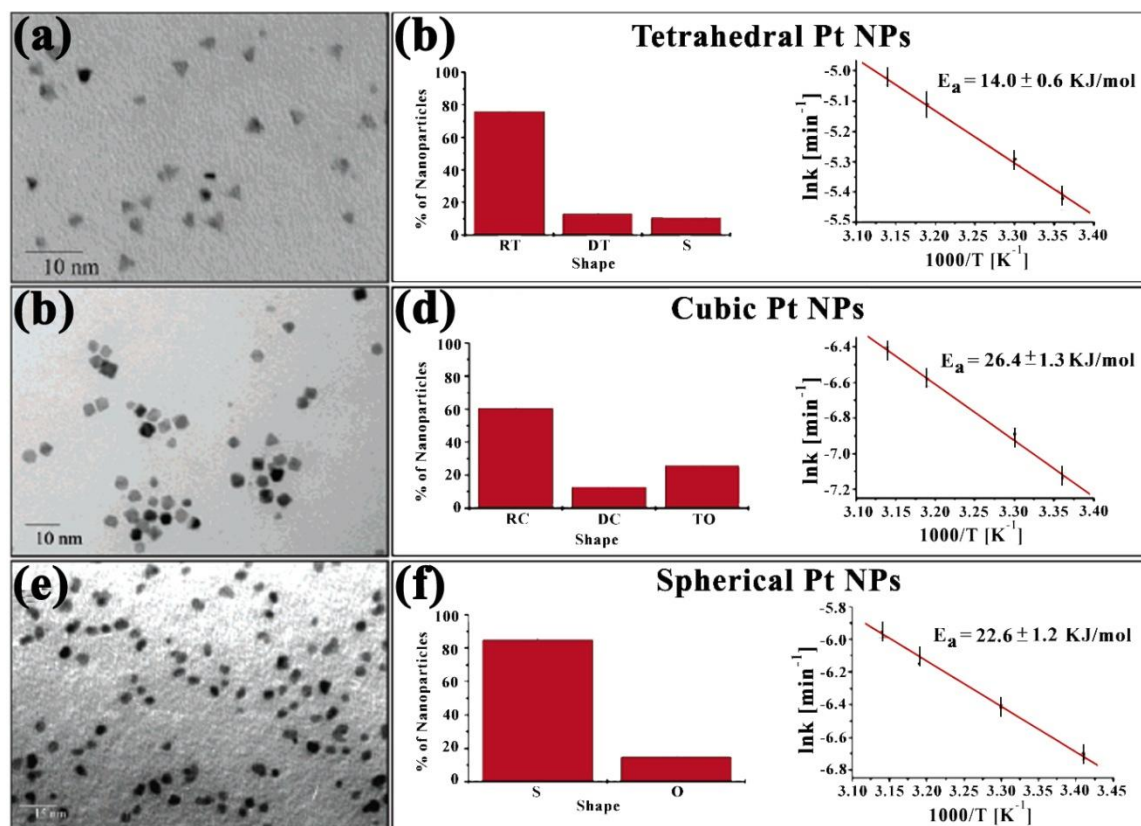


**Figure 1.6** Shape-dependent catalytic activity. TEM images, shape distributions, and Arrhenius plots obtained with dominantly tetrahedral (a-b), cubic (c-d), and spherical (e-f) platinum nanoparticles. It is observed that the tetrahedral platinum nanoparticles have the lowest activation energy, the cubic platinum nanoparticles have the highest activation energy, and the spherical platinum nanoparticles have intermediate activation energy. Reproduced with permission from ref. 28.

In addition, other forms of nanostructures have been designed for achieving enhanced catalytic activity while avoiding particle aggregation. For example, layered nanosheets produced by exfoliation of intercalated layered materials when used as solid acid catalysts exhibit

improved catalytic activity as compared to large particles due to enhanced photon absorption because of the large surface area.<sup>30</sup> Photocatalysts in the form of hollow nanostructures display significantly enhanced photocatalytic activity because the possibility of photo-induced species (photoelectrons and/or photoholes) to reach the surface is increased while reducing their bulk recombination rate, thus increasing their availability for surface reactions.<sup>31</sup>

### **1.2.2 Energy**

Considering the global warming and fossil fuel depletion, the efficient utilization of solar energy is a major goal for modern society. The use of photovoltaic solar cells is one of the methods to directly convert solar energy into electrical power. Traditional design of solar cells is based on single crystalline silicon solar cells which have the shortcomings of very high cost and limited efficiency. To improve the cell performance, a significant amount of effort has been devoted to the structural design of solar cell materials and cell structure. One method is to increase the absorption efficiency of solar radiation but at a reasonable cost. Thin-film solar cells such as amorphous silicon (a-Si),<sup>32</sup> cadmium telluride (CdTe),<sup>33</sup> copper indium gallium selenide (CIS or CIGS),<sup>34</sup> and dye-sensitized (DSC)<sup>35</sup> thin-film solar cells have been intensively investigated, which provide comparable efficiency at a decreased cost. Another method for enhancing the solar cell efficiency is to utilize the excess photon energy which is lost as heat. Calculated thermodynamic efficiency limits in single-junction solar cells (~31 %) indicate that absorption of an individual photon results in the formation of a single electron-hole pair and all of the photon energy in excess of the energy gap is lost as heat.<sup>36</sup> This limit can be bypassed via the multiple exciton generation by single-photon absorption, as observed optically in PbSe and PbS quantum dots.<sup>37</sup> In addition, novel nanostructured materials, including nanoporous films, nanowires, and

nanotubes, have been found to be useful in enhancing the cell efficiency - primarily attributed to the higher electrolyte percolation and higher charge-transfer efficiency.<sup>38-40</sup> The electron migration rate within nanowire arrays is estimated to be several orders of magnitude higher than that of nanoparticle agglomerates, which is expected to enhance the solar energy conversion efficiency. Recently, unique coaxial silicon nanowires have been developed that appear promising for fabrication of solar cells and nanoelectronic power sources, as seen in Figure 1.7.<sup>40</sup>

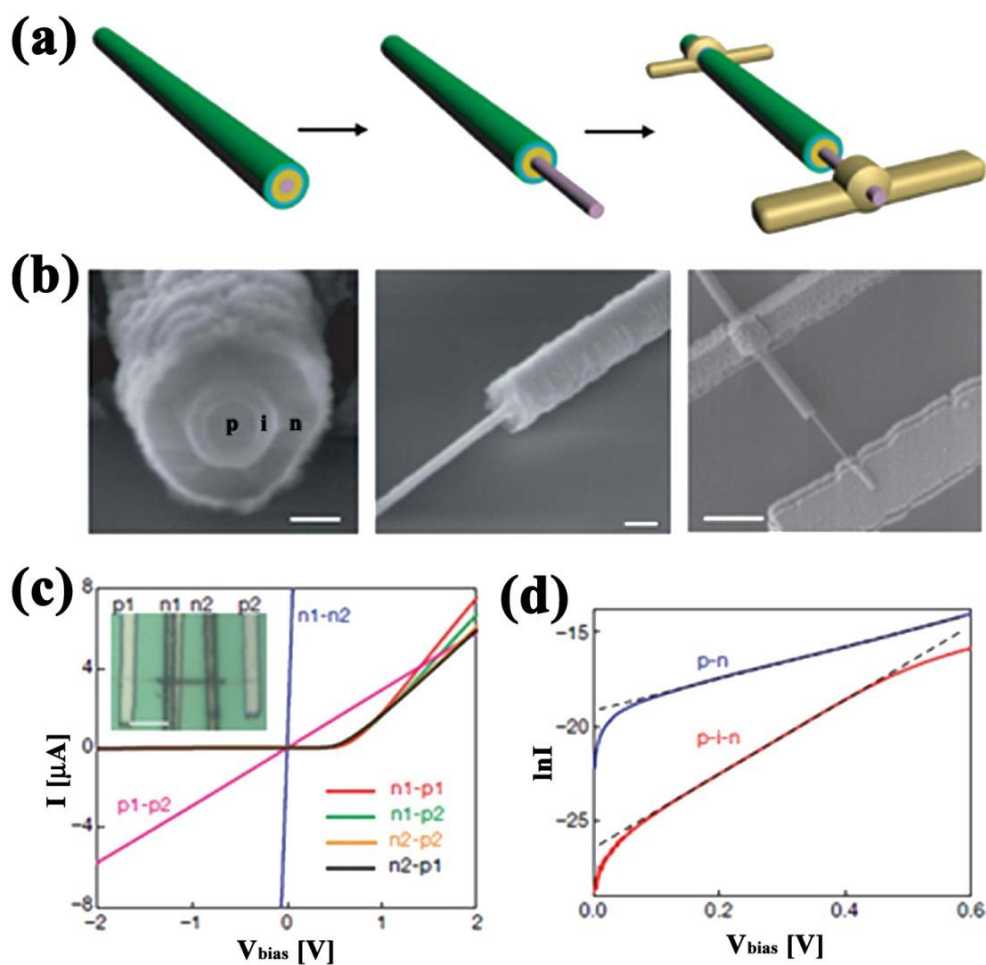


**Figure 1.7** (a) Schematics and (b) corresponding SEM images of device fabrication of p(core)-i(shell)-n(shell) nanostructures. Scale bars in b are 100 nm (left), 200 nm (middle), and 1.5 μm (right). (c) Dark I–V curves of a p–i–n device with contacts on core–core, shell–shell, and different core–shell combinations. (d) Semi-log scale I–V curves of p–i–n and p–n diodes. Reproduced with permission from ref. 40.

### 1.2.3 Nanodevices

The miniaturization of modern devices has stimulated the research interest in nanomaterials whose novel size- and shape-dependent properties have in turn propelled the development of nanodevices. For example, a variety of chemical sensors fabricated using nanomaterials have been reported, showing good performance for detecting gases, glucose, etc.<sup>41, 42</sup> Mann *et al.* arranged magnetic nanoparticles into a two-dimensional array with the aid of a cross-linked biotinylated ferritin network, which can be used in high-density magnetic storage devices.<sup>43</sup> Moreover, semiconductor materials with hierarchically porous or hollow nanostructures have shown an enhanced absorption for specific electromagnetic waves.<sup>44</sup> Although the mechanism of this phenomenon is still not clear, the potential of such nanostructured materials for electromagnetic wave shielding is proven.

Quantum computers are another potential application of nanoscale materials.<sup>45</sup> The quantum computer is a machine that aims to exploit the full complexity of a many-particle quantum wavefunction to solve a computational problem and thus would dramatically improve the computational power for particular tasks. The central challenge in actually building quantum computers is maintaining the simultaneous abilities to control quantum systems, to measure them, and to preserve their strong isolation from uncontrolled parts of their environment.<sup>46</sup> Quantum dots integrated into a solid state host is one of the technologies addressing this challenge, as shown in Figure 1.8, because large arrays of qubits may be easier to assemble and cool. Quantum logic can be accomplished by changing voltages on the electrostatic gates to move electrons closer or further from each other, activating and deactivating the exchange interaction.<sup>47</sup>

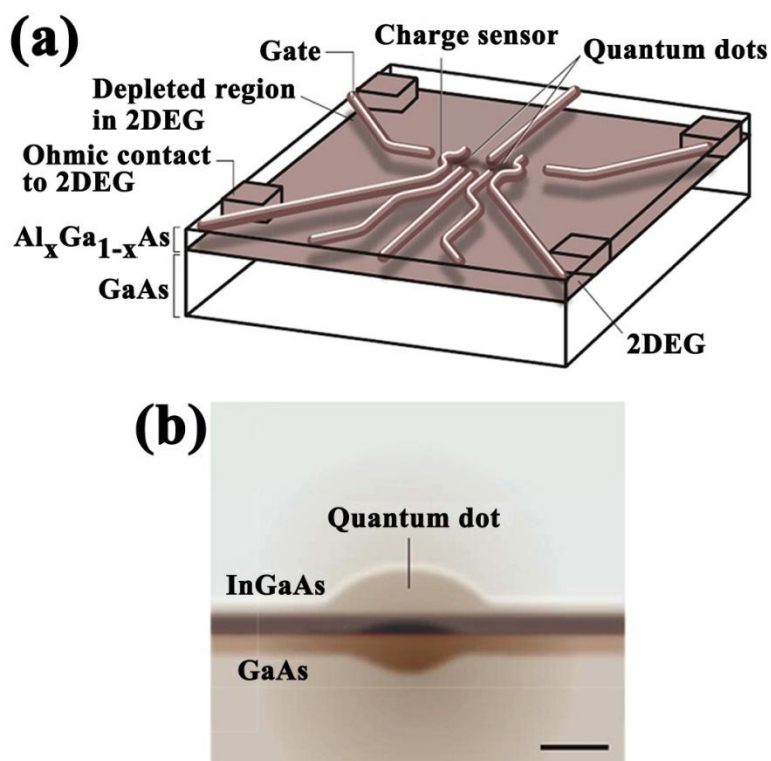


**Figure 1.8** Quantum dot and solid-state dopant qubits. (a) An electrostatically confined quantum dot; the structure shown is several mm across. 2DEG, two-dimensional electron gas. (b) A self-assembled quantum dot. Scale bar is 5 nm. Reproduced with permission from ref. 46.

### 1.2.4 Biotechnology

Nanoparticles possess unique size- and shape-dependent properties and demonstrate potential for a wide-range of biomedical applications such as imaging, cancer treatment, and drug delivery. Quantum dots exhibit intense luminescence, often 20 times brighter and 100 times more stable than that of typical organic fluorescent dye molecules.<sup>48</sup> In addition, the emission of the quantum dots can be tuned by changing their size, thus providing a choice of different colors. This unique property made them appealing as *in vivo* and *in vitro* fluorophores for a variety of biological studies, e.g. bio-labeling and bio-imaging.<sup>49</sup> For example, Mulder *et al.* fabricated quantum dots coated with paramagnetic  $Gd^{3+}$  ions and pegylated lipids (Figure 1.9).<sup>50</sup> The *in vitro* imaging capability of paramagnetic quantum dots was demonstrated for angiogenic human

umbilical vein endothelial cells. Biocompatible magnetic nanoparticles like  $\text{Fe}_3\text{O}_4$  (magnetite) and  $\text{Fe}_2\text{O}_3$  (maghemite) also have been extensively studied for imaging (magnetic resonance imaging, MRI).<sup>51</sup> The MRI technique is based on the nuclear magnetic resonance of the various interacting nuclei. The factors influencing the signal strength of MRI are spin-lattice/longitudinal relaxation time, transverse relaxation time, and spin energy. Magnetic nanoparticles are generally introduced as exogenous contrast agents to enhance the tissue contrast.<sup>51</sup> Bawendi's group also described an efficient synthetic method for magnetic and fluorescent silica microspheres fabricated by incorporating magnetic ( $\gamma\text{-Fe}_2\text{O}_3$ ) nanoparticles and CdSe/CdZnS core/shell quantum dots into a silica shell around preformed silica microspheres.<sup>52</sup>

Magnetic nanoparticles have been actively investigated for hyperthermia treatment of targeted cancer, stem cell sorting and manipulation, guided drug delivery, gene therapy and DNA analysis, etc.<sup>51, 53</sup> For several biomedical procedures, the separation of specific biological entities (e.g. DNAs, proteins, and cells) from their native environment is often required for analysis. Superparamagnetic colloids are ideal systems for bioseparation because their on-off nature of magnetization with and without an external magnetic field enables the magnetic separation of adsorbed biomolecules. To increase the colloidal stability, nanoparticles are usually coated with polymers, such as polyethylene glycol<sup>54</sup> or polyvinylpyrrolidone,<sup>55</sup> which also provide conjugation between the magnetic particles and the targeted biological entities of interest. Compared to polymer-coated nanoparticles, nanostructures of porous hollow structure, core-shell structure, etc. have received more attention because of their large loading capacity, large surface area, stability, etc.<sup>56, 57</sup> As an example, sandwich-structured mesoporous silica microspheres (~500 nm), composed of a silica-coated magnetite core and ordered mesoporous silica shell with

perpendicularly oriented channels, exhibit an enhanced adsorption efficiency for fast removal of large microcystins from solution.<sup>58</sup>

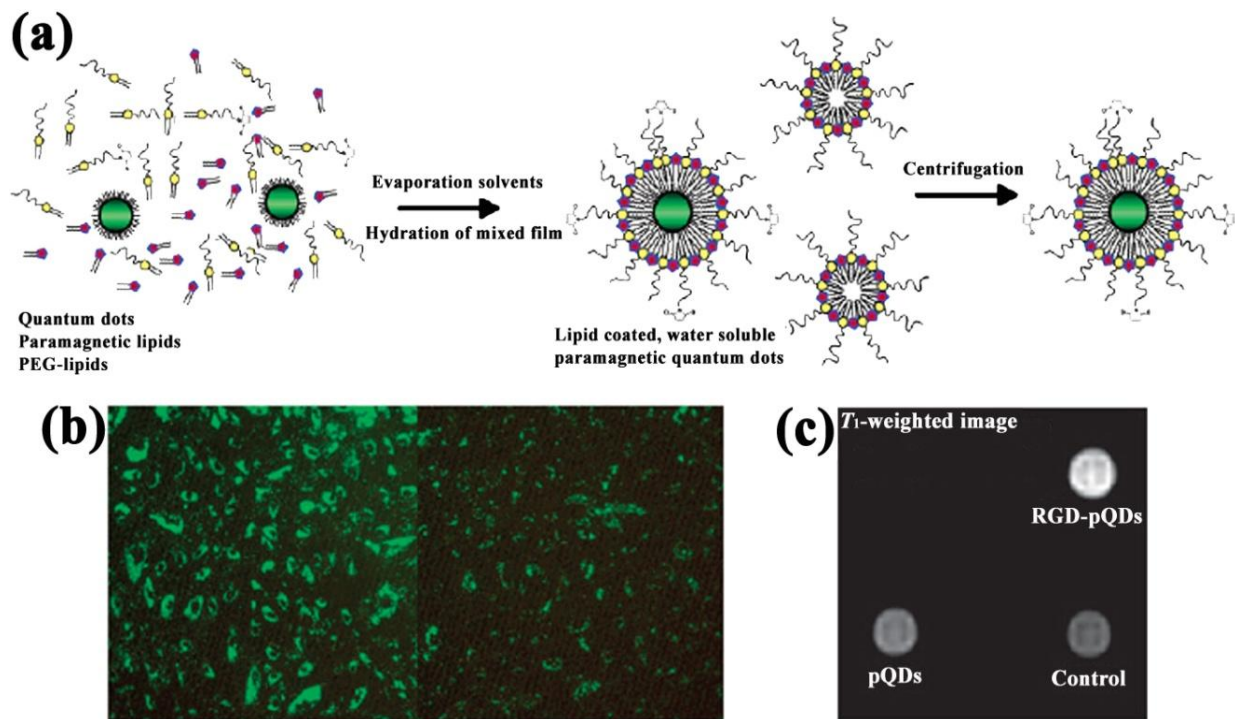


**Figure 1.9** (a) Schematic representation of the preparation of QDs with a paramagnetic micellular coating. (b) Fluorescence microscopy of HUVEC incubated with RGD-pQDs and bare pQDs. (c) T1-weighted image of cells that were incubated with RGD-pQDs, pQDs, or without contrast agent. Reproduced with permission from ref. 50.

### 1.3 Synthetic Methods of Nanomaterials

Rapid progress has been made in the last decade with regards to the controlled synthesis of nanoparticles both for fundamental research and technological applications. According to Moore's law, the size of microelectronic devices shrinks by half every four years. In comparison, the development of nanomaterials with desired properties has lagged behind because of significant challenges. For example, semiconductor quantum dots usually need to be stabilized against aggregation for retaining their quantum confinement effect. Adsorption of solvent

molecules or ligands is one of the common methods to cap the particles for stabilization in solution. Such capping agent however can greatly perturb the performance of surface-related properties. Therefore, the fabrication of nanostructures with desired properties is not without challenge and consequently, various chemical approaches have been developed, including solution methods, templating methods, and biological synthetic methods, to fabricate desired nanomaterials.

### **1.3.1 Solution Methods**

The commonly used solution methods for the synthesis of nanomaterials include coprecipitation, microemulsion, hydro/solvothermal synthesis, and thermal decomposition synthesis.

#### **1.3.1.1 Coprecipitation**

Coprecipitation is one of the earliest reported synthetic methods for preparing nanoparticles. Typically, nanoparticles are formed from sparingly soluble species formed under conditions of high supersaturation. The materials synthesized using this method include metals, oxides, and chalcogenides.<sup>59</sup> Most of the simple precipitation reactions can be carried out under aqueous conditions. For ternary and quaternary systems, multiple species have to be precipitated simultaneously and nonaqueous conditions are preferable. Meanwhile, numerous strategies have been investigated to induce precipitation such as electrochemical reduction, radiation-assisted reduction, decomposition of metallorganic precursors, microwave-assisted coprecipitation, sonication-assisted coprecipitation, etc.<sup>59</sup>

Merely inducing the precipitation of a compound, however, does not guarantee that the product will have uniform shape and a narrow size distribution. The particle size and morphology of products from precipitation reactions are governed by the processes of nucleation and growth. When precipitation begins, numerous small crystalline nuclei initially formed tend to quickly aggregate together to form larger particles.<sup>60</sup> Such ready agglomeration of fine particles is caused by attractive van der Waals forces and the minimization of the total surface or interfacial energy of the system. This thermodynamic stabilization process is termed as Ostwald ripening and aggregation. In order to produce nanoparticles with a narrow size distribution the nucleation process of all particles must occur simultaneously and be sufficiently fast while the growth process remains relatively slow.<sup>59</sup> Experimentally, the simplest approach to prevent agglomeration is using a capping agent to protect the surface of particles and thereby prevent them from further growth.<sup>61</sup> The capping agent can be the solvent itself, but in many cases an additional polymeric stabilizer is used to attach to the particle surface. The morphology of nanoparticles is determined by the reaction conditions (reaction time, concentration, etc.) and may exhibit significant shape evolution with varying reaction conditions, but eventually will become spherical due to the lowest surface energy of this shape.<sup>59</sup>

### **1.3.1.2 Microemulsion**

Microemulsions have been developed since 1943 when Hoar and Schulman first observed a clear homogenous solution of four-component mixture of water, oil, surfactant, and an alcohol or amine-based cosurfactant.<sup>62</sup> Amphiphilic surfactants are long-chain organic molecules with a hydrophilic head and lipophilic tail, which makes them miscible in both water and oil. In microemulsion, these surfactants form spherical aggregates in which the hydrophilic ends of the

surfactant molecules orient toward the center, with a small water droplet situating at the center of each spherical aggregate. The polar cosurfactants then interact with the surfactant heads through ion-dipole interactions to minimize repulsions between the positively charged surfactant heads. Thus microemulsions are thermodynamically stable. These monodispersed water droplets have been used as nanoreactors where nanoparticles precipitate with dimensions limited by that of the water droplets.<sup>63</sup> Thus far, a variety of nanomaterials including oxides, halides, sulfides metals, and alloys have been synthesized using this method. The particle size is tunable by changing the water-to-surfactant ratio. But the subsequent calcination required for improving the crystallinity of the product will inevitably result in some degree of agglomeration. Another concern about this method is the selection of surfactants. For the system containing oxidizing or reducing agents, the surfactant should be chemically inert with respect to all other components. The most commonly investigated surfactants are ionic surfactant such as cetyl trimethylammonium bromide and sodium bis(2-ethylhexyl)sulfosuccinate. These surfactants are stable against mild oxidizers (dilute H<sub>2</sub>O<sub>2</sub>) and mild reducing agents (hydrazine) but can be problematic in the presence of stronger reducing agents such as borohydride ions.<sup>59</sup>

### **1.3.1.3 Thermal Decomposition Method**

The thermal decomposition of organometallic compounds in hot high-boiling organic solvents in the presence of a surfactant has been widely used for the synthesis of a variety of uniform monodisperse nanocrystals.<sup>64</sup> The size and morphology of the nanocrystals can be precisely controlled by simply changing the reaction temperature, reaction time, and aging time. This method was firstly reported by Murray *et al.* who reacted solutions of dimethylcadmium, (CH<sub>3</sub>)<sub>2</sub>Cd, in tri-n-octylphosphine (TOPO) and tri-n-octylphosphine selenide in hot tri-n-

octylphosphine oxide in the temperature range 120-300 °C.<sup>65</sup> This reaction produced TOPO-capped nanocrystallites of CdSe. The size of the particles is controlled mainly by the reaction temperature, with larger particles being obtained at higher temperatures. This TOPO method has advantages over previous synthetic methods, including monodispersity and high yield of products (hundreds of milligrams of materials in a single experiment). Alivisatos subsequently used higher temperatures for injection and growth to improve the quality of the prepared materials.<sup>66</sup> Thus far many interesting structures, such as rod-like, tetrapodal, or core-shell structures having high quantum efficiencies, have been prepared by this method.<sup>67, 68</sup>

#### **1.3.1.4 Hydrothermal/Solvothermal Synthesis**

In the research area of semiconductors, high quality monodisperse nanoparticles generally are prepared by thermal decomposition of organometallic precursors at elevated temperatures. Such a method is expensive and also uses toxic precursors. Comparably, hydrothermal/solvothermal synthesis provides a single-step process with advantages of lower energy requirement, narrow particle size distribution, ability to obtain diverse compounds with unique properties, etc. Hydrothermal/solvothermal synthesis usually is performed in a sealed vessel (bomb, autoclave, etc.) at elevated temperatures and autogeneous pressures resulting from the heating process. Thereby, the chemical reactivity and solubility of reagents can be enhanced, allowing many inorganic materials to be prepared at temperatures substantially below those required using traditional solid-state reactions. In addition, the products from hydrothermal/solvothermal reactions are usually crystalline and do not require a post-annealing treatment which can cause particle agglomeration. Moreover, by changing the reaction

temperature, time, and solvents, both the crystalline phase and the size of the nanoparticles can be controlled.<sup>69</sup>

### **1.3.2 Templating Methods**

The synthesis of nanomaterials with the aid of templates has garnered a great deal of interest because the templating methods are very effective in creating complex nanostructures (one-, two-, and three-dimensional structures). In order to achieve the desired properties, several types of templates, varying from inorganic particles to organic molecules, have been applied in syntheses. The templates can be retained or removed afterwards with corresponding strategies according to the application environment of the materials.

#### **1.3.2.1 Inorganic Hard Templates**

The use of crystal seeds as nucleation sites for the further deposition and growth of crystallites can essentially be considered as one of the simplest forms of templated synthesis. For example, Au colloids were used as seeds to achieve larger Au nanoparticles from aqueous Au<sup>3+</sup>, with the addition of hydroxylamine (NH<sub>2</sub>OH) to prevent nucleation from solution and thus avoid a broad size distribution.<sup>70</sup> This seed-mediated method has been used for the synthesis of metal nanoparticles, core-shell and onion structures. For producing more complicated structures, other hard templates including zeolites, mesoporous silicates, nanoporous alumina, layered solids, membranes, polystyrene spheres, carbon nanotubes, etc., have commonly been used in the synthesis of nanomaterials.<sup>59</sup> The precursors can be incorporated into the channels and spaces of these hard templates by sorption, phase transition, ion exchange, complex or covalent grafting. Upon heat treatment and phase transition, the precursors are thermally decomposed and the

derived nanoparticles grow larger in the confined spaces to form nanoparticles with different shapes, or interconnect with each other to form interesting nanostructures with continuous frameworks.

The removal of the hard templates is important for many applications. A variety of template removal strategies have thus been developed during the templating synthesis. For example, Ag particle templates can be removed by the galvanic replacement reaction to give rise to hollow Au spheres. In some cases, the template removal process gives rise to more interesting structures, such as nanoboxes, triangular nanorings, multiple-walled nanoshells or nanotubes, reflecting the size and shape of the initial nanotemplates.<sup>71-73</sup> For example, Xu *et al.* transformed cobalt nanocrystal assemblies to CoSe<sub>2</sub> hollow nanostructures retaining the chain-like shape via the Kirkendall process.<sup>74</sup>

### 1.3.2.2 Organic Soft Templates

Routine organic soft templates include some polymers, surfactants (true-liquid-crystal mesophases), etc.<sup>59, 75</sup> The polymer-templated method was initially developed for the reduction of transition metals, decomposition of metal carbonyls, or precipitation of metal oxides in polymer matrices. Dendrimers, such as poly(amidoamine), belong to a class of soft polymer templates, appearing as roughly spherical large molecules comprised of repeating branches. Such templates can absorb reagent ions into their dendrimer structure prior to chemical reactions and encapsulate the formed nanoparticles from further growth. The size of nanoparticles synthesized on dendrimers can reach as small as 1 nm.<sup>59</sup>

Surfactants have been intensively used in nanomaterial synthesis, as described in the section on microemulsion. Commonly used surfactants are long-chain hydrocarbons with a hydrophilic

head and lipophilic tail. The self-assembly feature of surfactants evolve along with changes in the surfactant concentration and system temperature. As the concentration of a surfactant in a solvent is larger than the critical micellization concentration, the surfactant micellar solution transforms to form lyotropic liquid crystals (of either “oil-in-water” or “water-in-oil”), which are called true-liquid-crystal mesophases. A mesophase will turn to an isotropic phase as the temperature increases above the critical micellization temperature. True-liquid-crystal mesophases present in highly concentrated surfactant solutions have been used to synthesize ordered mesostructured nanocomposites, especially chalcogenides.<sup>75</sup> During the synthesis, the inorganic precursors cast the mesostructures, pore sizes, and symmetries from the true-liquid-crystal scaffolds, forming morphology confined and ceramic-like frameworks. After the condensation of the inorganic materials, the organic templates can be removed by calcination, extraction, etc.

### **1.3.3 Biological Synthetic Methods**

The biological synthesis (or biomimetics) refers to chemical synthetic methods inspired by biologically related processes. The interest in this interdisciplinary research field stems from the fact that biosystems can use relatively simple building blocks to self-assemble structures displaying a high degree of organization. A wide range of biological matter, ranging from individual biomolecules (DNA, proteins, hydrocarbonates, etc.) to biological entities (bacteria, phages, fungi, etc.), has been utilized to template or catalyst the synthesis of nanostructured materials.

### 1.3.3.1 Biomolecules

DNA is one of the most intensively utilized biomolecules for templating novel metal particles, metal nanowires, two-dimensional metal networks. Double-stranded DNA (dsDNA) consists of two strands of nucleotide polymers, running in anti-parallel directions and stabilized by hydrogen bonds between the nitrogenous base pairs. The external backbone of the nucleotide polymers is made of alternative pentoses and phosphate groups joined by phosphodiester bonds. The length of natural DNA molecules can be very long, example, 220 million base pairs long for the human chromosome number 1 (one nucleotide unit around 0.33 nm long).<sup>76</sup> Since DNAs contain backbones of phosphate which are negatively charged, they have been used in the reduction or precipitation of metal cations or in the assembly of positively-charged nanoparticles into one-dimensional nanowires, nanoribbons, etc.<sup>77</sup> DNA also can be tailored into more complicated structures to direct the synthesis of higher ordered nanomaterials. For example, Sharma *et al.* assembled two types of DNA tiles, hybridized at the complementary sticky ends, into two-dimensional nanogrids, with one type of DNA tiles attached by Au nanoparticles through thiol linkage.<sup>78</sup> Consequently, Au nanoparticles form a designed assembly pattern with precisely controlled interspacing.

Another popular type of biomolecule template is polymers of amino acids (peptides and proteins). There are twenty-two standard amino acids classified by the properties of their side chains into four groups (weak acidic, weak basic, hydrophilic, and hydrophobic). Peptide refers to a short polymer chain of amino acids linked to each other by covalent peptide bonds. Both naturally occurring and artificially synthesized peptides have been used to template or catalyze the formation of nanomaterials.<sup>79</sup> The morphology of the inorganic products include nanoparticles, nanowires, and double helical superstructure of gold nanoparticles.<sup>80-82</sup> Proteins

are composed of polypeptides, showing favorable conformations. Spherical apoferritin composed of 24 polypeptide subunits is the most intensively investigated protein template. The size of the inner cavity of this protein is about 8 nm and that of the outer diameter is about 12 nm.<sup>77</sup> A range of nano-sized metals and compounds have been produced by the deposition within the cavity of apoferritin. Kim *et al.* proposed that the shell wall has channels through which ions and small molecules can move in and out, resulting in the formation of shape- and size-controlled monodisperse nanoparticles.<sup>83</sup> Moreover, modifications on the surface of proteins, either by chemical methods or genetic methods, have been widely studied to improve the attachment of inorganic materials to the proteins or to assist the construction of more complicated structures.<sup>77</sup> For example, Mann *et al.* assembled ferritins into two-dimensional arrays through the modification of the protein surface with biotin which then interacts with streptavidin to form a cross-linked network.<sup>43</sup> Consequently, arrays of ferromagnetic iron oxides grown within the cavity of patterned ferritin could be obtained.

### 1.3.3.2 Microorganism

Many microorganisms have the intrinsic ability to produce inorganic materials either intra- or extracellularly under mild conditions for their existence. In particular, they have the ability to recognize and control the formation of inorganic materials. For example, diatoms precipitate silica with species-specific morphologies and stunning architectures; the silver-resistant bacteria strain *Pseudomonas stutzeri* AG259 can form Ag and Ag<sub>2</sub>S nanoparticles inside the cell to tolerate the high concentration of Ag<sup>+</sup> in the environment; magnetotactic bacteria synthesize magnetic Fe<sub>3</sub>O<sub>4</sub> nanocrystals inside their magnetosomes and the alignment of these magnets can direct cell movement.<sup>77, 84</sup> Because of the advantages of eco-friendly reaction conditions and

controlled product morphology, microorganism mineralization has been widely mimicked *in vitro* for synthesizing high-performance nanomaterials.<sup>79, 84</sup> The synthesized inorganic compounds on various templates range from metals to alloys, semiconductors, and composites. As an example, Sweeney *et al.* produced wurzite CdS nanocrystals inside *Escherichia coli* upon incubating cells with inorganic precursors.<sup>85</sup> By changing reaction conditions and precursors, CdS of nanoporous hollow structures were generated on the same type of cells and exhibited enhanced catalytic activity.<sup>43</sup>

### 1.3.3.3 Viruses

In the past decade, there has been a growing interest in the use of virus particles as templates for nanosized materials. Virus typically consists of several hundreds to thousands of protein molecules that self-assemble to form a confined protein scaffold, which encapsulates the viral nucleic acid. Cowpea chlorotic mottle virus (CCMV) is one type of spherical viruses widely used in the synthesis of nanoparticles. The protein scaffold of CCMV virion is composed of 180 subunits and about 28 nm in diameter, with an inner cavity of ~18 nm.<sup>86</sup> By changing the pH value, the protein scaffold will open to release its RNA, and then reassemble as the pH is tuned back. After removing the negatively charged RNA, the positively charged interior surface of the protein scaffold is exposed, thus being able to attract anionic components or negatively charged materials. The host-guest relationship between the protein cage and the encapsulated material is primarily based on this complementary electrostatic interaction.<sup>87</sup> Douglas and Young have used this electrostatic host-guest interaction to encapsulate two polyoxometalate species (paratungstate and decavanadate) and an anionic polymer inside the CCMV cage.<sup>88</sup> After a further step of oligomeration, uniform nanocrystals, constrained in the protein cages, were

obtained. Under the similar host-guest interaction mechanism, cylindrical tobacco mosaic virus (TMV) protein scaffold, in the form of a hollow tube (300 x 18 nm with a central channel of ~4 nm in diameter), can encapsulate anisotropic assemblies of spherical Pt, Au, or Ag nanoparticles.<sup>89</sup> Furthermore, the external surface of protein cages can be modified by either chemical or genetic methods, causing the biomineralization to be selectively performed on the outer surface of the protein capsid.<sup>90</sup> Another type of viral template is filamentous M13 bacteriophage, which has emerged as an efficient template for the synthesis of nanowires. Filamentous M13 bacteriophage is approximately 860 nm long and 6.5 nm wide. Belcher's group genetically engineered peptides, specific to desired inorganic materials, to the main coat protein (PVIII) of M13.<sup>91</sup> During the consequent biomineralization, the inserted peptides direct the nucleation and growth of nanocrystals of a preferred crystal phase. The uniform precipitation of nanocrystals along the filamentous virus gives rise to the formation of nanowires.

#### **1.4 Research Objectives**

The properties of inorganic materials in nanoscale have been found to be size- and shape-dependent due to the quantum confinement effects. Arranging monodispersed nanoparticles into high-ordered hierarchical architectures can likely generate unprecedented properties for future applications and bypass the issue of nanoparticle aggregation. Biological matter possesses robust and precisely ordered structures and exists in a large variety of sizes and shapes, providing a platform for synthesizing high-performance nanostructures. We have aimed to expand the repertoire of natural biotemplates for the fabrication of nanostructures, investigate the mechanism of bio-inorganic interactions, and eventually enhance the performance of materials of interest for specific applications.

## 1.5 References

1. Zhou, S.; McIlwrath, K.; Jackson, G.; Eichhorn, B. *J. Am. Chem. Soc.* **2006**, *128*, 1780-1781.
2. Cheng, K.; Peng, S.; Xu, C.; Sun S. *J. Am. Chem. Soc.* **2009**, *131*, 10637-10644.
3. Xu, C.; Wang, B.; Sun, S. *J. Am. Chem. Soc.* **2009**, *131*, 4216-4217.
4. Choi, S.-H.; Na, H. B.; Park, Y.; An, K.; Kwon, S. G.; Jang, Y.; Park, M.; Moon, J.; Son, J. S.; Song, I. C.; Moon, W. K.; Hyeon, T. *J. Am. Chem. Soc.* **2008**, *130*, 15573-15580.
5. Ge, J.; Hu, Y.; Yin, Y. *Angew. Chem. Int. Ed.* **2007**, *46*, 7428-7431.
6. Nutzenadle, C.; Zuttel, A.; Chartouni, D.; Schmid, G.; Schlapbach, L. *Eur. Phys. J. D* **2000**, *8*, 245-250.
7. McConnell, W. P.; Novak, J. P.; Brousseau III, L. C.; Fuierer, R. R.; Tenent, R. C.; Feldheim, D. L. *J. Phys. Chem. B* **2000**, *104*, 8925-8930.
8. Sun, S. *Adv. Mater.* **2006**, *18*, 393-403.
9. Trindade, T. *Chem. Mater.* **2001**, *13*, 3843-3858.
10. Xia, Y.; Yang, P. *Adv. Mater.* **2003**, *15*, 351-352.
11. Varghese, O. K.; Paulose, M.; Grimes, C. A. *Nature Nanotechnology* **2009**, *4*, 592-597.
12. Sun, C.-L.; Chen, L.-C.; Su, M.-C.; Hong, L.-S.; Chyan, O.; Hsu, C.-Y.; Chen, K.-H.; Change, T.-F.; Chang, L. *Chem. Mater.* **2005**, *17*, 3749-3753.
13. Law, M.; Greene, L. E.; Johnson, J. C.; Saykally, R.; Yang, P. *Nat. Mater.* **2005**, *4*, 455-459.
14. Burda, C.; Chen, X.; Narayanan, R.; El-Sayed, M. A. *Chem. Rev.* **2005**, *105*, 1025-1102.
15. Shim, J.-H.; Lee, B.-J.; Cho, Y. W. *Surf. Sci.* **2002**, *512*, 262-268.
16. Faraday, M. *Philos. Trans. R. Soc. London* **1857**, *147*, 145-181.
17. Mie, G. *Ann. Phys.* **1908**, *330*, 377-445.
18. Gharibshahi, E.; Saion, E. *Phy. Intl.* **2010**, *1*, 57-64.
19. Jain, P. K.; Lee, K. S.; El-sayed, I. H.; El-sayed, M. A. *J. Phys. Chem. B* **2006**, *110*, 7238-7248.

20. Vossmeier, T.; Katsikas, L.; Giersig, M.; Popovic, I. G.; Diesner, K.; Chemseddine, A.; Eychmuller, A.; Weller, H. *J. Phys. Chem.* **1994**, *98*, 7665-7673.
21. Nimtz, G.; Marquardt, P.; Gleiter, H. *J. Cryst. Growth*, **1990**, *86*, 66-71.
22. Ray, V.; Subramanian, R.; Bhadrachalam, P.; Ma, L.-C.; Kim, C.-U.; Koh, S. J. *Nat. Nanotechnol.* **2008**, *3*, 603-608.
23. Schubert, U.; Husing, N. in *Synthesis of Inorganic Materials*, 2nd ed., Wiley-VCH, Weinheim, **2005**, Chapter 7, p 368.
24. Spaldin, N. A. in *Magnetic Materials: Fundamentals and Applications*, 2<sup>nd</sup> ed., Cambridge University Press, **2010**, Chapter 12, p 145.
25. Lu, A.; Salabas, E. L.; Schüth, F. *Angew. Chem. Int. Ed.* **2007**, *46*, 1222-1244.
26. Park, J.; Lee, E.; Hwang, N.-M; Kang, M.; Kim, S.; Hwang, Y.; Park, J.-Y; Noh, H.; Kim, J.; Park, J.-H.; Hyeon, T. *Angew. Chem. Int. Ed.* **2005**, *44*, 2872-2877.
27. Battle, X.; Labarta, A. *J. Phys. D: Appl. Phys.* **2002**, *35*, R15-R42.
28. Narayanan, R.; El-Sayed, M. A. *J. Phys. Chem. B* **2005**, *109*, 12663-12676.
29. Sun, C.-L.; Chen, L.-C.; Su, M.-C.; Hong, L.-S.; Chyan, O.; Hsu, C.-Y.; Chen, K.-H.; Chang, T.-F.; Change, L. *Chem. Mater.* **2005**, *17*, 3749-3753.
30. Takagaki, A.; Sugisawa, M.; Lu, D.; Kondo, J. N.; Hara, M.; Domen, K.; Hayashi, S. *J. Am. Chem. Soc.* **2003**, *125*, 5479-5485.
31. Bao, N.; Shen, L.; Takata, T.; Domen, K. *Chem. Mater.* **2008**, *20*, 110-117.
32. Collins, R. W.; Ferlauto, A. S.; Ferreira, G. M.; Chen, C.; Koh, J; Koval, R. J.; Lee, Y.; Pearce, J. M.; Wronski, C. R. *Sol. Energy Mater. Sol. Cells* **2003**, *78*, 143-180.
33. Fthenakis, V. M. *Renew. Sust. Energ. Rev.* **2004**, *8*, 303-334.
34. Ramanathan, K.; Contreras, M.; Perkins, C.; Asher, S.; Hasoon, F.; Keane, J.; Young, D.; Romero, M. J.; Metzger, W.; Noufi, R.; Ward, J.; Duda, A. *Prog. Photovoltaics* **2003**, *11*, 225-230.
35. O'Regan, B.; Grätzel, M. *Nature* **1991**, *353*, 737-740.
36. Shockley, W.; Queisser, H. J. *J. Appl. Phys.* **1961**, *32*, 510-514.
37. Nozik, A. J. *Chem. Phys. Lett.* **2008**, *457*, 3-11.

38. Mor, G. K.; Varghese, O. K.; Paulose, M.; Shankar, K.; Grimes, C. A. *Sol. Energy Mater. Sol. Cells* **2006**, *90*, 2011–2075.
39. Shen, L.; Bao, N.; Prevelige, P. E.; Gupta, A. *J. Phys. Chem. C* **2010**, *114*, 2551–2559.
40. Tian, B.; Zheng, X.; Kempa, T. J.; Fang, Y.; Yu, N.; Yu, G.; Huang, J.; Lieber, C. M. *Nature* **2007**, *449*, 885-889.
41. Murphy, L. *Curr. Opin. Chem. Biol.* **2006**, *10*, 177–184.
42. Guo, S.; Dong, S. *Trends Anal. Chem.* **2009**, *28*, 96-109.
43. Li, M.; Wong, K. K. W.; Mann, S. *Chem. Mater.* **1999**, *11*, 23-26.
44. Glybin, V.; Lynkov, L.; Bogush, V. in *Physics, Chemistry and Application of Nanostructure: Reviews and Short Notes to Nanomeeting'99*, World Scientific Publishing Co. Pte. Ltd. **1999**, C.251.
45. Ladd, T. D.; Jelezko, F.; Laflamme, R.; Nakamura, Y.; Monroe, C.; O'Brien, J. L. *Nature* **2010**, *464*, 45-53.
46. Hanson, R.; Awschalom, D. D. *Nature* **2008**, *453*, 1043-1049.
47. Hanson, R.; Kouwenhoven, L. P.; Petta, J. R.; Tarucha, S.; Vandersypen, L. M. K. *Rev. Mod. Phys.* **2007**, *79*, 1217-1265.
48. Chan, W. C. W.; Nie, S. M. *Science* **1998**, *281*, 2016-2018.
49. Medintz, I. L.; Uyeda, H. T.; Goldman, E. R.; Mattoussi, H. *Nature Materials* **2005**, *4*, 435-446.
50. Mulder, W. J. M.; Koole, R.; Brandwijk, R. J.; Storm, G.; Chin, P. T. K.; Strijkers, G. J.; Donega, C. de M.; Nicolay, K.; Griffioen, A. W. *Nano Lett.* **2006**, *6*, 1-6.
51. Figuerola, A.; Corato, R. D.; Manna, L.; Pellegrino, T. *Pharmacol. Res.* **2010**, *62*, 126–143.
52. Insin, N.; Tracy, J. B.; Lee, H.; Zimmer, J. P.; Westervelt, R. M.; Bawendi, M. G. *ACS Nano* **2008**, *2*, 197-202.
53. Yang, J.; Lee, C. H.; Park, J.; Seo, S.; Lim, E. K.; Song, Y. J.; Suh, J. S.; Yoon, H. G.; Huh, Y. M.; Haam, S. J. *Mater. Chem.* **2007**, *17*, 2695-2699.
54. Lee, H.; Lee, E.; Kim, D. K.; Jang, N. K.; Jeong, Y. Y.; Jon, S. *J. Am. Chem. Soc.* **2006**, *128*, 7383-7389.
55. Gupta, A. K.; Gupta, M. *Biomaterials* **2005**, *26*, 3395-4021.

56. Cheng, K.; Peng, S.; Xu, C.; Sun, S. *J. Am. Chem. Soc.* **2009**, *131*, 10637-10644.
57. Xu, X.; Deng, C.; Gao, M.; Yu, W.; Yang, P.; Zhang, X. *Adv. Mater.* **2006**, *18*, 3289-329.
58. Deng, Y.; Qi, D.; Deng, C.; Zhang, X.; Zhao, D. *J. Am. Chem. Soc.* **2008**, *130*, 28-29.
59. Cushing, B. L.; Kolesnichenko, V. L.; O'Connor, C. J. *Chem. Rev.* **2004**, *104*, 3893-3946.
60. Park, J.; Privman, V.; Matijević, E. *J. Phys. Chem. B* **2001**, *105*, 11630-11635.
61. Ge, J.; Hu, Y.; Biasini, M.; Dong, C.; Guo, J.; Beyermann, W. P.; Yin, Y. *Chem. Eur. J.* **2007**, *13*, 7153 – 7161.
62. Hoar, T. P.; Schulman, J. H. *Nature* **1943**, *152*, 102-103.
63. Vriezema, D. M.; Aragone`s, M. A.; Elemans, J. A. A. W.; Cornelissen, J. J. L. M.; Rowan, A. E.; Nolte, R. J. M. *Chem. Rev.* **2005**, *105*, 1445-1489.
64. Hyeon, T. *Chem. Commun.* **2003**, 927–934.
65. Murray, C. B.; Norris, D. J.; Bawendi, M. G. *J. Am. Chem. Soc.* **1993**, *115*, 8706-8715.
66. Malik, M. A.; O'Brien, P. in *Precursor Chemistry of Advanced Materials: CVD, ALD and Nanoparticles*, Springer, **2005**, p 178.
67. Li, Y.; Zhong, H.; Li, R.; Zhou, Y.; Yang, C.; Li, Y. *Adv. Funct. Mater.* **2006**, *16*, 1705-1716.
68. Bao, N.; Shen, L.; Wang, Y.-H. A.; Ma, J.; Mazumdar, D.; Gupta, A. *J. Am. Chem. Soc.*, **2009**, *131*, 12900–12901.
69. Shen, L.; Bao, N.; Zheng, Y.; Gupta, A.; An, T.; Yanagisawa, K. *J. Phys. Chem. C*, **2008**, *112*, 8809–8818.
70. Brown, K. R.; Natan, M. J. *Langmuir* **1998**, *14*, 726-728.
71. Skrabalak, S. E.; Chen, J.; Sun, Y.; Lu, X.; Au, L.; Cobley, C. M.; Xia, Y. *Acc. Chem. Res.* **2008**, *41*, 1587-1595.
72. Chen, J.; Saeki, F.; Wiley, B. J.; Cang, H.; Cobb, M. J.; Li, Z. Y.; Au, L.; Zhang, H.; Kimmey, M. B.; Li, X. D.; Xia, Y. *Nano Letters* **2005**, *5*, 473-477.
73. Khalavka, Y.; Becker, J.; Sönnichsen, C. *J. Am. Chem. Soc.* **2009**, *131*, 1871-1875.
74. Gao, J.; Zhang, B.; Zhang, X.; Xu, B. *Angew. Chem. Int. Ed.* **2006**, *45*, 1220-1223.

75. Wan Y.; Zhao, D. *Chem. Rev.* **2007**, *107*, 2821–2860.
76. Gregory, S.; Barlow, K. F.; McLay, K. E.; Kaul, R.; et al. *Nature* **2006**, *441*, 315-321.
77. Fan, T.-X.; Chow, S.-K.; Zhang, D. *Prog. Mater. Sci.* **2009**, *54*, 542-659.
78. Sharma, J.; Chhabra, R.; Liu, Y.; Ke, Y.; Yan, H. *Angew Chem Int Ed.* **2006**, *45*, 730–735.
79. Chen, C. L.; Rosi, N. L. *Angew. Chem. Int. Ed.* **2010**, *49*, 1924-1942.
80. Flynn, C. E.; Mao, C.; Hayhurst, A.; Williams, J. L.; Georgiou, G.; Iverson, B.; Belcher, A. M. *J. Mater. Chem.* **2003**, *13*, 2414-2421.
81. Mao, C.; Solis, D. J.; Reiss, B. D.; Kottmann, S. T.; Sweeney, R. Y.; Hayhurst, A.; Georgiou, G.; Iverson, B.; Belcher, A. M. *Science* **2004**, *303*, 213-217.
82. Chen, C. L.; Rosi, N. L. *J. Am. Chem. Soc.* **2010**, *132*, 6902–6903.
83. Kim, J. W.; Choi, S. H.; Lillehei, P. T.; Chu, S. H.; King, G. C.; Watt, G. D. *Chem. Commun.* **2005**, *32*, 4101-4103.
84. Palmer, L. C.; Stupp, S. I. *Acc. Chem. Res.* **2008**, *41*, 1674-1684.
85. Sweeney, R. Y.; Mao, C.; Gao, X.; Burt, J. L.; Belcher, A. M.; Georgiou, G.; Iverson, B. *Chem. Biol.* **2004**, *11*, 1553-1559.
86. Speir, J. A.; Munshi, S.; Wang, G.; Baker, T. S.; Johnson, J. E. *Structure* **1995**, *3*, 63-78.
87. Allen, M.; Willits, D.; Young, M.; Douglas, T. *Inorg. Chem.* **2003**, *42*, 6300–6305.
88. Douglas, T.; Young, M. *Nature* **1998**, *393*, 152-155.
89. Dujardin, E.; Peet, C.; Stubbs, G.; Culver, J. N.; Mann, S. *Nano Lett.* **2003**, *3*, 413–417.
90. Klem, M. T.; Willits, D.; Young, M.; Douglas, T. *J. Am. Chem. Soc.* **2003**, *125*, 10806-10807.
91. Mao, C.; Flynn, C. E.; Hayhurst, A.; Sweeney, R.; Qi, J.; Georgiou, G.; Iverson, B.; Belcher, A. M. *Proc. Natl. Acad. Sci.* **2003**, *100*, 6946–6951.

## CHAPTER 2

### EXPERIMENTAL TECHNIQUES

For our biomimetics research we prepared two types of biological entities - genetically engineered viruses (M13 and P22 bacteriophage) and bacterium (ethanol treated *Escherichia coli* (*E. coli*)). These were subsequently used as templates for the synthesis of highly ordered CdS and ZnS nanostructures via a general synthetic procedure. To characterize the virus- and bacterium-templated nanostructures, we have utilized various techniques, including scanning electron microscopy (SEM) coupled with energy-dispersive X-ray spectroscopy (EDS), transmission electron microscopy (TEM) coupled with high resolution (HR), confocal laser scanning fluorescence microscopy (CLSM), X-ray diffraction (XRD), and ultraviolet-visible spectroscopy (UV-Vis).

#### **2.1 Preparation of Biotemplates**

Filamentous bacteriophage M13 genetically engineered with specific binding peptide on the main coat protein (PVIII) were prepared for templating inorganic nanowires. Filamentous M13 bacteriophage is ~860 nm long and ~6.5 nm wide and 5 copies of its minor coat protein (PIII) and ~15 % of 2400 copies of its main coat protein (PVIII) are capable of displaying a foreign peptide.<sup>1</sup> Using phage display biopanning technique (see Chapter 3, Peptide Selection), we screened specific binding peptides from a combinatorial library of random peptide 12-mers fused to PIII proteins of bacteriophage M13 against different inorganic targets of interest. After inserting the encoding DNA of the selected peptide to the gp8 region of the viral DNA, the

peptide was expressed as a fusion protein on the surface of M13. Such engineered M13 with CdS-specific peptide were used as biotemplates for the synthesis of CdS nanowires.

Spherical self-assembly of the genetically engineered P22 coat protein was used for synthesis of high-ordered CdS and ZnS nanostructures. Viral P22 has an angular icosahedral structure which is ~64 nm in diameter, while the empty P22 shell is ~15 % smaller and more circular (seen Chapter 3, Fabrication of Ordered Nanostructures of Sulfide Nanocrystal Assemblies over Self-Assembled Genetically Engineered P22 Coat Protein). The structure of the protein assembly can be viewed as consisting of 60 hexamers clustered along with 12 pentamers at the vertices. Peptide sequences with strong affinity for the sulfides, ZnS (CNNPMHQNC) and CdS (SLTPLTTSHLRS), were inserted between P22 coat protein residues 182 and 183. On the resultant protein assembly, the engineered peptides lined the central channel of each of the pentamers and hexamers as dictated by the geometrical location of the original coat protein residue 182. These 72 engineered peptide groups symmetrically distributed over the whole protein assembly. Through the protein-directed nucleation of inorganic nanocrystals occurring at the engineered regions on the protein surface, we have achieved highly ordered sulfide nanostructures.

Ethanol-treated *E. coli* bacteria were used to template the growth of hollow sulfide nanostructures. *E. coli* is one of the longest rod-shaped bacteria and is by far the most well studied bacterial system. The genetic tools and cellular metabolisms associated with this bacterium are fairly well understood. The ethanol treatment is aimed to enhance the permeability of *E. coli* while retaining the morphology. One of the functions of the cell envelope is to protect the cells from environmental attack. Intact *E. coli* has a low permeability of the cell envelope due to the efflux pump inhibition<sup>2</sup> and thus will prevent the nucleation of inorganic materials on its

surface. The *E. coli* used as biotemplates were dispersed in 95 % ethanol for 3 minutes to dissolve the lipid layer of the outer membrane, thus enabling  $\text{Cd}^{2+}$  adsorption and reaction throughout the cell envelope.

The details regarding the amplification of bacteria and phages, ethanol treatment of *E. coli*, and molecular microbiological work on phages are described in Chapter 3 and 4.

## **2.2 General Synthetic Procedure of Bio-Templated CdS and ZnS Nanostructures**

In a typical reaction of virus-templated synthesis, a small amount of engineered bacteriophage solution was dispersed in aqueous metal cationic ( $\text{Zn}^{2+}$  or  $\text{Cd}^{2+}$ ) reagent for 12 hours, allowing sufficient time for the protein-metal (II) to interact. An aqueous  $\text{Na}_2\text{S}$  solution was then added to the above and the mixture held at room temperature for 2-12 hours. During this step, the protein-directed nucleation of sulfide nanocrystals occurs at the engineered regions of the protein surface, resulting in the growth of sulfide nanowires over the filamentous M13 template and spherical nanocrystal assembly on P22 template.

In a typical reaction of bacterium-templated synthesis, a small amount of ethanol-treated bacterium *E. coli* solution was first added to cadmium acetate dehydrate and after 30 minutes thioacetamide as a  $\text{S}^{2-}$  source was added. Upon the addition of thioacetamide,  $\text{H}_2\text{S}$  is gradually produced by sonochemical decomposition, which then reacts rapidly with the adsorbed cadmium ions to nucleate and grow CdS throughout the cell envelope. The reactions were conducted for different times (1 minute-4 hours) in an ultrasonic bath with the temperature maintained at around 28 °C. The time-dependence of the size, shape, and structure of the *E. coli*-templated CdS structures was investigated by varying the reaction time. By adjusting the sulfur/cadmium molar ratio, the crystal phase of the CdS product could be precisely controlled from cubic, mixture of

cubic and hexagonal, to pure hexagonal. The synthetic procedure has been extended to the synthesis of a variety of other sulfides, such as PbS, HgS, and ZnS.

The details of the experimental procedure are described in Chapter 3 and 4.

### **2.3 Scanning Electron Microscopy**

The scanning electron microscope (SEM) uses secondary electrons to form images of solid specimens. When high-energy incident electrons are decelerated in the solid sample, a variety of species, including secondary electrons are generated from electron-sample interaction, as shown in Figure 2.1. Each of these species has a different electron interaction volume, thus providing a range of information such as external morphology, chemical composition, crystalline structure and orientation. Such information can be collected by use of appropriate detectors. The secondary electrons are generated near the surface, have the best imaging resolution, and therefore commonly used for displaying the morphology and topography of samples. Conventional SEM techniques have magnification ranging from 20x-30,000x with spatial resolution of 50 to 100 nm, and are able to image areas ranging from approximately 1 cm to 5 microns in width.<sup>3</sup>

Most SEM equipments are coupled with energy-dispersive X-ray spectroscopy (EDS). By collecting the characteristic X-rays, SEM is capable of performing point analysis on the sample to qualitatively or semi-quantitatively determine chemical composition.

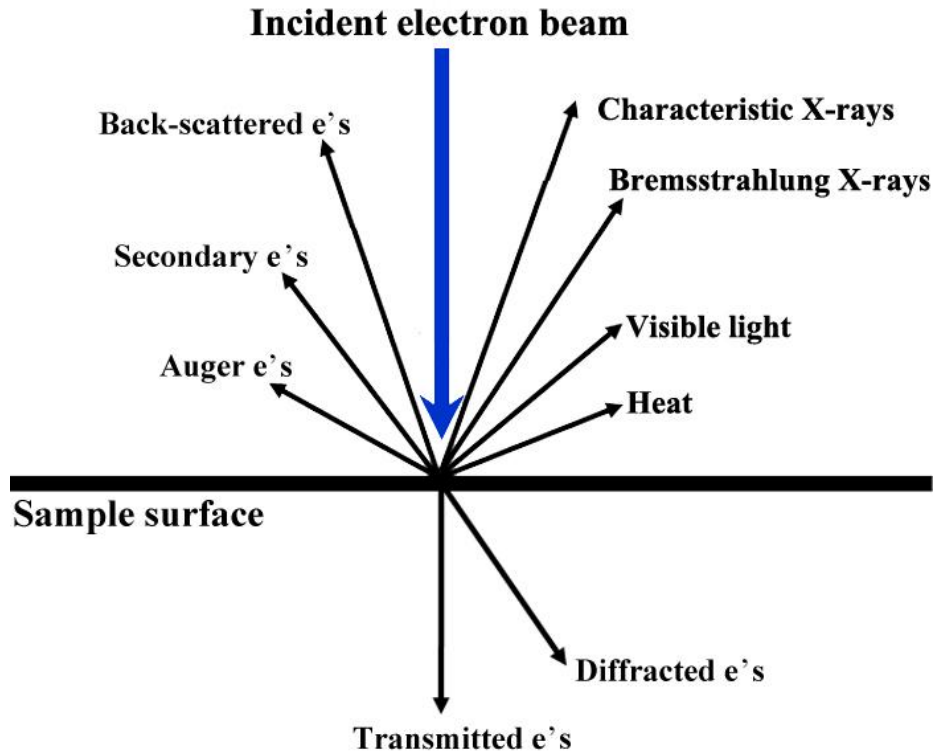


**Figure 2.1** Interaction between electrons and a sample. Adapted from ref. 4.

## 2.4 Transmission Electron Microscopy

The transmission electron microscope (TEM) is a high resolution (<10 nm) microscopy technique for examining the finer details of solid samples. The structure and basic principles of a TEM is shown in Figure 2.2. TEM usually uses a field-emission or thermionic source, which gives high quality results. In the vacuum column, the generated electron is then focused to a very thin electron beam through an electromagnetic lens and accelerated towards an ultra thin specimen. Upon interacting with the specimen, some of the electrons are backward scattered, but some of the electrons can transmit through the ultra thin specimen. These transmitted electrons finally strike a phosphor screen at the bottom of the microscope to generate an optical image. The transmitted electrons can also be detected by a charge-coupled device (CCD) camera. In the images, the darker areas represent thicker or denser areas of the sample from where fewer

electrons transmitted through. Similarly, the lighter areas of the image represent those thinner or less dense areas of the sample through which more electrons are transmitted. High resolution transmission electron microscopy (HR-TEM) image usually provides detailed information at the atomic level.

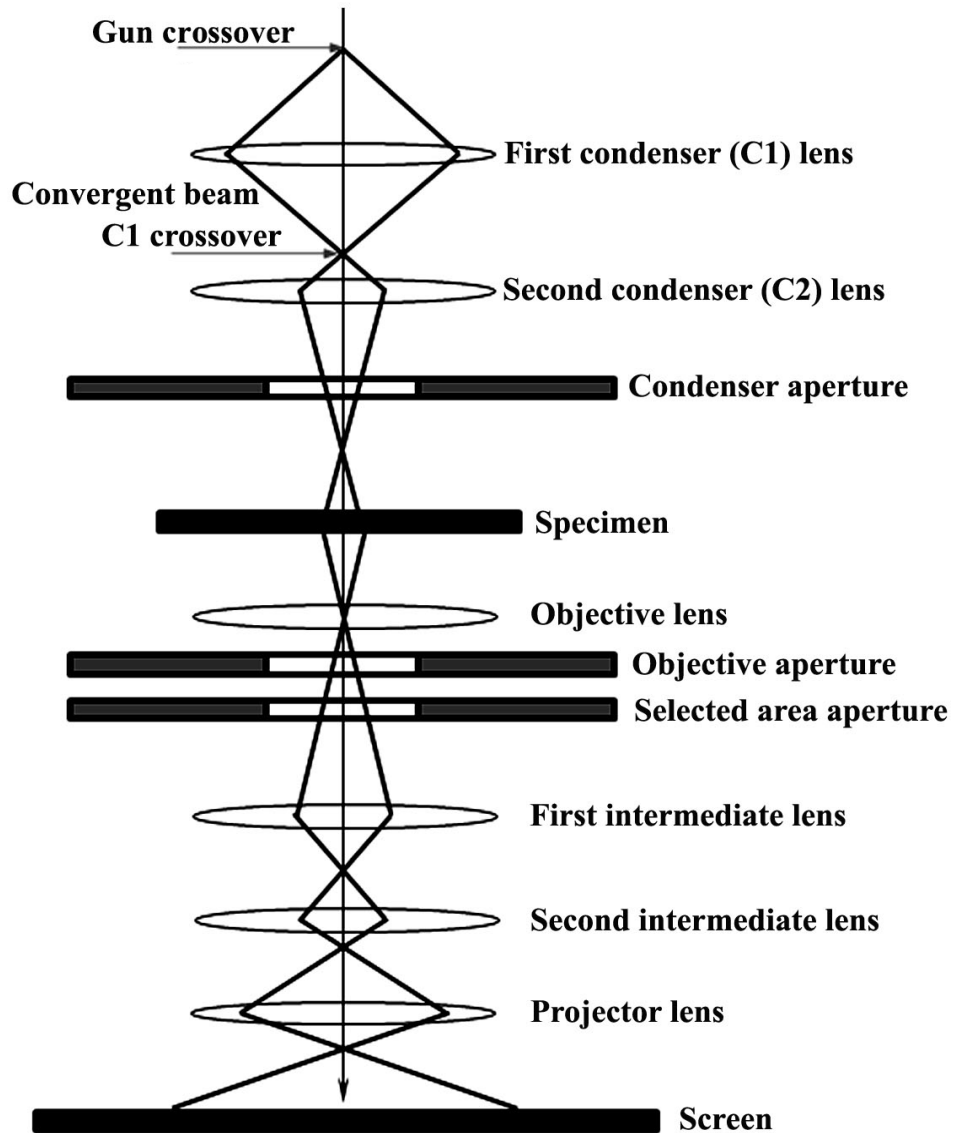


**Figure 2.2** A schematic diagram of a transmission electron microscope. Adapted from ref. 5.

Transmission electron microscope uses a set of electrostatic and electromagnetic converging lenses. By controlling the strength of the magnetic field, the electron beam is magnified and focused to generate the image and diffraction pattern. To protect the specimen from stray radiation (high angle scattered electrons), apertures are often inserted after the electron lenses. These include the condenser, objective, and selected area apertures. The role of the condenser aperture is to knock out high angle electrons. By changing the size of the condenser aperture, one can increase or decrease the beam strength. The objective aperture is used to block out high angle diffracted electrons, so as to enhance the contrast. The selected area aperture enables the user to examine the electron diffraction pattern of the selected area in the sample.

## **2.5 Confocal Laser Scanning Fluorescence Microscopy**

Confocal laser scanning microscopy (CLSM) is a technique for obtaining high-resolution optical images of micro-scale specimens. Different from conventional optical microscopes, confocal microscopes have a pinhole in front of the detector, as schematically depicted in Figure 2.3. The pinhole is able to block any signal coming from the out-of-focus planes, allowing light that originated from an in-focus plane to pass through. The focused laser beam selectively scans on or within a three dimensional specimen point by point, which is termed optical sectioning. Light signals are detected by a photomultiplier tube and then transformed into electrical signals to reconstruct the three dimensional structure. Signals from slower scans have a better signal-to-noise ratio, resulting in a better contrast and higher resolution.

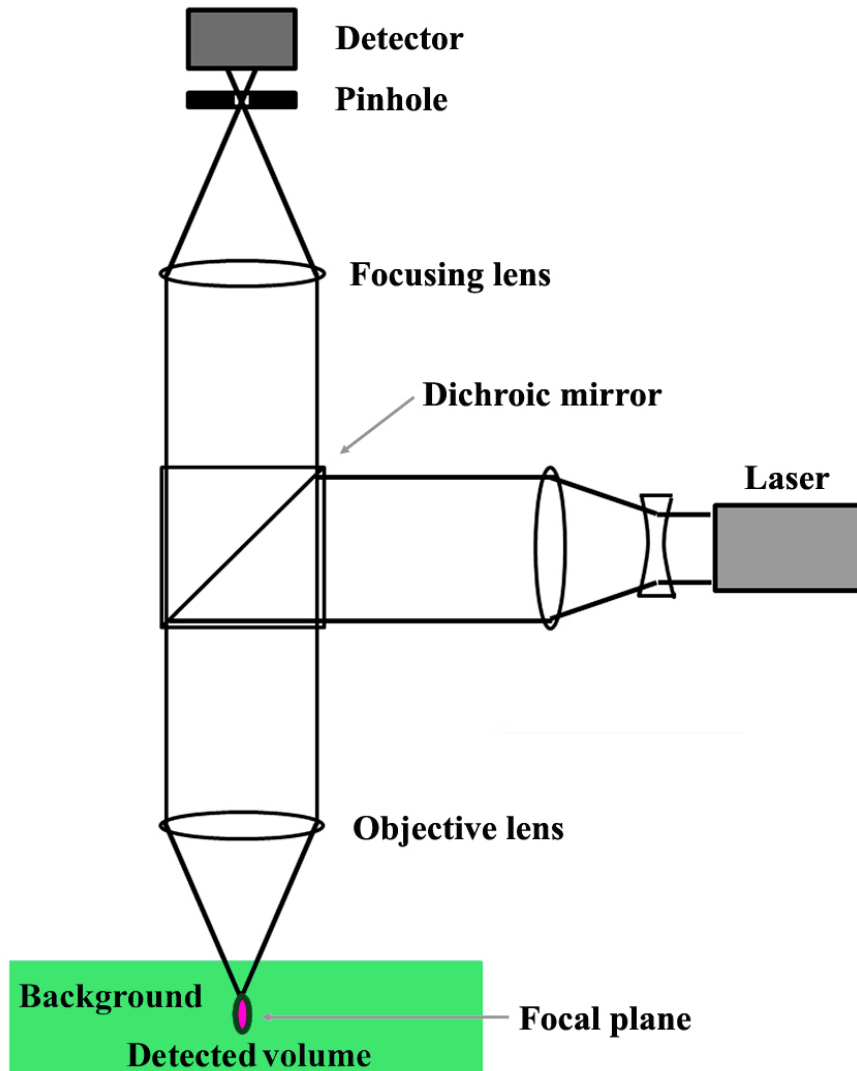


**Figure 2.3** Ray paths in a confocal laser scanning microscope.

Confocal laser scanning microscopy can be used for detecting biological specimens. In this case, specimens are generally tagged with a fluorescent marker or are intrinsically fluorescent. Through absorbing the excitation radiation, the specimen emits detectable fluorescence. During the measurement, a filter is used to selectively transmit the fluorescent wavelengths while blocking the original excitation wavelength.

## 2.6 X-Ray Powder Diffraction

X-rays are generated in an X-ray tube which contains a heated cathode and a target. Upon applying a high voltage field between the target and cathode, electrons emitted by the cathode are accelerated through the electric field and then bombard the target. The bombardment causes an energy transfer from electrons to atoms of the target. It can result in ejection of an electron from an inner energy level, leaving a vacant inner level. When an electron from an outer energy level falls into the vacant level, the excess energy is emitted as X-rays. The wavelengths of X-rays are in the range of 10 to 0.01 nm and are characteristic of the target. The transition from L to K shell causes the most intense radiation known as  $K\alpha$  line.

In crystalline solids, atoms are arranged in a regular and repetitive pattern with specific distances. Because the wavelengths of X-rays are comparable to the atomic spacing distances, incident X-rays will be scattered in all directions by the atoms. Constructive interference only occurs when scattered waves satisfy the Bragg's law:  $2d\sin\theta=n\lambda$ , where  $d$  is the interplanar distance,  $\theta$  is the scattering angle,  $n$  is an integer,  $\lambda$  is the wavelength. In the diffraction pattern from a crystalline solid, the position and intensity of the diffraction peaks thus depends on the unit cell and the type of atoms. Each crystalline solid has its unique characteristic X-ray powder pattern which can be used as a "fingerprint" for its identification. For an unknown crystallite, we can easily identify it by comparing its diffraction data with the JCPDS (Joint Committee on Powder Diffraction Standards) pattern database.

Nanocrystalline materials (typically  $< 100$  nm) often give broad diffraction peaks. In this case, the particle size can be estimated by the Scherrer equation:  $t=K\lambda/(\beta\cos\theta)$ , where  $t$  is the mean size of the nanoparticles,  $K$  is the shape factor (typically 0.9),  $\lambda$  is the X-ray wavelength

(1.54 Å for Cu target),  $\beta$  is the full width at half maximum intensity of the peak (FWHM), and  $\theta$  is the Bragg angle.

## 2.7 Ultraviolet-Visible Spectroscopy

In our research, ultraviolet-visible (UV-Vis) spectroscopy has been employed to determine the growth stage of bacterial cells, assess the concentration of proteins, estimate the purity of deoxyribonucleic acid (DNA), and monitor the structural evolution of bacteria *E.coli*-templated CdS.

In the presence of a growth medium, cell population goes through an exponential growth stage. For example, one *E. coli* cell divides into two cells in 20 minutes under optimal conditions. As the time passes, the overnight culture can contain  $\sim 10^9$  cells/mL at the stationary phase. The cell concentration can be calculated by counting cell plaques under a hemacytometer, but a spectrophotometer is more commonly used to examine the bacterial cell growth. The beam of light passing a cuvette with cell culture will be scattered more or less depending on the cell density, as shown in Figure 2.4. The absorbance reading is commonly taken as the optical density (OD) of a bacterial culture, which is proportional to the cell density. For the same cell culture, different spectrophotometers may give different optical density readings, depending on the distance between the sample and detector and geometry of the light beam. Therefore, a calibration for the number of cells per mL corresponding to a particular OD reading needs to be conducted before making the measurement of cell density.

Spectroscopy is a convenient method to quantify the concentration of a protein solution or estimate the purity of extracted DNA. Protein solution shows an absorbance peak at 280 nm ( $A_{280}$ ) due to the amino acids with aromatic rings. Nucleic acids strongly absorb at 260 nm

( $A_{260}$ ) because of their nitrogenous heterocyclic bases. The concentration of the protein solution with possible nucleic acid contamination is commonly calculated using the following equation:  $[\text{protein}] \text{ (mg/ml)} = (1.55 \times A_{280}) - (0.76 \times A_{260})$ . The ratio of the absorbance at 260 nm and 280 nm ( $A_{260/280}$ ) can be used to assess the purity of extracted DNA. A ratio of  $\sim 1.8$  is generally accepted as “pure” for DNA. An appreciably low ratio indicates the presence of protein, phenol, or other contaminants that strongly absorb around 280 nm.<sup>7</sup>

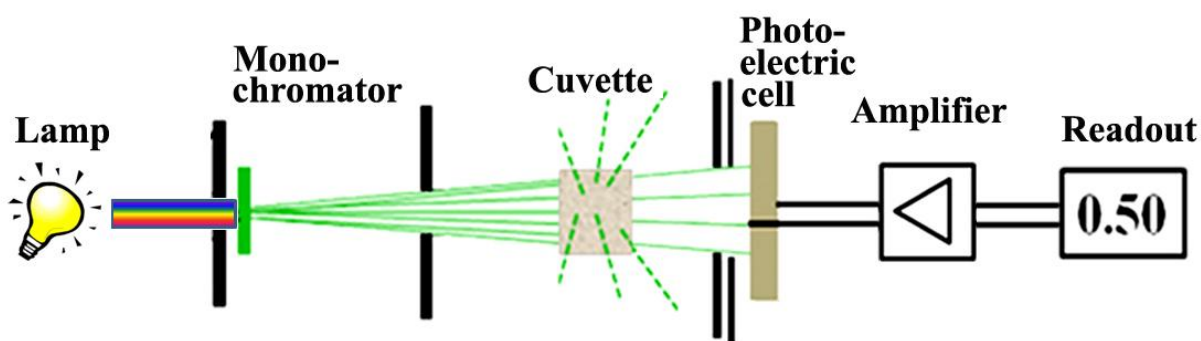


**Figure 2.4** Schematic demonstration of the measurement of the optical density on a spectrophotometer. Adapted from ref. 6.

UV-Vis spectroscopy is also a valuable tool for structural characterization of semiconductor nanoparticles because their band gap is size-dependent due to the quantum confinement effect. The optical absorption spectra shift to shorter wavelengths with decreasing particle size. We thus utilized this technique for monitoring the structural evolution of CdS nanoparticles grown on the bacteria *E. coli* template.

## 2.8 Photoelectrochemical Cell

To investigate the catalytic activity of *E. coli*-templated hollow nanoporous CdS rods, a general photoelectrochemical cell was set up. An EG&G potentiostat was used to measure the

photoelectrochemical response of the fabricated photoanodes with a conventional three-electrode system comprising of a photoanode (the hollow nanoporous CdS rods deposited and annealed onto an ITO-coated glass substrate), an Ag/AgCl reference electrode, and Pt foil counter electrode. A Na<sub>2</sub>S-Na<sub>2</sub>SO<sub>3</sub> aqueous solution was used as the electrolyte. A solar simulator with an illumination intensity of one sun (AM 1.5, 100 mW/cm<sup>2</sup>) was used as the light source. A power meter was used to calibrate the input power before and after the photoelectrochemical measurements. The photoelectrochemical cell efficiency was used to evaluate the photoelectrochemical activity of the synthesized materials. The details of the measurements and results are described in Chapter 4.

## 2.9 References

1. Kay, B. K.; Winter, J.; McCafferty, J. in *Phage Display of Peptides and Proteins: A Laboratory Manual*, Academic Press, **1996**.
2. Mehra, R. K.; Winge, D. R. *J. Cell Biochem.* **1991**, *45*, 30-40.
3. [http://serc.carleton.edu/research\\_education/geochemsheets/techniques/SEM.html](http://serc.carleton.edu/research_education/geochemsheets/techniques/SEM.html)
4. [http://serc.carleton.edu/research\\_education/geochemsheets/electroninteractions.html](http://serc.carleton.edu/research_education/geochemsheets/electroninteractions.html)
5. Williams, D. B.; Cater, C. B. in *Transmission Electron Microscopy, A Textbook for Materials Science*, Springer Science+Business Media, Inc. **1996**.
6. <http://elchem.kaist.ac.kr/vt/chem-ed/spec/uv-vis/uv-vis.htm>
7. Nanodrop Technical Support bulletin.

## CHAPTER 3

### PEPTIDE SELECTION USING PHAGE DISPLAY BIOPANNING AND FABRICATION OF ORDERED NANOSTRUCTURES OF SULFIDE NANOCRYSTAL ASSEMBLIES OVER SELF-ASSEMBLED GENETICALLY ENGINEERED P22 COAT PROTEIN

Reproduced in part with permission from [Journal of the American Chemical Society], submitted for publication. Unpublished work copyright [2010] American Chemical Society.

#### 3.1 Introduction

Ordered nanoparticle assemblies are of considerable interest because of their novel collective properties and potential applications in diverse areas such as catalysis, drug delivery, biomedicine, composites, etc.<sup>1-5</sup> A major challenge in the assembly of nanoparticles lies in the development of controllable synthetic strategies that can enable growth and assembly of target nanoparticles with high selectivity and good controllability.<sup>6-7</sup> Biological systems ranging from microbes to complex multicellular systems are known to possess intrinsic recognition mechanisms for inorganic species and sophisticated self-assembly processes, as evidenced by the synthesis of linear arrays of magnetic Fe<sub>3</sub>O<sub>4</sub> nanoparticles in magnetotactic bacteria, amorphous silica with species-specific pattern in diatoms, tough nanostructured hybrids of shells and bones in multicellular organisms, etc.<sup>8-9</sup> As a step toward mimicking some of these biological self-assembly processes, a variety of organisms have been exploited in recent years as templates for the construction of intricate nanostructures with controlled size, shape, structure, and functionality.<sup>10-13</sup>

Proteins play a key role for the growth of inorganic materials in biological systems under relatively mild conditions, which are quite different from the thermodynamic conditions in general chemical syntheses. Thus, proteins have been extracted from organisms to be used as templates or catalysts for the synthesis of inorganic materials *in vitro* under mild conditions. For

example, the repeat unit of silaffin protein identified from the diatom *Cylindrotheca fusiformis*, R5 peptide (H<sub>2</sub>N-SSKKSGSYSGSKGSKRRIL-COOH), can catalyze the precipitation of silica within seconds when added to a solution of silicic acid under ambient conditions *in vitro*.<sup>14</sup> Since their ease of functionalization, specific recognition and interaction with diverse materials, and ability to self-assemble as exhibited in natural biomineralization processes, peptides and proteins have been quite extensively investigated during the early phase of research in biomimetic synthesis.<sup>15-16</sup> A number of protein architectures, such as apoferritin, heat shock protein, and cowpea chlorotic mottle virus, have been studied for the growth of uniform nanoparticles including metals, semiconductors, and magnetic oxides.<sup>17-23</sup> The intrinsic inner nanometer-size cavity of such protein cages helps to spatially constrain the growth of the nanoparticles/nanocrystals and results in very good homogeneity in the resultant size and shape. Through proteins, numerous microorganisms are able to synthesize inorganic materials that are hierarchically organized from the nano- to the macroscale. However, most of the natural biomineralizing peptides identified so far are limited to those binding to inorganic components which are naturally abundant. Their extraction is also constrained by conventional biological procedures.

In order to fabricate complex inorganic nanostructures using protein templates, more effort has been devoted to protein surface modification to enhance the binding affinity for creating interesting nanostructures of designed materials.<sup>24-25</sup> Belcher's group was one of the first to express specific peptides, screened out using combinatorial phage display library, on filamentous M13 bacteriophage for biosynthesis.<sup>26-28</sup> The results from their group and others indicate that the addition of specific peptides can greatly enhance the selectivity and binding affinity of protein templates for inorganic material synthesis.<sup>24-28</sup> To date, a large number of peptides have been

screened for specific binding affinity to different substrates, including metals, oxides, and semiconductors.<sup>29-36</sup> The synthesized inorganic materials include nanoparticles<sup>26-27</sup> and in particular, interesting nanostructures of nanowires and double helical superstructure of nanoparticle assemblies over self-assembled peptides.<sup>28, 37-38</sup> Moreover, the use of self-assembling engineered proteins is promising for use as a biomimetic scaffold for achieving the rational control of ordered inorganic nanostructures with designed components and architectures.<sup>6-7, 39-40</sup>

In the first part of this chapter, we described the identification of CdS- and TiO<sub>2</sub>-binding peptides by using phage display biopanning. The specific binding affinity between organic molecules and inorganic components has been analyzed based on the chemical and physical properties of both the amino acids of the peptides and the inorganic materials. In the second part of this chapter, we demonstrate the fabrication of ordered nanostructures of sulfide nanocrystal assemblies over the self-assembled genetically engineered P22 coat protein. The high-affinity ZnS- and CdS-binding peptides, identified by phage display biopanning, enable the selective nucleation and growth of sulfides over the complex protein assemblies. The synthetic strategy can be extended to the fabrication of a variety of desired nanostructures.

### **3.2 Peptide Selection Using Phage Display Biopanning**

Phage display biopanning was originally developed for the selection of antibodies for pharmaceutical use.<sup>41-42</sup> This powerful selection technique has recently been adopted in screening inorganic-specific peptides. A combinatorial library of random peptide 9- or 12- mers fused to a minor coat protein (PIII) of bacteriophage M13 is commonly used in phage display biopanning. The peptide selection procedure involves four steps (Figure 3.1): (1) preparing a

combinatorial library of random peptides expressed as a fusion with the coat protein of a bacteriophage and displayed on the surface of the virion; (2) incubating the library of phage displayed peptides with desired inorganic materials; (3) washing away unbound phages from the surface of inorganic materials; (4) eluting the bound phages in a low pH elution buffer. The eluted phages are amplified and subjected to additional biopanning rounds. Peptide sequences with strong binding affinity against the inorganic materials will be enriched after several rounds of biopanning. Finally, the peptide sequence is available by decoding the DNA sequence of the selected phage.

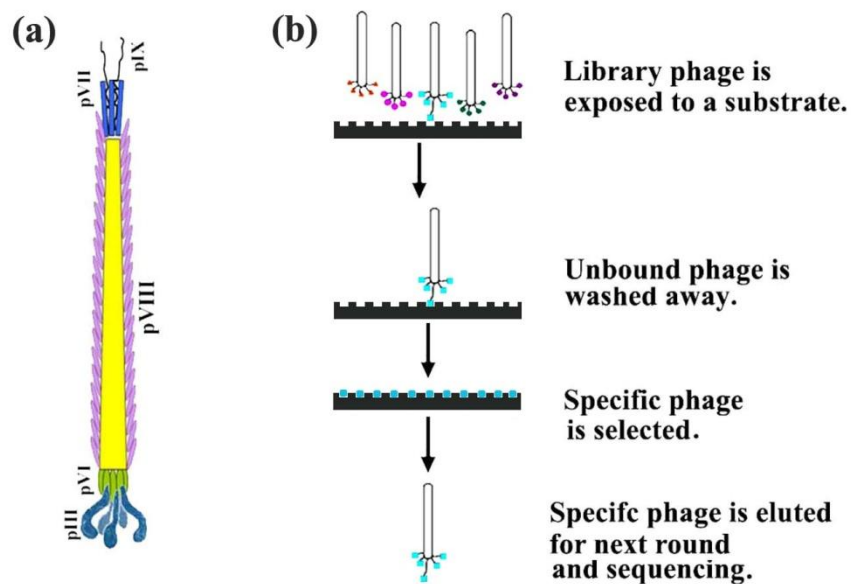


**Figure 3.1** (a) Schematic bacteriophage M13 and (b) biopanning with phage display peptide library. Adapted from ref. 43.

A number of peptides have been identified via phage display biopanning.<sup>29-36</sup> In a number of cases, the selected peptides do catalyze or template the synthesis of desired inorganic materials.<sup>26-28, 44-46</sup> However, our knowledge of the specific interaction between peptides and inorganic components is still limited to the collection of pieces of information. For example, A3 dodecapeptide (-Ala-Tyr-Ser-Ser-Gly-Ala-Pro-Pro-Met-Pro-Pro-Phe-), identified from a phage

display library, is able to synthesize and stabilize Au nanoparticles because amino acid tyrosine is known to reduce  $\text{HAuCl}_4$ .<sup>47</sup> Because of the lack of detailed knowledge, the complex interactions have been generally described as either hydrophobic interaction or hydrogen bonding.

In our work, we identified CdS- and  $\text{TiO}_2$ -binding peptides via phage display biopanning and then fused the CdS-binding peptide to the main coat protein (PVIII) of bacteriophage M13 for CdS nanowire formation. The specific binding affinity between organic molecules and inorganic components has been analyzed based on the chemical and physical properties of both the amino acids of the peptides and the inorganic materials. This research has enabled a better understanding of the combination mechanism between peptides and inorganic molecules, and provided basic knowledge about the fabrication of ordered nanostructures of sulfide nanocrystal assemblies over self-assembled genetically engineered P22 coat protein.

### **3.2.1 Experimental**

#### **3.2.1.1 Materials**

All phage display peptide libraries used for peptide selection were purchased from New England Biolabs and were used as-received. F88.4 vector and related cells (K91 and MC1061) were provided by Dr. George P. Smith of the University of Missouri. CdS and  $\text{TiO}_2$  single crystal substrates were purchased from CrysTec Kristalltechnologie, Germany. Anti-M13 monoclonal antibody and anti-Mouse IgG Cy3 conjugate antibody developed in sheep were obtained from Amersham Biosciences. All other chemicals for bacterial culture media and buffers were from Fisher Scientific and used as-received without any further purification.

### 3.2.1.2 Preparation of Inorganic Substrates

CdS single crystal wurzite substrates were cleaned in acetone for 15 min, isopropanol for 15 min, 0.05 M HCl for 1-2 min, and then rinsed with sterile deionized water before biopanning. The acid solution of 0.05 M HCl was replaced by HF:H<sub>2</sub>O (1:10) for cleaning TiO<sub>2</sub> substrates. The surface characteristics and composition of the cleaned substrates were determined using scanning electron microscopy and X-ray photoelectron spectroscopy.

### 3.2.1.3 Peptide Selection

The phage display biopanning procedure followed the protocol manual provided by New England Biolabs. In a typical round, 10 µL of the phage display library was added to a piece of cleaned crystal substrate submerged in 1 mL of 50 mM tris-buffered saline (TBS) containing 0.1 % (v/v) Tween-20 (0.1 % TBST). Tween is used to decrease the binding of unspecific peptides to the substrate. After rocking the sample in a tube for 1 h at room temperature, the surface of the substrate was washed 10 times with TBS (pH 7.5) to get rid of unbound phages. The remaining binding phages were eluted from the surface by the addition of elution buffer glycine-HCl (pH 2.2). After rocking for 8 min, the eluted phages were transferred to a fresh tube and then neutralized with Tris-HCl (pH 9.1). The neutralized phage was amplified and subjected to the next panning round. Up to five biopanning rounds is usually conducted for selecting strong binding sequences, while increasing the concentration of Tween-20 from 1 % to 5 %.

The eluted phages were titred after each round and were sequenced from the third round. To enrich the phages for titrating and sequencing, the eluted phages were incubated with their host *Escherichia coli* (*E. coli*) ER2738 and plated on LB Xgal/IPTG plates. Since the library phage was derived from the cloning vector M13mp19, which carries the *lacZα* gene, phage plaques

appear blue in color when plated on media containing Xgal (5-bromo-4-chloro-3-indoyl- $\beta$ -D-galactoside) and IPTG (isopropyl- $\beta$ -D-thiogalactoside). The appearance of white plaques usually indicates contamination from environmental filamentous phage. Blue plaques were collected and DNA sequenced.

#### **3.2.1.4 Affinity Assay**

0.2 mL of diluted anti-M13 monoclonal antibody, which can recognize the main coat protein PVIII of bacteriophage M13 to form a specific complex, was placed on top of phage-bound CdS substrate. The same amount of secondary antibody, diluted anti-mouse IgG Cy3 conjugate antibody developed in sheep, was applied on the above CdS substrate to cross-react with the primary antibody. Cy3 monofunctional dye attached to the secondary antibody is an orange fluorescent cyanine that produces an intense signal which can be easily detected using most rhodamine filter sets. The CdS substrate was exposed to TBS 10 times to get rid of unbound antibodies after each step. Because of the conjugated antibodies, the phage binding to the surface of CdS substrate can be visualized using a confocal fluorescence microscope. The combination of CdS substrate, phage and antibodies is demonstrated in Figure 3.2. The same procedure was carried out on a glass slide for comparison.

#### **3.2.1.5 Genetically Engineering Main Coat Protein of M13 Phage**

Double stranded replicative form (RF) DNA was extracted from F88.4 vector amplified from host K91. Short DNA insert, screened out via biopanning against a wurzite CdS substrate, was annealed to make it double stranded and then was ligated with RF DNA from the F88.4 vector. The ligates were further transformed into chemically competent MC1061. Filamentous phages

with specific peptides displayed on their main coat protein were finally secreted out from the transformed cells after incubation. The molecular microbiology work was carried out in Dr. Peter Prevelige's lab at the University of Alabama at Birmingham.

### **3.2.1.6 Synthesis of CdS Nanowires on Genetically Engineered M13 Phage**

In a typical reaction, 10  $\mu\text{L}$  of engineered phage solution was dispersed in 500  $\mu\text{L}$  of aqueous  $\text{ZnCl}_2$  (1 mM) for 12 h at room temperature. 500  $\mu\text{L}$  of aqueous  $\text{Na}_2\text{S}$  (1 mM) was then added to the above solution and the mixture was placed at room temperature with rocking for 12 h. All the experimental procedures were carried out in a fume hood with appropriate handling of the chemicals and biological samples for safety. The morphology of the products was characterized using transmission electron microscopy (TEM).

### **3.2.2 Results and Discussion**

The binding affinity of the selected phage displayed peptides to the wurzite CdS substrate was examined by applying Cys-labeled antibodies over phage-bound CdS substrate. Figure 3.3 shows the fluorescent images of a CdS substrate and a glass slide. Both the CdS substrate and the glass slide have been treated with selected phages and antibody (see experimental details in 3.2.1.4 Affinity Assay). There was no fluorescent signal observed on the surface of the glass slide, as shown in Figure 3.3a. This is because the phages used for affinity assay were specifically selected against the wurzite CdS rather than the glass and could not remain on the surface of glass after stringent washing. The fluorescent-labeled antibodies thus could not stick onto the surface of the glass without the presence of antigenic proteins. Contrarily, CdS substrate emits a strong fluorescent signal, as shown in Figure 3.3b. The primary antibody, anti-M13

monoclonal antibody, can specifically recognize the main coat protein, so the fluorescent signal generated from its conjugated secondary antibody indicates that the washed CdS substrate still has phages strongly bound to it. Figure 3.3c and 3.3d shows fluorescent images of one corner of the CdS substrate and one from top of the same substrate, respectively. The bright uniform fluorescent color indicates that the selected phages evenly bind onto the entire surface of the substrate.

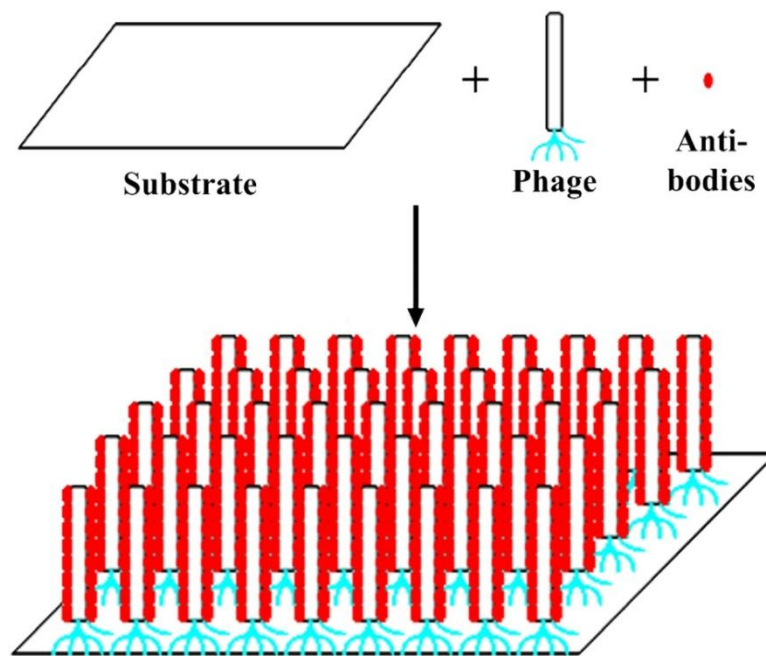


**Figure 3.2** Schematic affinity assay.

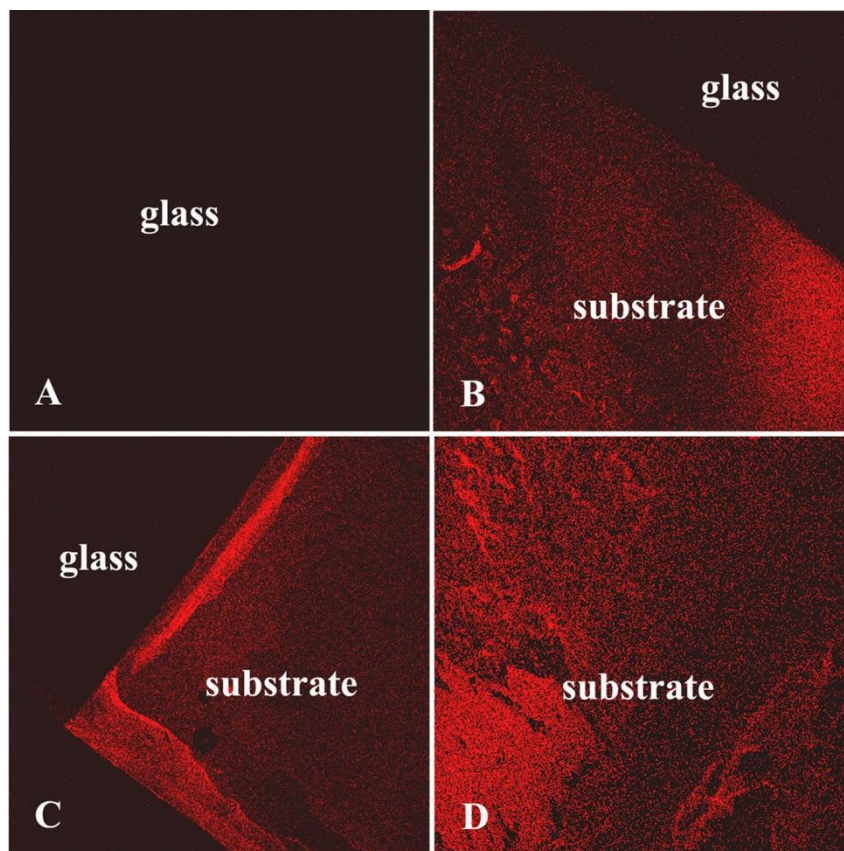


**Figure 3.3** Confocal fluorescent microscope images of (A) a glass slide and (B-D) a CdS substrate treated with selected phages and antibodies.

The specific peptide sequences responsible for binding to the CdS substrate were deciphered through sequencing their encoding DNA. Tables 3.1 and 3.2 show the obtained peptide sequences after three rounds (R3) and five rounds (R5) of biopanning, respectively. Twelve amino acids of each peptide are distinguished by different colors based on the polarity of their side chains (or R groups) at pH 7: polar, uncharged R groups including serine (S), threonine (T), cysteine (C), asparagine (N), glutamine (Q), are indicated in blue color; positively charged R groups including lysine (K), arginine (R), histidine (H), are indicated in pink color; negatively charged R groups including aspartate (D) and glutamate (E) are indicated in green color; nonpolar, aliphatic R groups (glycine (G), alanine (A), proline (P), valine (V), leucine (L),

Isoleucine (I), methionine (M)) and aromatic R groups (phenylalanine (F), tyrosine (Y), tryptophan (W)) are marked in black color. In order to analyze the trend of selected peptides, the ratio of amino acids of each color over the total residues has been calculated. The calculated results for R3 peptides listed in Table 3.1 are shown as follows:

1. Polar, uncharged R groups (S, T, C, N, Q):  $22/108=20.37\%$ .
2. Positively charged R groups (K, R, H):  $36/108=33.33\%$ .
3. Negatively charged R groups (D, E):  $0/108=0\%$ .
4. Non-polar and aromatic R group (G, A, P, V, L, I, M, F, Y, W):  $50/108= 6.30\%$ .

Similar calculation was carried out for the R5 peptides shown in Table 3.2:

1. Polar, uncharged R groups (S, T, C, N, Q):  $23/120=19.17\%$ .
2. Positively charged R groups (K, R, H):  $45/120=37.5\%$ .
3. Negatively charged R groups (D, E):  $6/120=5.0\%$ .
4. Non-polar and aromatic groups (G, A, P, V, L, I, M, F, Y, W):  $46/120=38.33\%$ .

The above calculations show that the peptides selected after three rounds (Table 3.1) and five rounds (Table 3.2) of biopanning have a similar trend, namely a relatively high ratio of amino acids with positively charged R groups and a very low ratio of amino acids with negatively charged R groups. With the panning rounds increasing from three to five, the ratio of amino acids with positively charged R groups increased from 33.33 % to 37.5 %, which indicates that this category of amino acids plays a predominant role in substrate binding and thus has been enriched with additional rounds of panning. We also confirmed the preference of positively charged R groups by calculating the net charge of each peptide sequence, as shown in the last column in Tables 3.1 and 3.2. It is notable that all peptide sequences have positive net charge. We thus postulate that the strong affinity between these peptides and the CdS substrate is

attributed to the interaction of their positively charged side chains with the solid surface. The domination of positive net charge was also observed in the CdS-, ZnS- and PbS-binding peptides selected by Dr. Belcher's group.<sup>26</sup>

**Table 3.1** CdS-specific peptide sequences after three rounds (R3) of biopanning

		Pos1	Pos2	Pos3	Pos4	Pos5	Pos6	Pos7	Pos8	Pos9	Pos10	Pos11	Pos12	Net Charge
Clone #	1	K	P	P	H	A	T	K	A	T	L	P	S	+3
	2	K	P	I	S	H	H	P	H	H	R	A	W	+6
	3	K	P	T	K	H	I	N	Y	L	P	G	P	+3
	4	G	P	H	L	P	K	L	T	K	F	P	K	+4
	5	A	K	S	S	Q	H	I	H	K	G	L	S	+4
	6	K	P	A	S	H	N	H	L	K	P	A	L	+4
	7	K	P	V	H	N	Y	L	Q	K	K	I	H	+5
	8	G	P	H	K	P	P	K	S	P	P	T	L	+3
	9	G	K	M	H	Q	H	L	N	S	R	T	Q	+4

**Table 3.2** CdS-specific peptide sequences after five rounds (R5) of biopanning

		Pos1	Pos2	Pos3	Pos4	Pos5	Pos6	Pos7	Pos8	Pos9	Pos10	Pos11	Pos12	Net Charge
Clone #	1	K	P	H	T	H	Y	A	N	K	D	P	R	-4
	2	K	P	P	S	K	H	T	I	I	W	N	S	-3
	3	G	K	T	K	H	D	S	H	R	K	H	M	-6
	4	G	P	H	S	P	K	H	R	I	H	P	N	-5
	5	L	E	A	K	A	K	Q	H	R	D	L	T	-2
	6	K	P	L	H	K	P	P	H	V	S	T	V	-4
	7	K	P	P	R	T	P	A	M	H	L	A	G	-3
	8	K	P	S	P	H	H	H	H	S	E	R	M	-5
	9	K	P	I	K	H	L	Q	H	S	L	T	H	-5
	10	G	K	L	K	N	D	K	Y	Q	F	Y	T	-2

In order to understand the preference of peptides with positively charged R groups, we investigated the influence of the crystalline structure of CdS. The CdS substrate used in biopanning is of wurzite structure with (0001) orientation, as shown in Figure 3.4a. In  $\langle 0001 \rangle$  direction, the exposed planes can be either Cd or S dominated faces. But the use of diluted HCl in the substrate cleaning process will likely consume all surface Cd cations and result in the

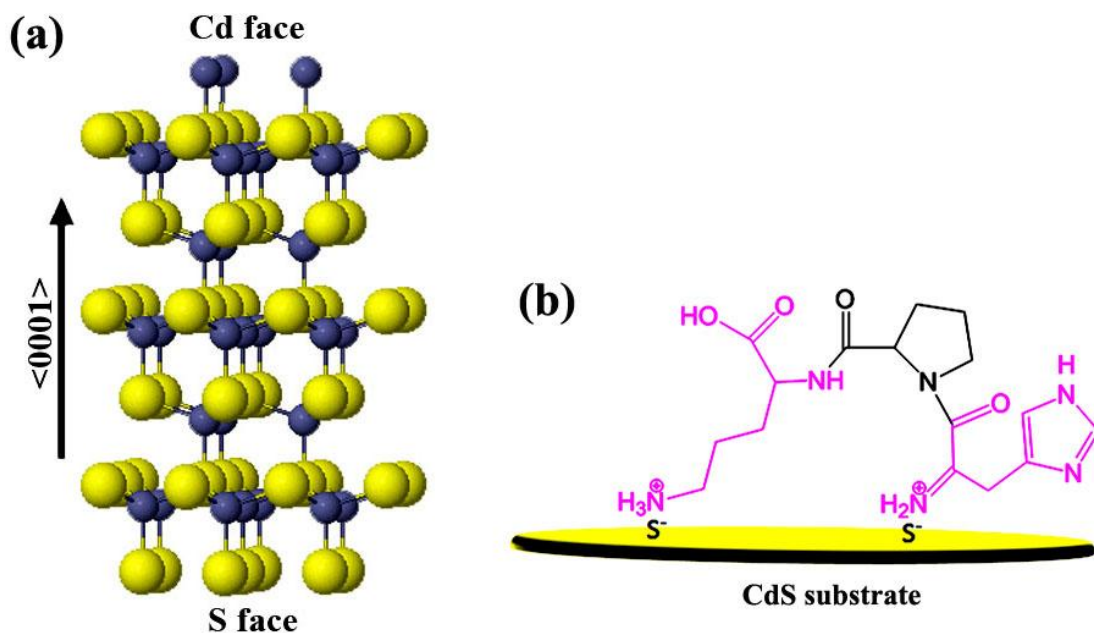


**Figure 3.4** Schemes of (a) the wurzite CdS and (b) the interaction between CdS substrate and amino acids with positively charged R groups.

exposure of S face over the whole substrate surface. The positive R groups thus competitively attach to the surface of CdS substrate through electrostatic interaction with exposed S anions, as depicted as Figure 3.4b. We also notice the high frequency of proline (P) in these specific peptides. Proline differs from all the other standard amino acids in actually being an  $\alpha$ -imino acid, which causes kinks in the chain. The cis-peptide bond of proline may therefore enable the functional amino acids to approach the substrate surface, instead of floating freely.

We also investigated the interaction between rutile TiO<sub>2</sub> substrates and their specific peptides. Two types of TiO<sub>2</sub> substrates, with (110) and (100) orientations, were used in biopanning (their selected peptides are listed in Tables 3.3 and 3.4). For the TiO<sub>2</sub> (110) substrate, there are 13 of 17 clones sharing one identical peptide sequence, SVSVGMKPSRP (Clone 1 in Table 3.3). For the TiO<sub>2</sub> (100) substrate, 10 of 17 clones have the same sequence, SVSVGMKPSRP (Clone 4 in Table 3.4). It is interesting that the dominant binding peptides for rutile TiO<sub>2</sub> (110) and (100) are actually the same, which indicates that the interactions between peptides and the two different rutile surfaces are probably similar. From Tables 3.3 and 3.4, we

**Table 3.3** TiO<sub>2</sub> (110)-specific peptide sequences after five rounds (R5) of biopanning. The peptide sequence in Clone 1 was observed in 13 clones.

		Pos1	Pos2	Pos3	Pos4	Pos5	Pos6	Pos7	Pos8	Pos9	Pos10	Pos11	Pos12
Clone #	1	S	V	S	V	G	M	K	P	S	P	R	P
	2	H	P	L	H	T	K	P	L	V	S	S	S
	3	L	T	Q	P	Q	D	I	P	V	F	R	S
	4	K	A	L	N	L	P	N	R	P	L	G	T
	5	T	L	P	S	P	L	A	L	L	T	V	H

**Table 3.4** TiO<sub>2</sub> (100)-specific peptide sequences after five rounds (R5) of biopanning. The peptide sequence in Clone 4 was observed in 10 clones.

		Pos1	Pos2	Pos3	Pos4	Pos5	Pos6	Pos7	Pos8	Pos9	Pos10	Pos11	Pos12
Clone #	1	T	T	S	S	V	H	G	T	P	S	R	M
	2	D	S	P	S	Y	K	A	I	P	G	A	S
	3	G	S	M	S	P	Y	V	R	W	Y	T	P
	4	S	V	S	V	G	M	K	P	S	P	R	P
	5	S	A	V	T	V	P	M	P	Y	K	Y	L
	6	V	Y	S	S	T	T	R	P	L	P	S	P
	7	S	L	A	S	Q	P	T	L	R	L	I	G
	8	A	H	S	T	S	T	P	A	L	L	P	W

find that amino acids with polar uncharged R groups and positively charged R groups are preferred, indicating that these amino acids play a key role in the attachment to TiO<sub>2</sub> substrates.

For single-crystal rutile substrates, even if they are carefully prepared the crystal surface is quite defective,<sup>48</sup> the surface of TiO<sub>2</sub> substrate thereby can be easily hydrolyzed in aqueous solution.<sup>49</sup> Amino acids with polar uncharged R groups and positively charged R groups thus can bind to the hydroxyl groups on the surface of TiO<sub>2</sub> substrates through hydrogen bonds, as depicted in Figure 3.5.

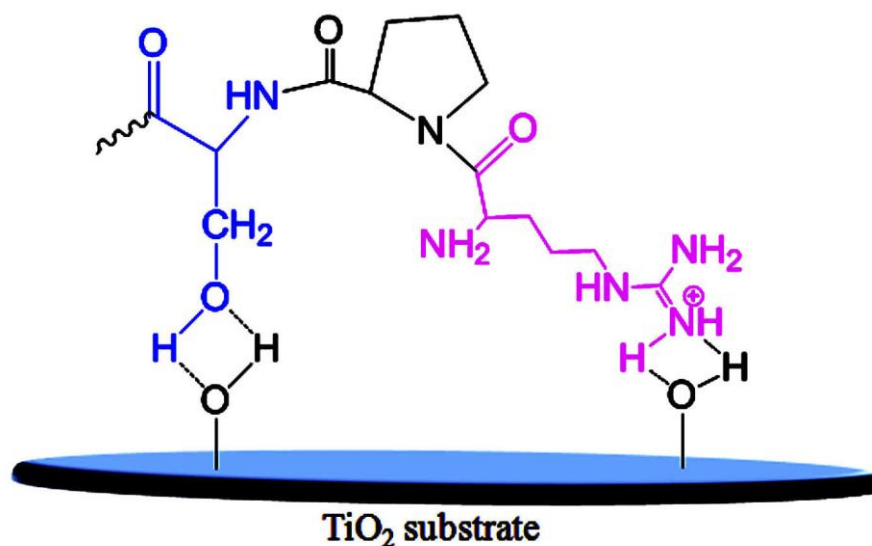


**Figure 3.5** Schemes of the interaction between the hydroxyl groups on the TiO<sub>2</sub> substrate and the amino acids with polar side chains.

It is plausible that these chemical interactions between the functional amino acids and the hydroxyl groups on the rutile TiO<sub>2</sub> substrates are not the only factor in determining the binding affinity. Peptides containing several consecutive functional amino acids, such as Clone 2 in Table 3.3 and Clones 1, 6, and 8 in Table 3.4, surprisingly do not appear as the strongest binding sequences. We thus postulate that the peptide structure is another important factor in determining the binding affinity. The distance between two C $\alpha$  is around 3.6 Å<sup>50,51</sup> and the lattice parameter of rutile TiO<sub>2</sub> is  $a=b=4.5845\text{Å}$ ,  $c=2.9533\text{Å}$ .<sup>52</sup> In the case of all functional amino acids in a consecutive pattern, the peptide will be in a rigid conformation in order to interact with the

adjacent surface hydroxyl groups on the surface of TiO<sub>2</sub>. Furthermore, the polar R groups of two adjacent amino acids may form hydrogen bond between them, instead of interacting with the surface hydroxyl groups, and thus decrease the binding affinity of the entire peptide. Therefore, in the dominant peptide the functional amino acids are spaced apart by interval residues, such as V and P, providing the flexibility for better matching with the crystal structure of TiO<sub>2</sub>. The cis-peptide bond of proline may act as a bridge between two functional amino acids which interact with two most adjacent hydroxyl groups on TiO<sub>2</sub> substrate. Having five separated functional amino acids along with three proline linkages, the peptide sequence SVSVGMPKPSRP therefore possesses the strongest affinity for TiO<sub>2</sub> substrates.

We finally investigated the recognition property of selected peptides in biomimetics. For this purpose, CdS-binding peptide, GPHSPKHRIHPN (Clone 4 in Table 3.2), was expressed on the main coat protein PVIII of bacteriophage M13 via inserting the encoding DNA into the vector F88.4. The dimension of M13 is around 6.6 nm in diameter and 880 nm in length.<sup>53</sup> Figure 3.6a shows a TEM image of uranyl acetate (2 %) stained M13. The phage-templated CdS nanowires replicated the morphology of the phage (Figure 3.6b), which indicates that the displayed peptide is able to template the synthesis of CdS. Such nanowire morphology was not observed with using wild type M13 as template (Figure 3.6c) or in the absence of any type of phage in the reaction (Figure 3.6d).

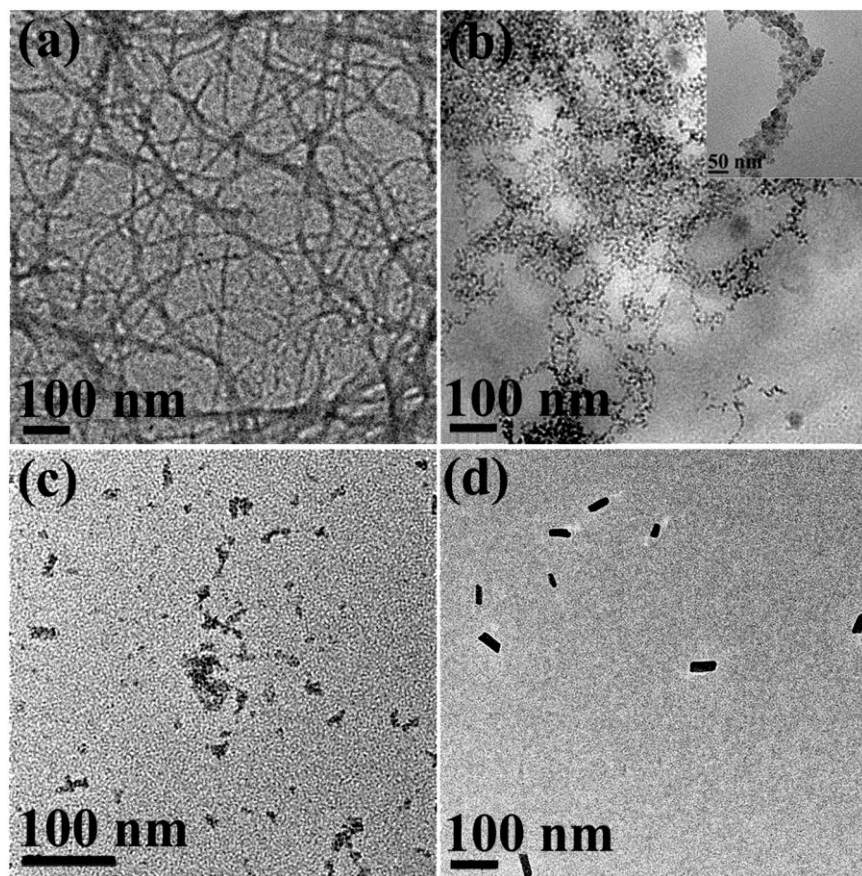


**Figure 3.6** TEM images of (a) filamentous bacteriophage stained by 2 % uranyl acetate. (b) CdS nanowires grown on the engineered phage; insert: one single nanowire. (c) CdS agglomerates obtained in the presence of wild phage. (d) CdS nanoparticles obtained in the absence of any type of phage.

### 3.2.3 Conclusion

Specific binding peptides for wurtzite CdS and rutile TiO<sub>2</sub> were selected via phage display biopanning technique. The recognition ability of CdS-specific peptides to the substrate has been examined with the aid of labeled antibodies. The binding mechanisms between CdS- and TiO<sub>2</sub>-specific peptides and the inorganic templates have been analyzed on the basis of the natural properties of amino acid side chains and the crystalline structure of the substrates. The successful growth of CdS nanowires over genetically engineered M13 phages indicates that the selected

peptides can be engineered onto other organisms to template various architectures with desired components.

### **3.3 Fabrication of Ordered Nanostructures of Sulfide Nanocrystal Assemblies over Self-Assembled Genetically Engineered P22 Coat Protein**

Lysogenic bacteriophage P22 has been intensively studied in virus assembly since it was discovered in 1952. In a typical P22 virus assembly process (Figure 3.7a), 420 copies of the P22 coat protein of MW around 47 kDa start to assemble with the aid of approximately 300 copies of the 33.6 kDa scaffolding protein to form an icosahedral  $T=7$  P22 procapsid.<sup>54-57</sup> The icosahedral procapsid has a diameter of 58 nm. Then the scaffolding proteins exit and dsDNA packages through a portal complex. In this process the procapsid undergoes a structural transformation and finally forms mature virion of 64 nm diameter. Compared to angular P22 mature virion, an empty P22 procapsid is ~15 % smaller and more circular. The circular to angular structural transformation can be mimicked *in vitro* by gentle heating (65 °C for 10 min), while an extended heating (75 °C,  $\geq$  20 min) can induce the release of the twelve five-fold icosahedral vertices, leaving a 10 nm hole at each of the vertices (Figure 3.7b).<sup>58</sup>

In this section, we demonstrate the fabrication of ordered nanostructures of nanocrystal assemblies over self-assembled genetically engineered P22 coat protein. This biotemplated construction involves two steps: (1) the self-assembly of spherical protein templates from genetically engineered P22 coat proteins; and (2) the nucleation and growth of nanocrystals on the self-assembled protein templates. We have used ZnS and CdS grown on the engineered P22 coat protein assembly as a model system since binding peptides with strong affinity for these sulfides have been identified. Furthermore, the structure and assembly of the P22 coat proteins is

reasonably well understood. The synthetic strategy is quite general and can be extended to the fabrication of a variety of other nanostructures.

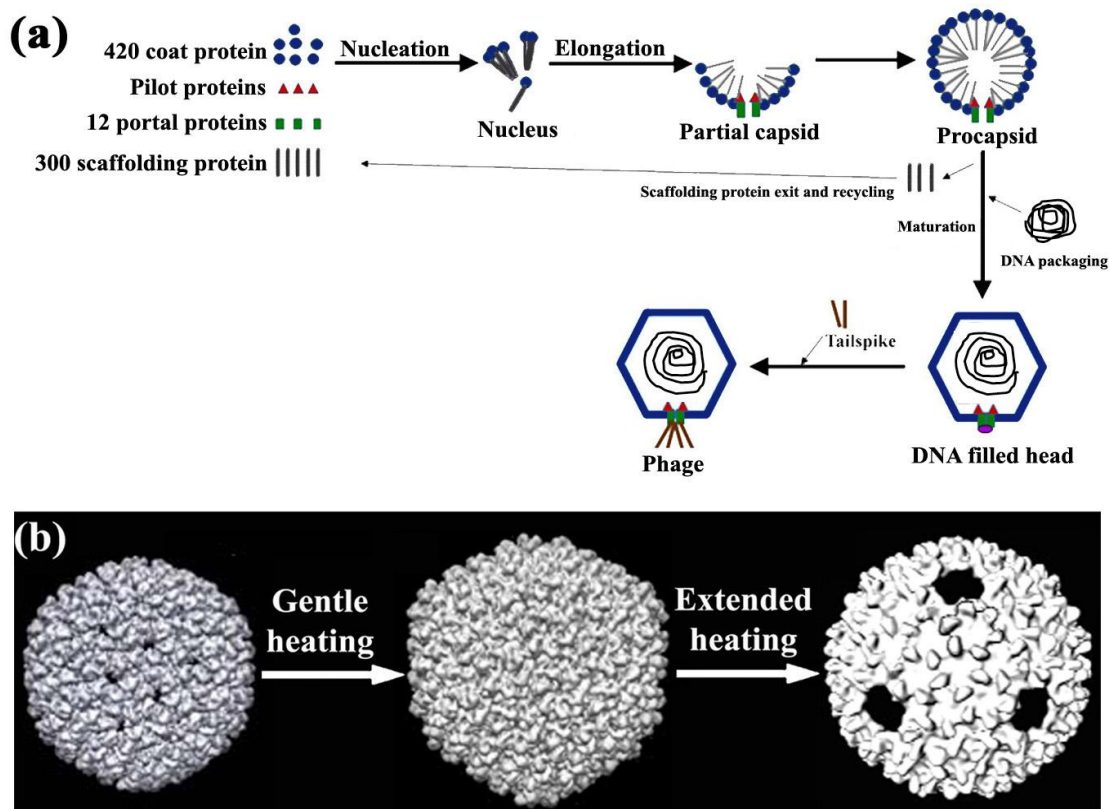


**Figure 3.7** (a) Assembly pathway of bacteriophage P22 showing the proteins involved and the nucleation, elongation and maturation reactions. Adapted from ref. 57. (b) Structural transformation of empty P22 procapsid. Reproduced with permission from ref. 58.

### 3.3.1 Experimental

#### 3.3.1.1 Materials

The synthesis of ZnS and CdS was carried out using commercially available reagents. Sodium sulfide ( $\text{Na}_2\text{S}$ ) and cadmium acetate ( $\text{Cd}(\text{CH}_3\text{COO})_2$ ) were purchased from Acros Organics and zinc acetate ( $\text{Zn}(\text{CH}_3\text{COO})_2 \cdot 2\text{H}_2\text{O}$ ) was obtained from Fisher Scientific. All the chemicals were used as-received without any further purification.

### **3.3.1.2 Preparation of Genetically Engineered Bacteriophage P22 Coat Protein Assemblies.**

Two peptide sequences, CNNPMHQNC and SLTPLTTSHLRS, isolated by Belcher's group through screening of M13 phage display library and confirmed to have binding specificity to ZnS and CdS were used in this work.<sup>26</sup> The nucleotide sequence encoding the specific peptide was introduced into a pET-based plasmid encoding the bacteriophage P22 scaffolding and coat protein genes at coat protein residue 182 by PCR based mutagenesis as described previously.<sup>57</sup> The coat and scaffolding proteins were expressed in *E. coli* BL21 DE3 at 37 °C. Cells were harvested by centrifugation 3-4 hours after induction with 1 mM IPTG and lysed by repeated freeze-thaw cycles in 50 mM Tris, 100 mM NaCl, 20 mM MgSO<sub>4</sub>, pH 7.6. The lysate was clarified by centrifugation at 12,000 x g for 45 min and the supernatant containing the procapsid-like particles (PLPs) was centrifuged through a 20 % sucrose cushion at 185,000 x g for 2 h to pellet the procapsids. The procapsids were re-suspended in 0.5 M Guanidinium-Cl buffer to remove the scaffolding proteins and procapsid shells were pelleted at 40,000 x g for 1 h. The coat protein assemblies were re-suspended in 50 mM NaCl, 25 mM Tris, 2 mM EDTA, pH 7.6 and band purified by sucrose gradient centrifugation on a 5 mL 5-20 % sucrose gradient, followed by dialysis against 50 mM NaCl, 25 mM Tris, 2 mM EDTA, pH 7.6 to remove the sucrose.

### **3.3.1.3. Inorganic Synthesis over Genetically Engineered Bacteriophage P22 Coat Protein Assemblies.**

Genetically engineered bacteriophage P22 coat protein assemblies stored in EDTA buffer were 4,000x dialyzed against deionized water before being utilized as biosynthetic templates. Water based protein assembly solution (10 µL) was dispersed in 1 mL of aqueous Zn(CH<sub>3</sub>COO)<sub>2</sub>

(1 mM) for interaction at 4 °C for 12 h, allowing the protein-Zn(II) interaction. 1 mL of aqueous Na<sub>2</sub>S solution (1 mM) was then added into the above solution and the mixture was placed at room temperature for 2 h. Aqueous Cd(CH<sub>3</sub>COO)<sub>2</sub> (1 mM) was used as the Cd(II) source in the synthesis of CdS. All the reported experimental procedures were carried out in a fume hood with appropriate handling of the chemicals and biological samples for safety.

The morphology and structure of the products was observed using transmission electron microscopy (TEM) coupled with high resolution (HR) (Tecnai F-20).

### 3.3.2 Results and Discussion

Figure 3.8 demonstrates the formation of ordered sulfide nanocrystal assemblies over self-assembled genetically engineered P22 coat proteins. Hereafter, we refer to these hybrid structures as sulfide (ZnS or CdS) nanostructures. The assembly process and the resultant structure of protein templates are similar to those of the wild P22 procapsid. Typically, 420 copies of the P22 coat protein of MW around 47 kDa assemble with the aid of approximately 300 copies of the 33.6 kDa scaffolding protein to form an icosahedral  $T = 7$  P22 procapsid (Figure 3.8a).<sup>54-57</sup> The protein assembly (Figure 3.8b) has been established to have an approximate diameter of 58 nm. The structure of the protein assembly can be viewed as consisting of 60 hexamers clustered along with 12 pentamers at the vertices; one of each kind is marked by Numbers 5 and 6, respectively, in Figure 3.8a. Each pentamer is roughly 12.5 nm in diameter, while the axes of the slightly skewed hexamer are approximately 11 and 13 nm. Both the pentamers and hexamers contain channels of about 3 nm in diameter.<sup>54</sup> In the self-assembly of the genetically engineered P22 coat protein, as shown in Figure 3.8c, a foreign peptide is inserted between coat protein residues 182 and 183 by PCR based mutagenesis (see details of

genetic engineering of P22 coat protein in 3.3.1.2). These residues lie in the middle of a flexible loop region on the protein surface such that it has the tolerance for addition of a short peptide.<sup>55</sup> Peptide sequences with strong affinity for the sulfides, ZnS (CNNPMHQNC) and CdS (SLTPLTTSHLRS), have previously been identified from a phage display peptide library by Belcher's group.<sup>26</sup> On the resultant protein assembly, the engineered peptides ring the central channel of each of the pentamers and hexamers as dictated by the geometrical location of the original coat protein residue 182. In a typical inorganic synthesis, the protein-directed nucleation of sulfide nanocrystals occurs at the engineered regions on the protein surface. Since the central cavity of a pentamer or hexamer is about 3 nm in diameter, it can aid in the growth of a nanocrystal from several sulfide nuclei formed over five (pentamer) or six (hexamer) fused peptides.<sup>59-61</sup> Thus, an engineered protein assembly is theoretically capable of forming 72 sulfide nanocrystals symmetrically distributed on its surface. By changing the reaction time and reactant concentration, the final protein-directed sulfide growth is expected to exhibit different structures, such as ordered spherical nanocrystal assemblies (Figure 3.8d) during the early stage of growth that eventually develop into spherical hollow nanostructures for longer growth periods (Figure 3.8e). Experimental details are provided in 3.3.1.3 and the products have been investigated using transmission electron microscope (TEM) coupled with high resolution (HR).

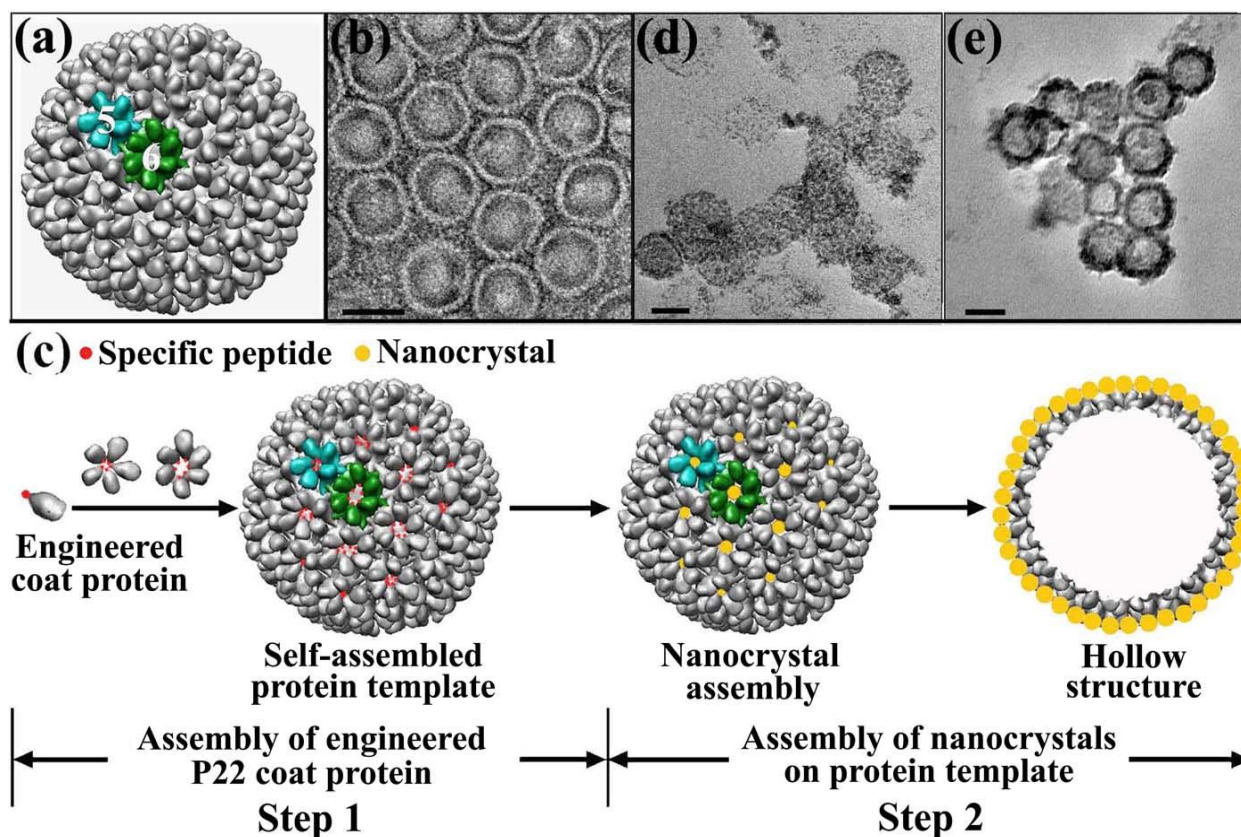


**Figure 3.8** (a) Three-dimensional surface representation of P22 procapsid viewed along a 3-fold axis; (b) TEM image of stained protein assemblies of genetically engineered P22 coat protein; (c) Schematic illustration of the formation of ordered nanocrystal assemblies over self-assembled genetically engineered P22 coat proteins. Step 1: assembly of P22 coat proteins (gray) genetically engineered with specific peptide (red). Step 2: protein-directed nucleation and growth of nanocrystals (yellow) on the protein assembly. (d, e) Sulfide nanocrystal assemblies grown on the self-assembled protein templates shown in Figure 3.8b. All scale bars represent 50 nm.

In order to verify the directing function of the protein template in the nucleation and growth of ZnS, we determined the actual number of nanocrystals formed after a short reaction period on the protein template. Figure 3.9a shows the TEM image of two ZnS nanostructures and their nanocrystal subunits. Since the individual ZnS nanocrystals are discontinuously distributed over the protein assemblies and each of them can scatter the electron beam to provide contrast, the number of nanocrystals can be counted. The number of distinct nanocrystals in each nanostructure (Figure 3.9a) has been determined to be 65 for the one on bottom-left (Figure 3.9b)

and 70 for the top-right nanostructure (Figure 3.9c), respectively. The number of nanocrystals is very close to the predicted value of 72 - the total number of pentamers and hexamers within one protein assembly. Figure 3.10a shows the TEM image of a spherical ZnS nanostructure grown on genetically engineered P22 coat protein assembly. The HRTEM image of a typical individual nanocrystal is provided in Figure 3.10b, which shows lattice fringes with a spacing of  $d = 0.337 \pm 0.006$  nm, corresponding to the (100) planes of the wurtzite (hexagonal) structure of ZnS. For site-specific nucleation and growth of the nanocrystals the pattern of electron dense ZnS nanocrystals should correspond to the locations of the fusion peptides on the protein assembly. The particles can affix to the grid with any rotation about the Euler angles and different orientations will result in different projected patterns of the ZnS nanostructure. We have verified the ability of genetically engineered proteins to direct the construction of inorganic nanostructures by matching the locations of the synthesized ZnS nanocrystals to the location of the fusion peptides on the protein assembly. Figure 3.10c displays the two dimensional projection image of the locations of the fusion peptide (small white dots) projected from the orientation providing the best match to one observed ZnS nanostructure. The seventy-two red dots indicate the center of the pentamers and hexamers, the expected locations for nanocrystal growth. The correspondence between the projected dot-pattern and the ZnS nanocrystals for one nanostructure is shown in Figure 3.10d. There are partial mismatches, which is likely due to the deformation of protein template during sample preparation and TEM imaging. The correspondence between fusion peptide and nanocrystal location for a second ZnS nanostructure affixed to the grid in a different orientation is shown in Figure 3.11a and b.

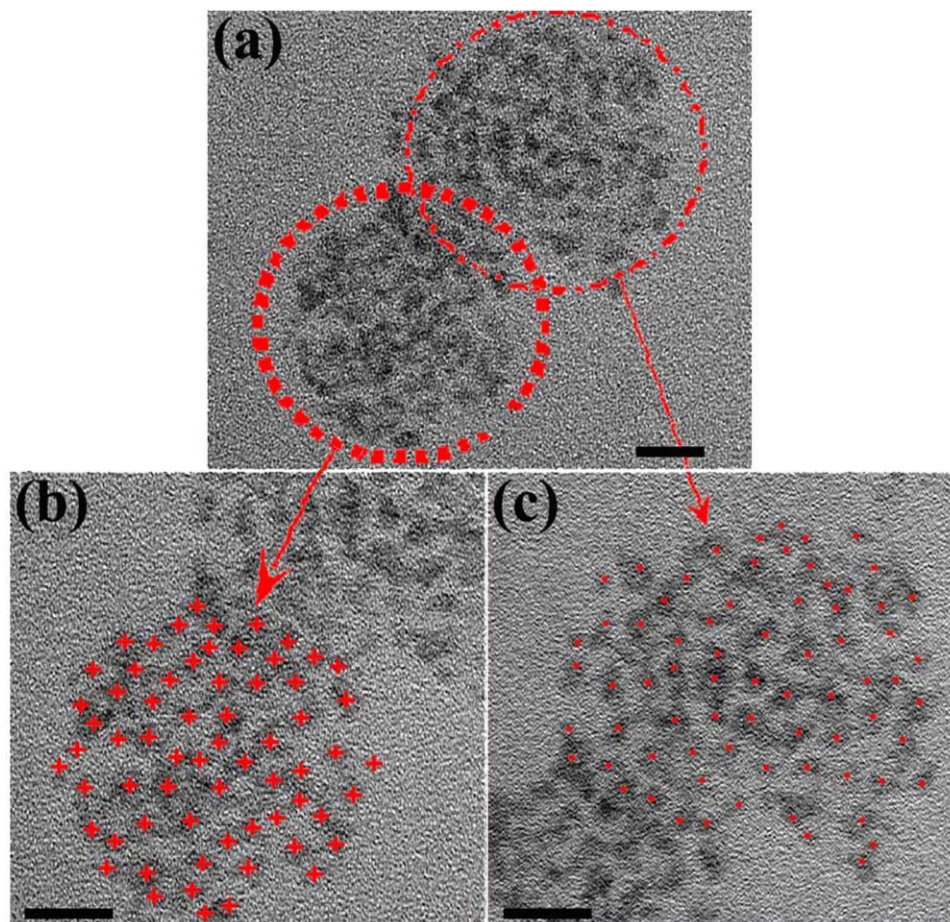


**Figure 3.9** (a) TEM image of two connected ZnS nanostructures formed after 2 h; magnified TEM images of (b) the bottom-left and (c) the top-right nanostructures shown in Figure 3.9a. Protein-templated nanocrystal subunits are marked in red. All scale bars represent 20 nm.

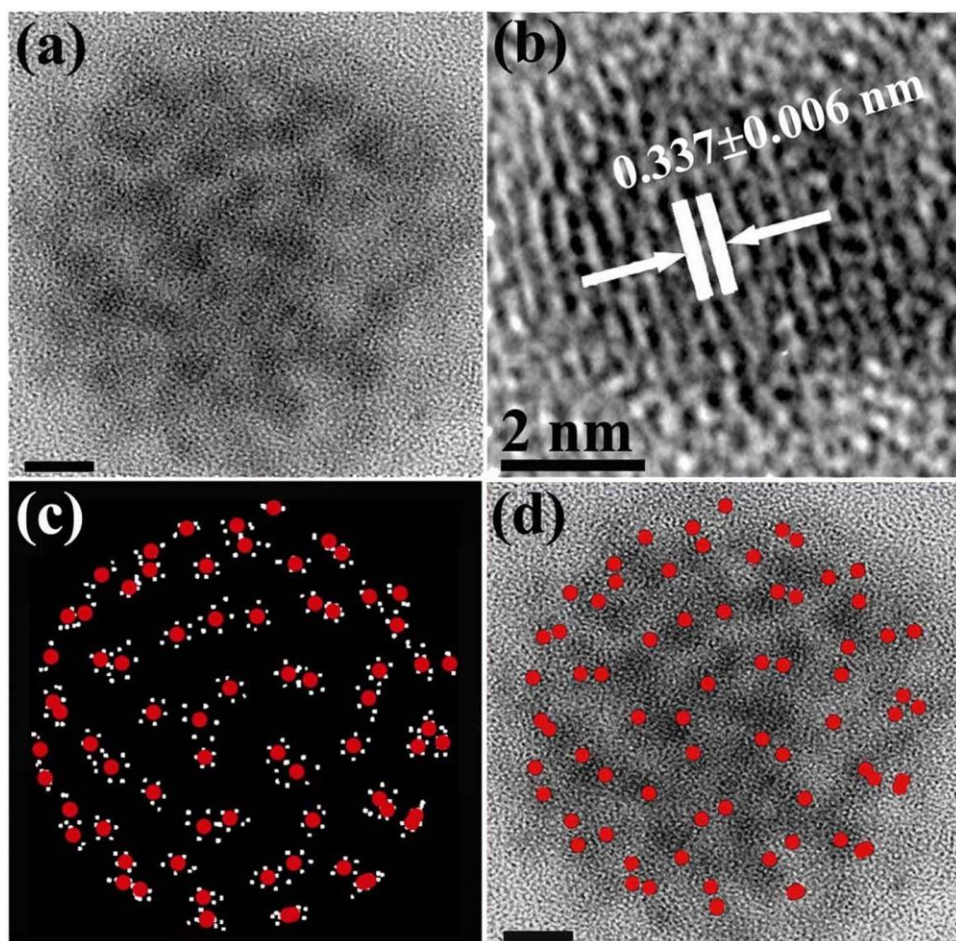


**Figure 3.10** (a) TEM image of a spherical ZnS nanostructure and (b) HRTEM image of one crystal subunit; (c) Simulated structure of P22 coat protein assembly generated by PyMOL molecular visualization system, showing protein residue 182. The red dots indicate the center of the hexamers and pentamers. (d) Superimposed simulated structure of Figure 3.10c on synthesized ZnS nanostructure. The scale bar in Figure 3.10a and 3.10d represents 10 nm.

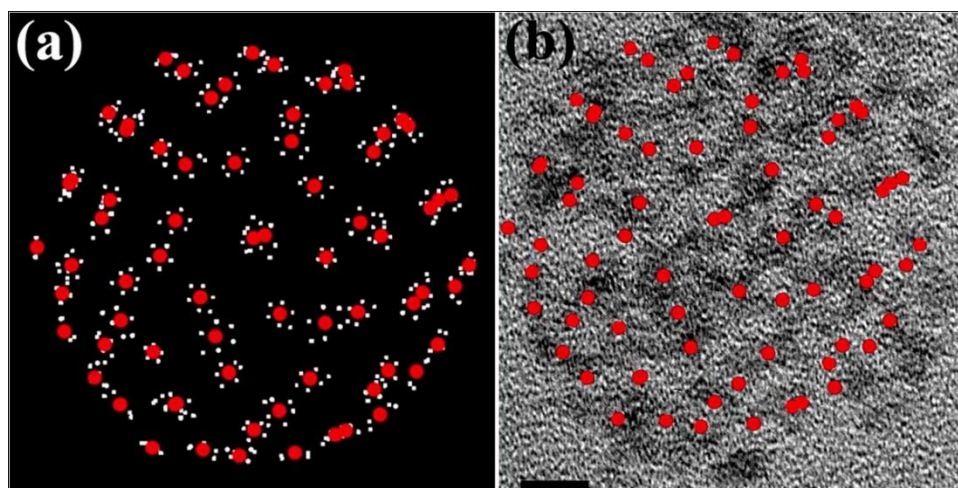


**Figure 3.11** (a) Two-dimensional projection of a simulated P22 coat protein assembly generated by PyMOL molecular visualization system, only showing the individual protein residue 182 as a white dot. The red dots indicate the center of the hexamers and pentamers. (b) Matching (a) with a ZnS nanostructure. The scale bar represents 10 nm.

We have also studied the nano-patterned assembly of CdS nanocrystals and their evolution on the surface of self-assembled genetically engineered P22 coat protein. For this purpose, as in the case of ZnS, a peptide with specific affinity to CdS is inserted into P22 coat protein. The size, shape, and structure of the synthesized ordered sulfide nanostructures can again be manipulated by varying the reaction time and reactant concentration. The nucleation and growth of CdS over the assembled proteins after a short reaction period result in the formation of the nanoclusters that are composed of  $\sim 2$  nm quantum dots, as shown in Figure 3.12. The HRTEM image (Figure 3.12d) of a typical CdS nanostructure shows clear crystal lattice fringes with interlayer spacing measured to be  $0.244 \pm 0.001$  nm, very close to the lattice spacing of the (102) planes of 0.245 nm in hexagonal CdS. We have also investigated the dot-pattern match between the synthesized CdS nanoclusters and the location of the fusion peptides on the protein assembly (Figure 3.13). The good correspondence further confirms that the sulfide nanocrystals specifically nucleate at the engineered peptide sites.

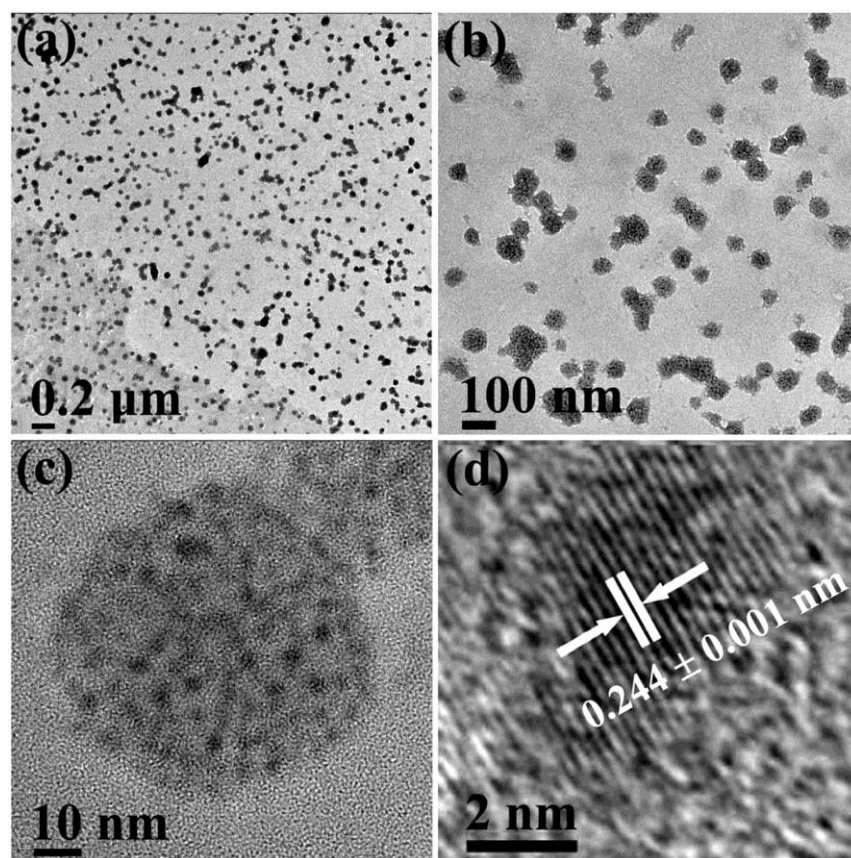


**Figure 3.12** (a-c) TEM and (d) HRTEM images of nearly monodisperse CdS nanocrystal assemblies formed over genetically engineered P22 coat protein assemblies after a short reaction time of 2 hours at a low reactant concentration (1 mM).

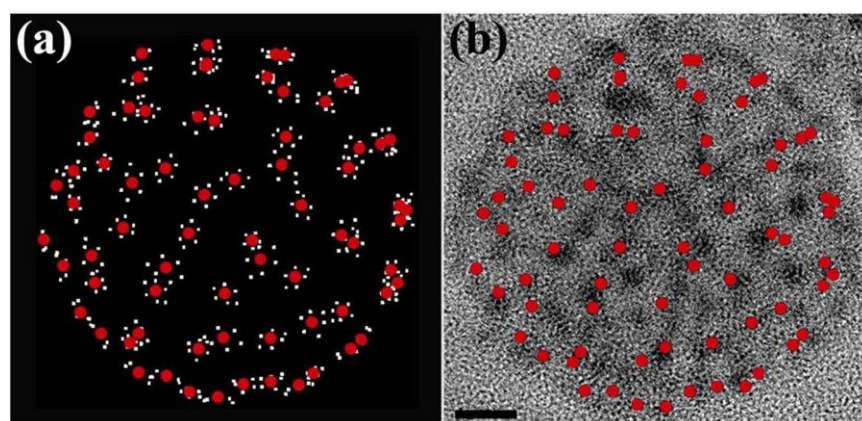


**Figure 3.13** (a) Two-dimensional projection of a simulated P22 coat protein assembly generated by PyMOL molecular visualization system, only showing the individual protein residue 182 as a white dot. The red dots indicate the center of the hexamers and pentamers. (b) Matching (a) with a CdS nanostructure. The scale bar represents 10 nm.

By prolonging the reaction time, each CdS quantum dot subunit within the initially formed nanoclusters (Figure 3.12) grows larger to form ordered assemblies of more densely-packed nanocrystals while still maintaining the nanocluster structure (Figure 3.14). With increasing both the reaction time and reactant concentration, the nanoclusters evolve into spherical hollow nanostructures (Figure 3.15), accompanying the continued growth of the CdS quantum dot subunits to ~5 nm that essentially covers a major fraction of the protein template surface. All these nanostructures can form monodisperse layers on a large scale. A similar nanostructure evolution has also been observed for ZnS nanocrystal assemblies on engineered P22 coat protein templates (Figure 3.16 and 3.17). We finally note that only the genetically engineered P22 coat protein assemblies serve as efficient templates for the protein-directed nucleation and growth of the unique sulfide nanostructures. Non-spherical nanoparticle agglomerates are obtained in the presence of wild P22 capsids (Figure 3.18a), protein assemblies engineered with non-specific peptide (Figure 3.18b), and in the absence of any protein template (Figure 3.18c).

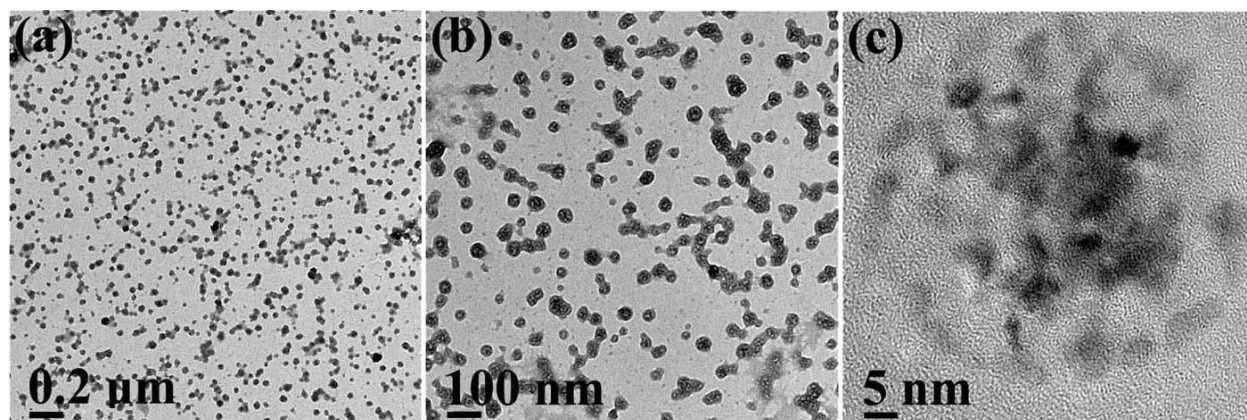


**Figure 3.14** TEM images of nearly monodisperse CdS nanocrystal assemblies formed over genetically engineered P22 coat protein assemblies after a longer reaction time of 5 hours at the low reactant concentration.

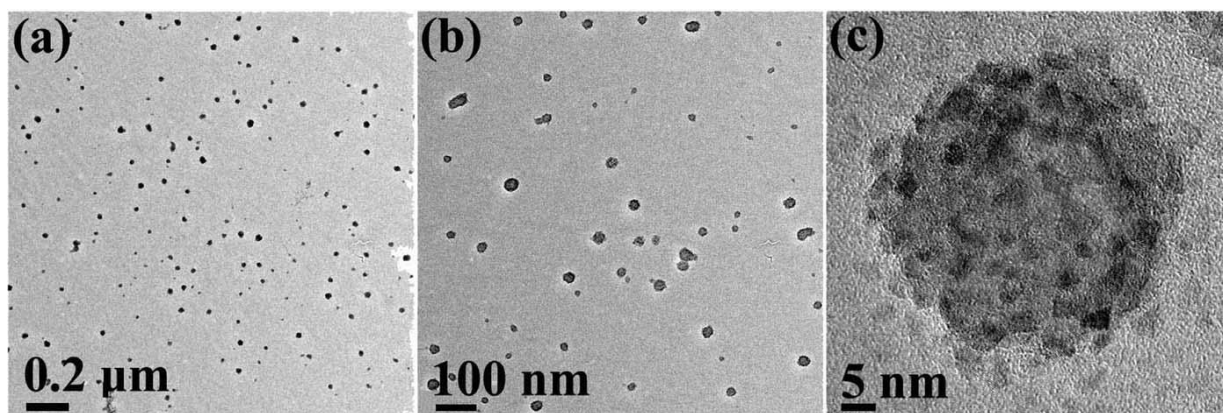


**Figure 3.15** TEM images of nearly monodisperse spherical hollow nanostructures of CdS nanocrystals assembled over genetically engineered P22 coat protein assemblies after an even longer reaction time of 12 hours and at a higher reactant concentration (2 mM).

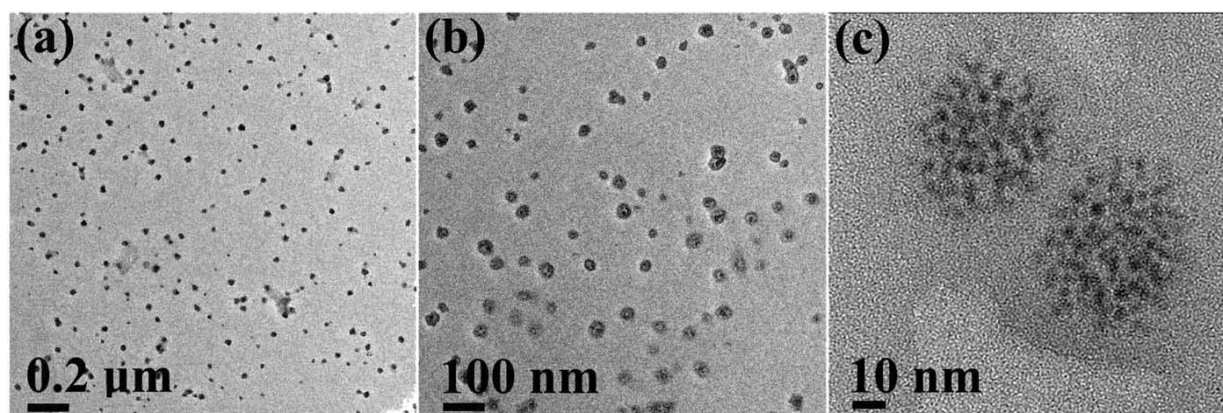


**Figure 3.16** TEM images of nearly monodisperse ZnS nanocrystal assemblies formed over genetically engineered P22 coat protein assemblies after a short reaction time of 2 hours.

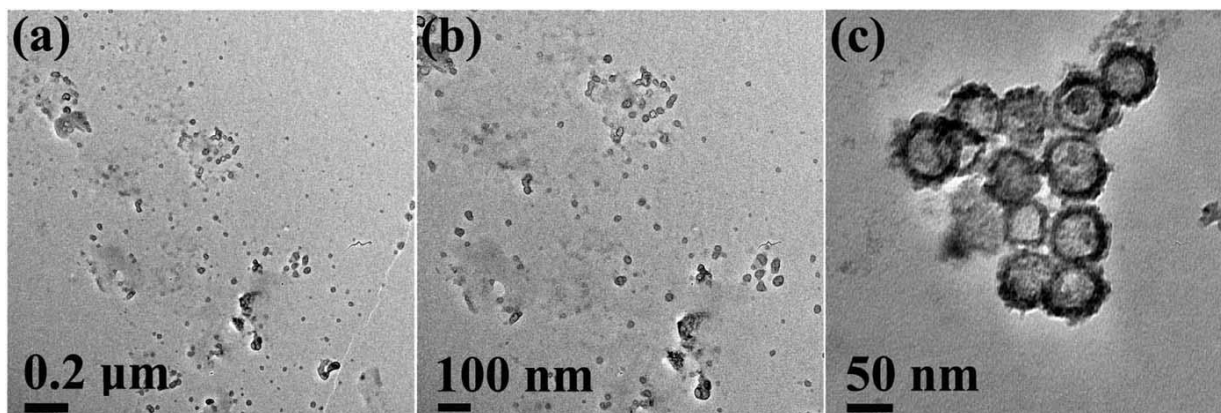


**Figure 3.17** TEM images of nearly monodisperse spherical hollow nanostructures of ZnS nanocrystals assembled over genetically engineered P22 coat protein assemblies after a longer reaction time of 12 hours.

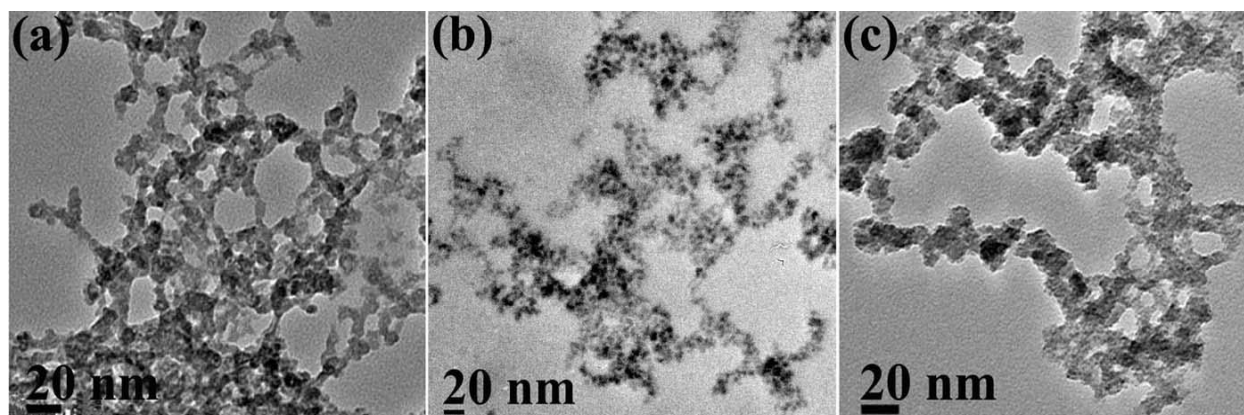


**Figure 3.18** TEM image of (a) ZnS product prepared in the presence of wild P22 procapsids; (b) CdS product prepared in the presence of self-assembled P22 coat proteins engineered with ZnS-specific peptide; and (c) ZnS product prepared in the absence of any type of P22 coat protein.

### 3.3.3 Conclusion

In summary, we have demonstrated a controllable approach for the construction of ordered ZnS and CdS nanostructures over genetically engineered P22 coat protein assemblies. The high-affinity ZnS- and CdS-binding peptides, identified from phage display library, enable the selective nucleation and growth of sulfides over the complex protein assemblies. The

demonstrated strategy can be expanded to serve as a general bio-inspired approach for the design of nanoparticle assemblies with desired components and architectures.

### 3.4 References

1. Zhou, S.; McIlwrath, K.; Jackson, G.; Eichhorn, B. *J. Am. Chem. Soc.* **2006**, *128*, 1780-1781.
2. Cheng, K.; Peng, S.; Xu, C.; Sun S. *J. Am. Chem. Soc.* **2009**, *131*, 10637-10644.
3. Xu, C.; Wang, B.; Sun, S. *J. Am. Chem. Soc.* **2009**, *131*, 4216-4217.
4. Choi, S.-H.; Na, H. B.; Park, Y.; An, K.; Kwon, S. G.; Jang, Y.; Park, M.; Moon, J.; Son, J. S.; Song, I. C.; Moon, W. K.; Hyeon, T. *J. Am. Chem. Soc.* **2008**, *130*, 15573-15580.
5. Ge, J.; Hu, Y.; Yin, Y. *Angew. Chem. Int. Ed.* **2007**, *46*, 7428-7431.
6. Nie, Z.; Petukhova, A.; Kumacheva, E. *Nat. Nanotechnol.* **2010**, *5*, 15-25.
7. Glotzer, S. C.; Solomon, M. J. *Nat. Mater.* **2007**, *6*, 557-562.
8. Sarikaya, M.; Tamerler, C.; Jen, A. -Y.; Schulten, K.; Baneyx, F. *Nat. Mater.* **2003**, *2*, 577-585.
9. Sanchez, C.; Arribart, H.; Guille, M. M. G. *Nat. Mater.* **2005**, *4*, 277-288.
10. Douglas, T.; Young, M. *Science* **2006**, *312*, 873-875.
11. Palmer, L. C.; Stupp, S. I. *Acc. Chem. Res.* **2008**, *41*, 1674-1684.
12. Cheung, C. L.; Chung, S.; Chatterji, A.; Lin, T.; Johnson, J. E.; Hok, S.; Perkins, J.; De Yoreo, J. J. *J. Am. Chem. Soc.* **2006**, *128*, 10801-10807.
13. Crookes-Goodson, W. J.; Slocik, J. M.; Naik, R. R. *Chem. Soc. Rev.* **2008**, *37*, 2403-2412.
14. Kroger, N.; Deutzmann, R.; Sumper, M. *Science* **1999**, *286*, 1129-1132.
15. Zhang, S. *Nat. Biotechnol.* **2003**, *21*, 1171-1178.
16. Chen, C.; Rosi, N. L. *Angew. Chem. Int. Ed.* **2010**, *49*, 1924-1942.
17. Varpness, Z.; Peters, J. W.; Young, M.; Douglas, T. *Nano Lett.* **2005**, *5*, 2306-2309.

18. Ueno, T.; Suzuki, M.; Goto, T.; Matsumoto, T.; Nagayama, K.; Watanabe, Y. *Angew. Chem. Int. Ed.* **2004**, *43*, 2527-2530.
19. Ensign, D.; Young, M.; Douglas, T. *Inorg. Chem.* **2004**, *43*, 3441-3446.
20. Kramer, R. M.; Li, C.; Carter, D. C.; Stone, M. O.; Naik, R. R. *J. Am. Chem. Soc.* **2004**, *126*, 13282-13286.
21. Iwahori, K.; Enomoto, T.; Furusho, H.; Miura, A.; Nishio, K.; Mishima, Y.; Yamashita, I. *Chem. Mater.* **2007**, *19*, 3105-3111.
22. Klem, M. T.; Resnick, D. A.; Gilmore, K.; Young, M.; Idzerda, Y. U.; and Douglas, T. *J. Am. Chem. Soc.* **2007**, *129*, 197-201.
23. Klem, M. T.; Willits, D.; Young, M.; Douglas, T. *J. Am. Chem. Soc.* **2003**, *125*, 10806-10807.
24. Flenniken, M. L.; Liepold L. O.; Crowley, B. E.; Willits, D. A.; Young, M. J.; Douglas, T. *Chem. Commun.* **2005**, 447-449.
25. Uchida, M.; Flenniken, M. L.; Allen, M.; Willits, D. A.; Crowley, B. E.; Brumfield, S.; Willis, A. F.; Jackiw, L.; Jutila, M.; Young, M. J.; Douglas, T. *J. Am. Chem. Soc.* **2006**, *128*, 16626-16633.
26. Flynn C. E.; Mao C.; Hayhurst A.; Williams J. L.; Georgiou G.; Iverson B.; Belcher, A. M. *J. Mater. Chem.* **2003**, *13*, 2414-2421.
27. Whaley, S. R.; English, D. S.; Hu, E. L.; Barbara, P. F.; Belcher, A. M. *Nature* **2000**, *405*, 665-668.
28. Mao, C.; Solis, D. J.; Reiss, B. D.; Kottmann, S. T.; Sweeney, R. Y.; Hayhurst, A.; Georgiou, G.; Iverson, B.; Belcher, A. M. *Science* **2004**, *303*, 213-217.
29. Li, Y.; Whyburn, G. P.; Huang, Y. *J. Am. Chem. Soc.* **2009**, *131*, 15998-15999.
30. Khoo, X.; Hamilton, P.; O'Toole, G. A.; Snyder, B. D.; Kenan, D. J.; Grinstaff, M. W. *J. Am. Chem. Soc.* **2009**, *131*, 10992-10997.
31. Heinz, H.; Farmer, B. L.; Pandey, R. B.; Slocik, J. M.; Patnaik, S. S.; Pachter, R.; Naik, R. R. *J. Am. Chem. Soc.* **2009**, *131*, 9704-9714.
32. Sano, K.; Shiba, K. *J. Am. Chem. Soc.* **2003**, *125*, 14234-14235.
33. Zhou, W.; Schwartz, D. T.; Baneyx, F. *J. Am. Chem. Soc.* **2010**, *132*, 4731-4738.
34. Roach, P.; Farrar, D.; Perry, C. C. *J. Am. Chem. Soc.* **2005**, *127*, 8168-8173.

35. Zorbas, V.; Smith, A.; Xie, H.; Ortiz-Acevedo, A.; Dalton, A. B.; Dieckmann, G. R.; Draper, R. K.; Baughman, R. H.; Musselman, I. H. *J. Am. Chem. Soc.* **2005**, *127*, 12323-12328.
36. Banerjee, I. A.; Yu, L.; Matsui, H. *J. Am. Chem. Soc.* **2005**, *127*, 16002-16003.
37. Chen, C. L.; Rosi, N. L. *J. Am. Chem. Soc.* **2010**, *132*, 6902-6903.
38. Chen, C. L.; Zhang, P. J.; Rosi, N. L. *J. Am. Chem. Soc.* **2008**, *130*, 13555-13557.
39. Chen, C. L.; Rosi, N. L. *Angew. Chem., Int. Ed.* **2010**, *49*, 1924-1942.
40. Stephanopoulos, N.; Liu, M.; Tong, G. Y.; Li, Z.; Liu, Y.; Yan, H.; Francis, M. B. *Nano Lett.* **2010**, *10*, 2714-2720.
41. Smith, G. P.; Petrenko, V. A. *Chem. Rev.* **1997**, *97*, 391-410.
42. Hoess, R. H. *Chem. Rev.* **2001**, *101*, 3205-3218.
43. <http://www.neb.com/nebecomm/products/productE8110.asp>
44. Naik, R. R.; Stringer, S. J.; Agarwal, G.; Jones, S. E.; Stone, M. O. *Nat. Mater.* **2002**, *1*, 169-172.
45. Dickerson, M. B.; Naik, R. R.; Stones, M. O.; Cai, Y.; Sandhage, K. H. *Chem. Commun.* **2004**, 1776-1777.
46. Ahmad, G.; Dickerson, M. B.; Cai, Y.; Jones, S. E.; Ernst, E. M.; Vernon, J. P.; Haluska, M. S.; Fang, Y.; Wang, J.; Subramanyam, G.; Naik, R. R.; Sandhage, K. H. *J. Am. Chem. Soc.* **2008**, *130*, 4-5.
47. Slocik, J. M.; Stone, M. O.; Naik, R. R. *Small* **2005**, *1*, 1048-1052.
48. Lad, R. J.; Antonik, M. D. *Ceram. Trans.* **1991**, *24*, 359-366.
49. Diebold, U. *Surf. Sci. Rep.* **2003**, *48*, 53-229.
50. Feher, M. *Chem. Phys. Lett.* **1992**, *188*, 609-612.
51. Ding, Y.-H.; Huang, X.-R.; Li, Z.-S.; Liu, J.-Y. *J. Mol. Struct. (Theochem)* **1998**, *454*, 61-67.
52. Diebold, U. *Surface Science Reports* **2003**, *48*, 53-229.
53. Lee, S.; Mao, C.; Flynn, C. E.; Belcher, A. M. *Science* **2002**, *296*, 892-895.
54. Thuman-Commike, P. A.; Greene, B.; Jakana, J.; Prasad, B. B. V.; King, J.; Prevelige, P. E.; Chiu, W. *J. Mol. Biol.* **1996**, *260*, 85-98.

55. Kang, S.; Lander, G. C.; Johnson, J. E.; Prevelige, P. E. *Chembiochem.* **2008**, *9*, 514-518.
56. Lander, G. C.; Tang, L.; Casjens, S. R.; Gilcrease, E. B.; Prevelige, P. E.; Poliakov, A.; Potter, C. S.; Carragher, B.; Johnson, J. E. *Science* **2006**, *312*, 1791-1795.
57. <http://www.sb.uconn.edu/MOTM.html>.
58. Teschke, C. M.; McGough, A.; Thuman-Commike, P. A. *Biophys. J.* **2003**, *84*, 2585-2592.
59. Zheng, H.; Smith, R. K.; Jun, Y.; Kisielowski, C.; Dahmen, U.; Alivisatos, A. P. *Science* **2009**, *324*, 1309-1312.
60. Privman, V.; Goia, D. V.; Park, J.; Matijevic, E. J. *Colloid Interface Sci.* **1999**, *213*, 36-45.
61. Bao, N.; Shen, L.; Wang, Y.-H. A.; Ma, J.; Mazumdar, D.; Gupta, A. *J. Am. Chem. Soc.* **2009**, *131*, 12900-12901.

## CHAPTER 4

### BACTERIUM E. COLI-TEMPLATED SYNTHESIS OF NANOPOROUS CADMIUM SULFIDE HOLLOW MICRORODS FOR EFFICIENT PHOTOCATALYTIC HYDROGEN PRODUCTION

Reproduced in part with permission from [Shen, L.; Bao, N.; Prevelige, P. E.; Gupta, A. *J. Phys. Chem. C* **2010**, *114*, 2551–2559.]. Copyright [2010] American Chemical Society.

#### 4.1 Introduction

Sulfides, such as CdS,<sup>1</sup> AgInS<sub>2</sub>,<sup>2</sup> CuInS<sub>2</sub>,<sup>3, 4</sup> etc., are a group of narrow-band-gap semiconductors that have been widely researched as candidates for visible-light-driven photocatalysis. In the presence of a sacrificial reagent, CdS, with a bandgap of about 2.4 eV and a flat-band potential at -0.66 V (pH 7), is an excellent photocatalyst for H<sub>2</sub> production under visible light irradiation.<sup>5, 6</sup> It should be noted that the bandgap structure of materials is only a thermodynamic requirement and not a sufficient condition for an efficient photocatalysis. The solar energy conversion efficiency of a photocatalyst is strongly dependent on materials-related characteristics, including the crystal structure, crystallinity, particle size, and distinctive nanostructures.<sup>7</sup> These factors directly influence the bandgap structure and electron-transfer processes, including the charge separation, transport of photogenerated carriers, and photochemical reactivity at the photocatalyst/electrolyte interface. Cadmium sulfide (CdS) nanocrystals with a hexagonal crystal structure have shown superior photocatalytic activity than that with a pure cubic, or a mixture of cubic and hexagonal phases.<sup>6</sup> Recent studies indicate that nanoporous hollow structures provide a shorter pathway for the transfer of electrons excited in semiconductors.<sup>8, 9</sup> Accordingly, nanoporous hexagonal CdS with a hollow structure, prepared using a two-step chemical reaction, exhibits a high activity (quantum yield=60.34 %) for the photocatalytic hydrogen production under visible light irradiation ( $\lambda \geq 420$  nm).<sup>10</sup>

Hollow structures have in fact attracted attention for a variety of applications, and are commonly fabricated on pre-synthesized templates such as polystyrene,<sup>11, 12</sup> silica spheres,<sup>13, 14</sup> etc. In recent years, a wide range of microbiological organisms, including proteins,<sup>15, 16</sup> nucleic acids,<sup>17, 18</sup> phages,<sup>19</sup> bacteria,<sup>20</sup> and complex multicellular systems,<sup>21</sup> have also been investigated as biotemplates. Using such biological systems, a number of inorganic nanomaterials have been synthesized with precisely controlled size, shape, structure, and functionality.<sup>22-25</sup> These nanomaterials can be further assembled into more complex functional structures and devices.<sup>26, 27</sup> From a practical viewpoint, unicellular microorganisms, such as bacteria, are attractive templates for material synthesis since they are readily available in a wide variety of shapes and sizes, and a number of them are environmentally benign and can be readily amplified under ambient conditions.<sup>28</sup>

Bacterial systems, including *Clostridium*, *Klebsiella aerogenes*, and *Escherichia coli* (*E. coli*), have been used to biosynthesize CdS nanocrystals.<sup>29</sup> *E. coli* is of particular interest, since it is a Gram-negative bacterium and is by far the most well studied bacterial system. The genetic tools and cellular metabolisms associated with this bacterium are fairly well understood. *E. coli* is also one of the longest rod-shaped bacteria.<sup>30</sup> Using *E. coli*, intracellular hexagonal CdS nanocrystals have been produced with a size distribution of 2-5 nm when the bacteria are incubated in a solution containing cadmium chloride and sodium sulfide.<sup>31</sup> The nanocrystal yield varies dramatically depending on the growth phase of the cells; increasing nearly 20-fold in *E. coli* cells grown to the stationary phase as compared with those grown to the late logarithmic phase. More recently, the microbial synthesis of CdS nanocrystals in genetically engineered *E. coli*, produced by expressing the phytochelatin synthase of *Schizosaccharomyces pombe* (SpPCS), has been reported.<sup>32</sup> By controlling the population of the capping PCs, *E. coli* cells

have been engineered as an eco-friendly biofactory to produce uniformly sized PC-coated CdS nanocrystals. In both reported cases, the intracellularly synthesized CdS in the form of nanocrystals has to be collected by disrupting the cells. Furthermore, the concentrations of the inorganic reactant salts have to be carefully controlled in order to avoid a rapid, uncontrolled precipitation of CdS particles in solution. Thus far, the controllable intracellular synthesis and assembly of more complex CdS architectures on *E. coli* has not been feasible because the low permeability of cell envelope and the efflux pump inhibition<sup>33-34</sup> in bacterial system prevents the nucleation of inorganic materials throughout the cell envelope.

We have developed a simple sonochemical route for the synthesis and assembly of CdS nanostructure with high yield under mild ambient conditions by exploiting the chemical characteristics and structure of permeabilized *E. coli* bacteria. Although other bacteria, such as *L. bulgaricus*, have been used as templates to prepare ZnS on the cell surface by combining sonochemistry,<sup>35</sup> the novelty of the present method lies in the use and modification of *E. coli* for the templating growth of CdS with controllable material properties. *E. coli* is one of the longest rod-shaped bacteria and also one of the most extensively studied bacterial systems.<sup>30</sup> Motivated by the use of ethanol in Gram staining, we have developed an ethanol treatment method to enhance the permeability of Gram-negative *E. coli* while retaining its morphology.<sup>36</sup> The role of ethanol is to dissolve the lipid layer in cell's outer membrane, thus enabling Cd<sup>2+</sup> adsorption and reaction throughout the cell envelope. Upon the addition of thioacetamide (TA), H<sub>2</sub>S is gradually produced by the sonochemical decomposition<sup>37</sup> and then reacts rapidly with the adsorbed cadmium ions to nucleate and grow CdS throughout the cell envelope. With increasing the reaction time, the CdS nanoparticles grow larger and coalesce to form continuous hollow nanostructures. Thus, by simply changing the reaction time, CdS nanostructures in the form of

monodisperse quantum dots, nearly monodisperse nanocrystals, and nanoporous hollow microrods are controllably formed throughout the whole cell envelope of the *E. coli* using cadmium acetate and thioacetamide as reactants. The process is schematically illustrated in Figure 4.1. We have also fabricated novel structures consisting of CdS nanorod antennas attached to nanoporous hollow microrods by using *E. coli* pili as templates. As expected, the synthesized CdS nanostructures show a distinct red-shift with increasing size of the nanostructures. In addition to controlling the morphology, we can precisely tune the crystal phase of CdS products from cubic, a mixture of cubic and hexagonal, to pure hexagonal by merely adjusting the sulfur/cadmium molar ratio of the reactants. Photoanodes fabricated using the nanoporous hollow CdS microrods of hexagonal structure exhibit excellent performance for the photocatalytic hydrogen production, with a maximum photoelectrochemical cell efficiency of 4.33 % under global AM 1.5 illumination. We have extended this bacterium-templated approach to the synthesis and assembly of other sulfides, including PbS, ZnS, and HgS.

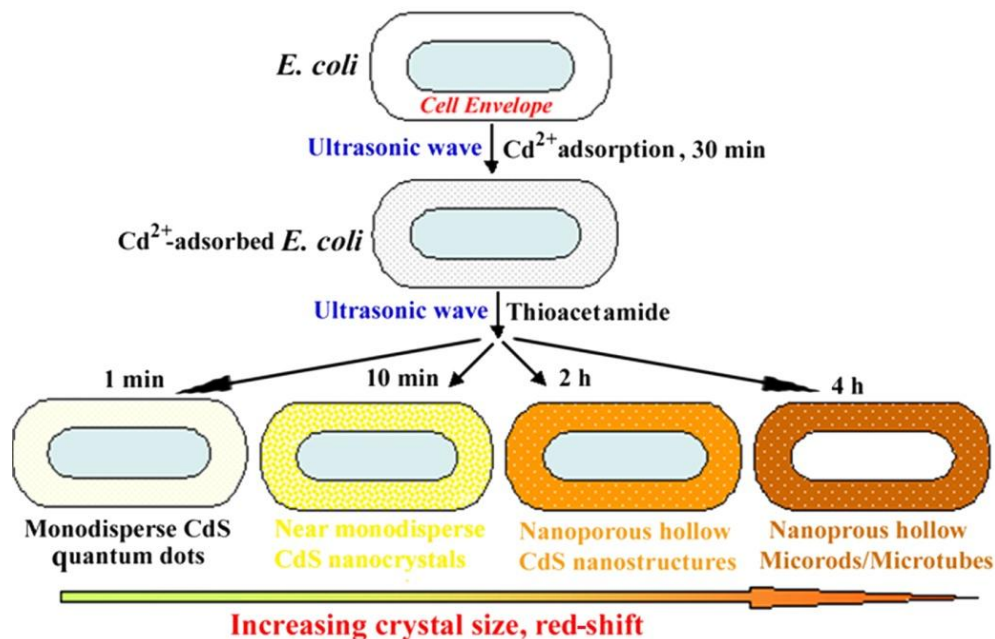


**Figure 4.1** A schematic diagram illustrating the concept of *E. coli*-templated synthesis and assembly of nanoporous hollow CdS nanostructures.

## 4.2 Experimental

### 4.2.1 Preparation of Cells

*E. coli* strain ER2738 was supplied by New England Biolab. The ER2738 cells were incubated in LB medium overnight, centrifuged at 10,000 rpm for 10 min, and then re-suspended in 1/7 volume sterile deionized water (the concentration of cells was  $\sim 10^9$  CFU/mL). 1 mL of this cell culture was centrifuged and the cell pellet was completely dispersed in 95 % ethanol for 3 min, followed by the addition of 50 mL of sterile deionized water. The ethanol-treated ER2738 cells were collected by centrifugation and then re-suspended in 50 mL of sterile deionized water for the inorganic synthesis.

### 4.2.2 Synthesis of CdS Nanostructures

Cadmium acetate dihydrate and thioacetamide were purchased from Acros Organics and used as-received. In a typical procedure, 0.5 mmol of cadmium acetate dihydrate was first added to 50 mL of ethanol-treated ER2738 solution and after 30 min, 0.5 mmol of thioacetamide was subsequently added. The reactions were conducted for up to 4 h in an ultrasonic bath with the temperature maintained at around 28 °C. The time-dependence of the size, shape, and structure of the *E. coli*-templated CdS structures was investigated by changing the reaction time. By adjusting the sulfur/cadmium molar ratio, the crystal phase of the CdS product could be precisely controlled from cubic, mixture of cubic and hexagonal, to pure hexagonal. For example, in order to supply more sulfide ions in a short time for decreasing the Cd/S ratio, the thioacetamide concentration was increased so that a suitable amount of hydrogen sulfide could be produced rapidly. The synthetic procedure has been extended to the synthesis of other sulfides such as PbS, HgS, and ZnS.

### 4.2.3 Characterization of materials

The morphology and structure of the CdS products were investigated using a combination of scanning electron microscopy (SEM, Philips X-30), operating at 20 kV, and transmission electron microscopy (TEM, coupled with high resolution (HR), Tecnai F-20), operating at 200 kV. The composition analysis was carried out using energy dispersive X-ray spectroscopy (EDS), equipped on the SEM. X-ray diffraction (XRD) patterns of samples were obtained on a Bruker D8 Advance X-ray diffractometer (Co irradiation,  $\lambda=1.7889 \text{ \AA}$ ), in the continuous scan mode over  $20\text{-}70^\circ$  ( $2\theta$ ) with a scanning rate of  $0.02^\circ$  ( $2\theta$ )/second, operating at 45 kV and 20 mA. UV-visible (UV-Vis) absorption spectrum of all the samples dispersed in water was recorded using a Varian Cary UV-Vis spectrophotometer.

### 4.2.4 Photoelectrochemical characterization

The photoanode was fabricated by spin-coating several layers of *E. coli*-templated CdS ethanol solution (0.05 g/ml) on to an ITO-coated glass substrate (1 cm  $\times$  1 cm) and was then annealed at  $300^\circ\text{C}$  in high-purity  $\text{N}_2$  for 0.5 h. The *E. coli*-templated CdS used for the fabrication of electrode was synthesized by the procedure described above. For comparison, a photoanode consisting of an identical amount of CdS nanoparticles synthesized in the absence of *E. coli* template was fabricated using the same procedure. An EG&G potentiostat was used to measure the photoelectrochemical response of the fabricated photoanodes with a conventional three-electrode system comprising of an Ag/AgCl reference electrode and Pt foil counter electrode. A 1 M  $\text{Na}_2\text{S}$ -0.5 M  $\text{Na}_2\text{SO}_3$  aqueous solution was used as the electrolyte. A solar simulator with an illumination intensity of one sun (AM 1.5,  $100 \text{ mW/cm}^2$ , Newport Corporation) was used as the light source. A power meter (Scientech, Inc.) was used to calibrate the input power before and

after the photoelectrochemical measurements. The photoelectrochemical cell efficiency was used as the parameter to evaluate the photoelectrochemical property of the synthesized nanostructures.<sup>38-39</sup>

### 4.3 Results and Discussion

The composition, crystal phase, morphology, structure, and optical absorption properties of the products have been examined using EDS, XRD, SEM, (HR) TEM, and UV-Vis spectroscopy. Figure 4.2 shows the typical morphology and structure of as-synthesized *E. coli*-templated nanoporous hollow CdS microrods obtained after a reaction time of 4 h. Figures 4.2a and 4.2b show the large-area and magnified SEM images of the products, respectively. The shape and dimension of most of the product are very close to that of *E. coli* (being rod-like with  $\sim 2.5 \mu\text{m}$  in length and  $\sim 0.8 \mu\text{m}$  in diameter), which indicates that the bacterium indeed acts as a template for the synthesis. A small fraction of the product has a longer length and some exhibit open-ended structures, as seen in Figures 4.2b and 4.2d. The latter is caused by cell division, which is a natural process during the cell growth. The CdS microrod imaged on the right in Figure 4.2c is formed at the start of cell division as suggested by the narrowed diameter in the mid section that appears pinched; while the microrod imaged in the left has a uniform diameter over the entire length since it forms before the cell division. The TEM cross section image for products formed at the time of cell division have an open end, as observed in Figure 4.2d. The hollow nature of the CdS microrods is quite apparent based on the examination of these open-end structures. Figure 4.2e shows the cross section TEM image of an open-end hollow microrod. The front and the back sides of the microrod can to be readily distinguished by comparing the bright/dark contrast. Since the diameter of the hollow microtubes is around  $0.8 \mu\text{m}$ , it is difficult

to image them with both the front and the back ends in focus. In Figure 4.2e, the bright part represents the back side of the microrod, which is in focus, showing the inner surface and structure. The dark part represents the front side of the microrod, showing an unfocused image of the outer surface and structure. By measuring the dark edge of the microrod in Figure 4.2e, the wall thickness is estimated to be around 60 nm. The hollow microrods are composed of CdS nanoparticle agglomerates that form a nanoporous structure with uniformly distributed nanopores of around 5 nm in diameter across the entire length. Both nanopores and clear crystal lattice fringes are observed in the HRTEM image shown in the inset to Figure 4.2f. We have further verified using EDS that the chemical composition of the products is close to stoichiometric with a Cd/S atomic ratio of  $\sim 1.02$ .

We have investigated the nucleation and growth of CdS on the ethanol-treated *E. coli* by withdrawing a small amount of sample from the reaction solution after 1 min, 10 min, 2 h, and 4 h of reaction for the TEM imaging and optical absorption measurements. Figure 4.3 shows the morphology of products formed after 1 min (Figures 4.3a and b), 10 min (Figures 4.3b and c), 2 h (Figure 4.3d), and 4 h (Figure 4.3e). As seen in Figure 4.3b, monodisperse single-crystalline CdS quantum dots with dimension  $< 2.5$  nm (over 90 % of the nanoparticles with sizes in the range of  $2.3 \pm 0.4$  nm) are formed inside the cell envelope after 1 min reaction. By prolonging the reaction time to 10 min, the quantum dots grow larger, forming CdS nanocrystals with dimension  $< 6.5$  nm (over 80 % of the nanoparticles with sizes in the range of  $5.3 \pm 0.5$  nm), as seen in Figure 4.3d. With further increasing the reaction time to 2 h, continuous CdS nanoparticle agglomerates form inside the cell envelope (Figure 4.3e). The hollow nature of the structure is apparent in the micrograph. After the longest reaction period (4 h), both the density and thickness of the CdS nanoparticle agglomerates increase (Figure 4.3f), resulting in a uniform porous coating.

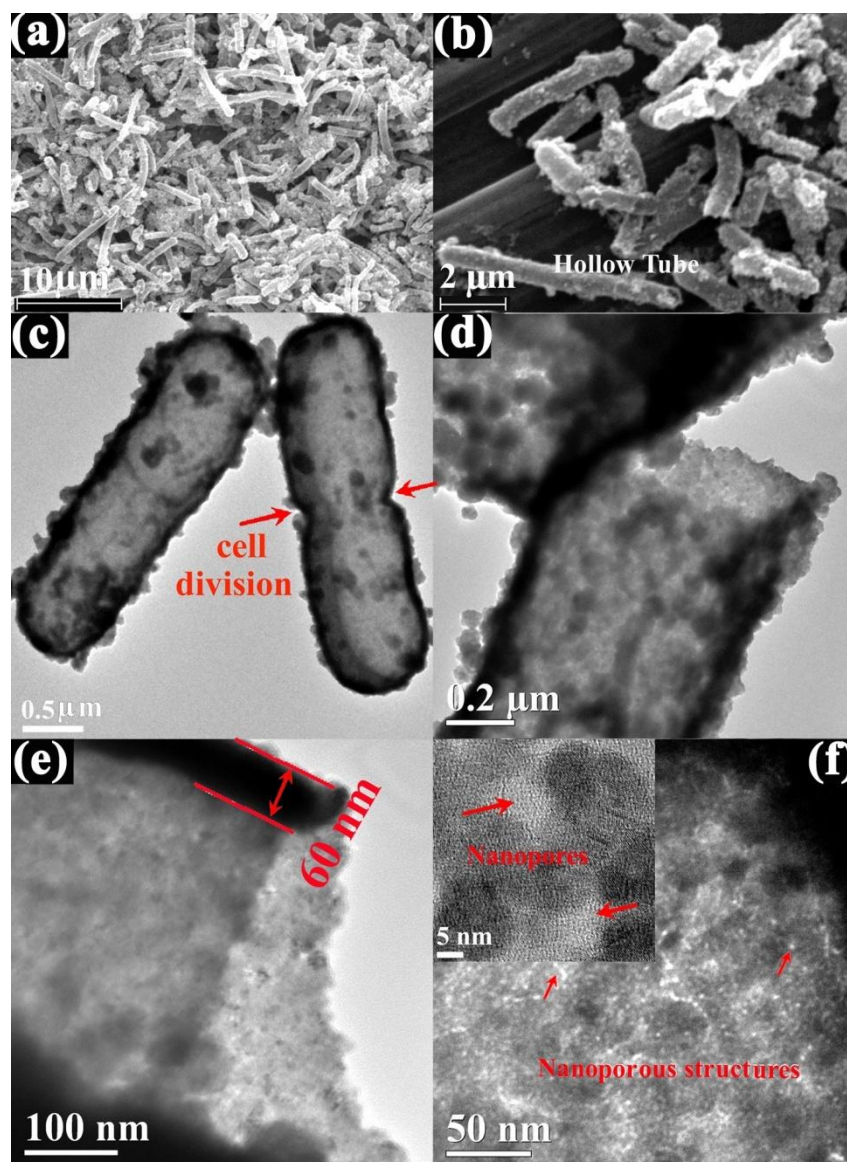


**Figure 4.2** SEM and TEM images of *E. coli*-templated nanoporous hollow CdS microrods formed after 4 h. (a) Low-magnification and (b) high-magnification SEM images of the hollow structures showing the high yield of product with the desired shape. TEM image of hollow CdS microrods with (c) closed ends and (d) an open end. The magnified TEM images of (e) the cross section and (f) the body of a rod-like hollow CdS structure show the uniform wall thickness and the nanoporous structure of the wall, respectively.

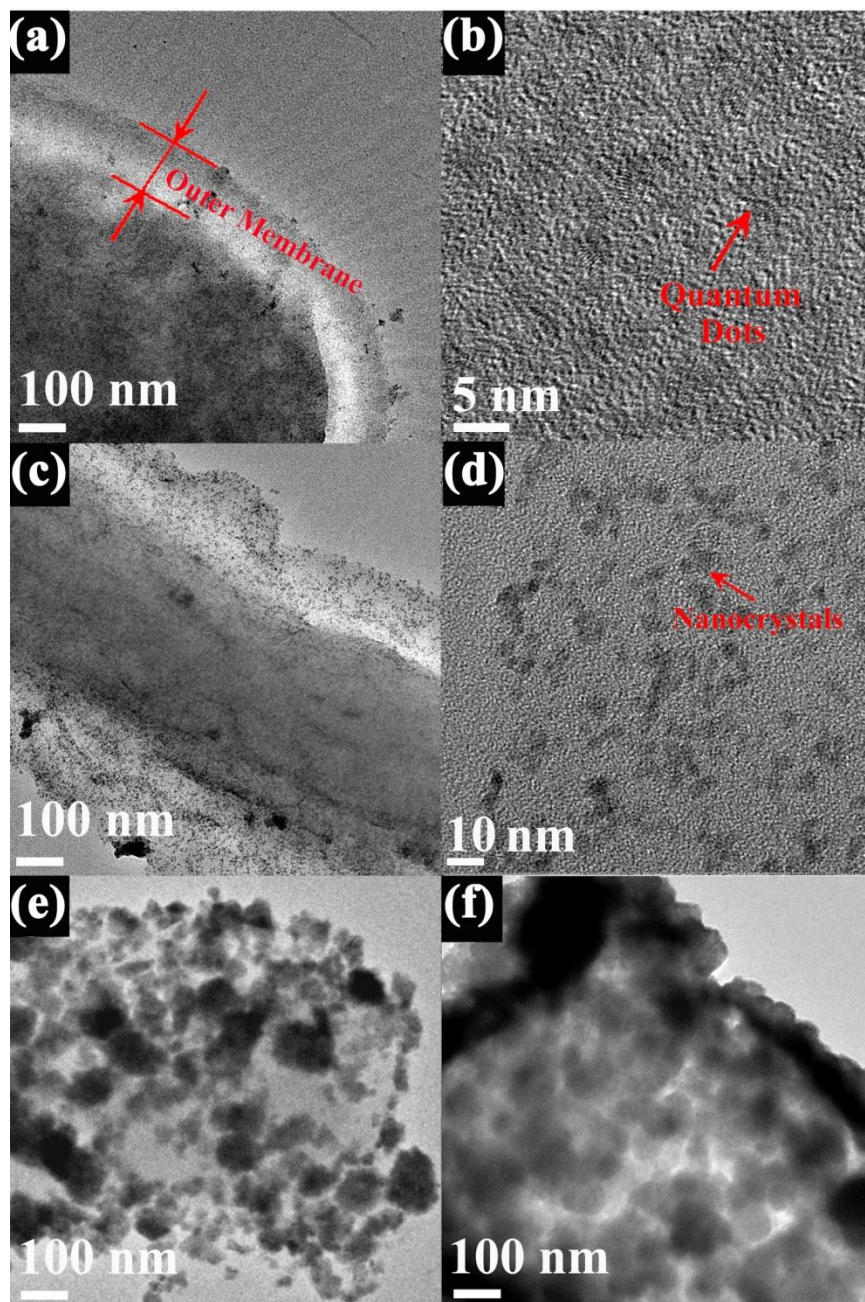


**Figure 4.3** TEM and HRTEM images of synthesized CdS nanomaterials as a function of reaction time. (a, b) Monodisperse quantum dots formed after 1 min; (c, d) nearly monodisperse nanocrystals formed after 10 min; (e) continuous nanoparticle agglomerates formed after 2 h; and (f) uniform porous coating formed after 4 h.

To confirm the essential role of *E. coli* as templates, we have verified that only CdS nanoparticles of around 80 nm in diameter are produced in their absence, under otherwise

identical reaction conditions, as seen in Figures 4.4a and b. As mentioned earlier, the ethanol treatment enhances the cell permeability of *E. coli* to enable the  $\text{Cd}^{2+}$  adsorption and reaction throughout the cell envelope. Thereby, CdS nanostructures in the form of monodisperse quantum dots, nearly monodisperse nanocrystals, and nanoporous hollow microrods are controllably formed on the cell envelope (Figure 4.3). In contrast, control experiments using untreated *E. coli* as template show the formation of CdS nanoparticles both in solution and on the surface of the bacteria after 1 min of reaction (Figure 4.4c), that then develop into large crystal agglomerates that are non-uniformly distributed on the cell surface after 2 h of reaction (Figure 4.4d).

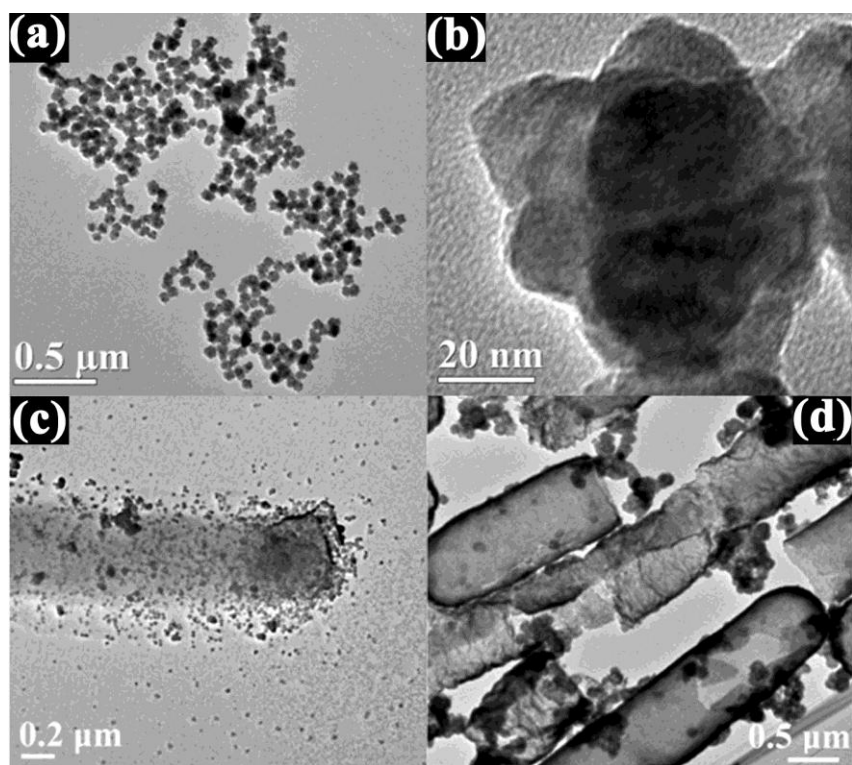


**Figure 4.4** TEM images of (a and b) crystalline CdS nanoparticles sonochemically synthesized after 4 h in the absence of *E. coli* bacteria, and CdS nanoparticles formed in the reaction solution and on the cell surface of untreated *E. coli* bacteria after (c) 1 min and (d) 2 h.

*E. coli* bacterium typically has pili (small hair-like projections emerging from the outside cell surface) during the growth phase. A cell may have 100-300 pili, which are approximately 6.5 nm in diameter and between 200 and 2000 nm in length, with a rapid loss of piliation occurring when the culture reaches the early stationary phase.<sup>40</sup> If using ethanol treated *E. coli* cells grown to the early stationary phase as templates, the resulting products are nanoporous hollow CdS microrods with attached CdS nanorod antennas, as seen in Figure 4.5. The CdS nanorod antennas have lengths varying from ~200 nm to several microns and widths of ~100 nm. By changing the growth conditions of the *E. coli*, both the number and the size of the pili will change. Correspondingly, the size, structure, and the density of the CdS nanorod antennas can be manipulated. The HRTEM image shown in Figure 4.5d indicates good crystallinity of the CdS antennas.

By increasing the reaction time, a gradual transition in the color of the reaction solution from colorless, to nearly colorless, to yellow, to orange, and finally to dark orange is observed, as shown in the photographs in Figure 4.6. Consistent with the TEM images of Figure 4.3, a distinct red-shift is noted in the absorption spectra as a function of reaction time in Figure 4.6, confirming the increase in size of the CdS nanoparticles formed on the cell envelope. The spectra of the product formed after 4 h (Figure 4.6e), with a peak at around 520 nm, is similar to that of bulk CdS. As seen in Figure 4.6e, the absorption edge for the sample obtained after 4 h reaction is at about 550 nm, which is at longer wavelength than the bandgap of bulk CdS. This is likely caused by Rayleigh scattering since the products are nanoporous hollow structures composed of nanoparticles, similar to earlier reported nanostructures.<sup>10</sup> Although the synthesized hollow microrods have a diameter of approximately 800 nm, the walls of the hollow microrod are composed of uniformly distributed CdS nanoparticle agglomerates consisting of nanoparticles in

the range of 5-15 nm in diameter and nanopores of ~5 nm. The dimension of the nanopores is extremely small as compared to the wavelength of UV and visible light (200-800 nm), resulting in the Rayleigh scattering phenomenon.

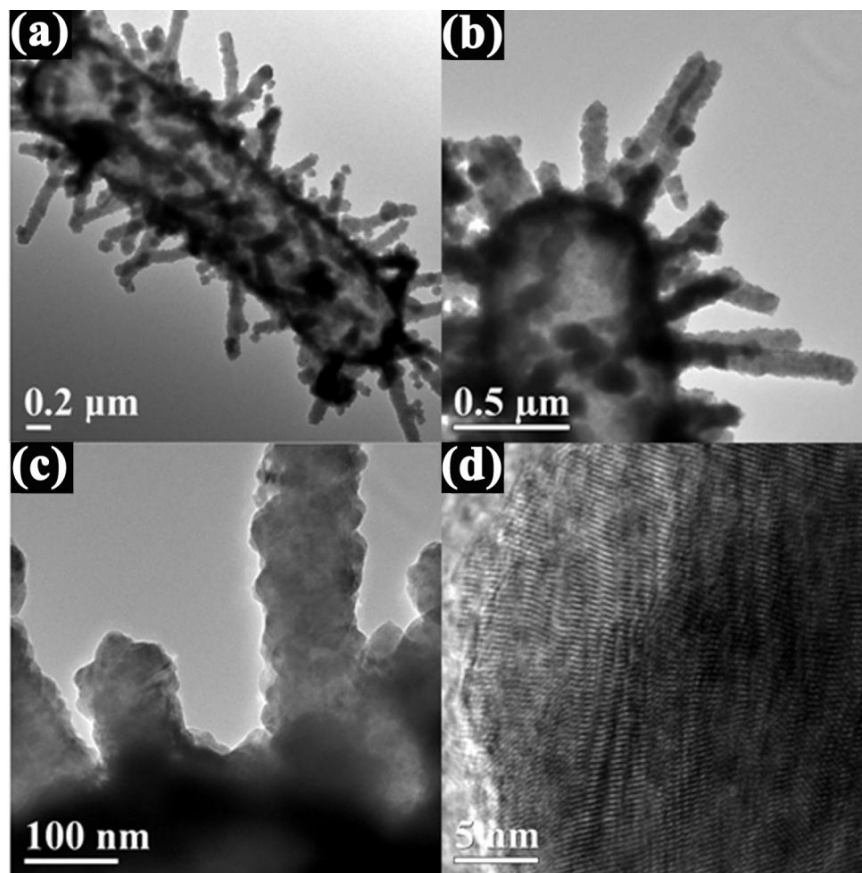


**Figure 4.5** TEM and HRTEM image of nanoporous hollow CdS microrod-supported nanorods synthesized after 4 h using *E. coli* with pili as templates. (a, b) Low-magnification and (c) high-magnification TEM images of the CdS nanostructures show the morphology and structure of the whole CdS assembly, the basic hollow microrod, and the attached nanorods. (d) HRTEM image of the CdS nanorods showing crystal lattice fringes.

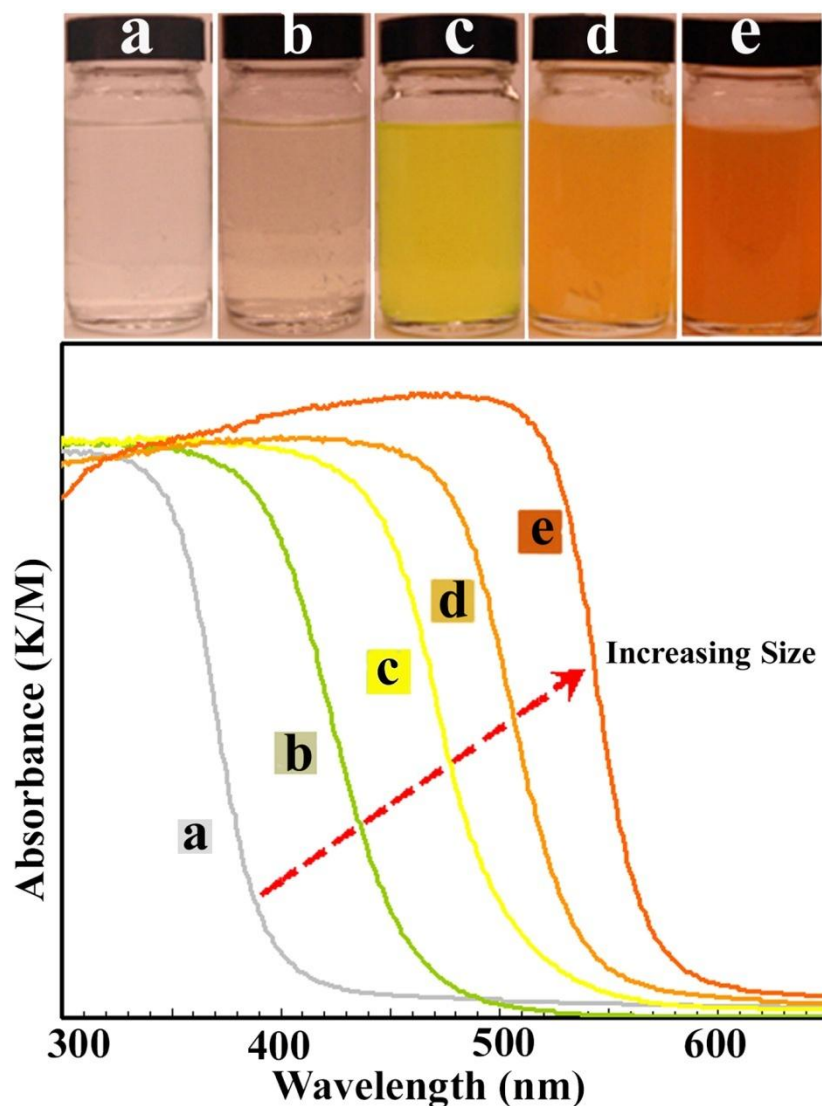


**Figure 4.6** Optical images and UV-Vis spectra of *E. coli*-templated CdS nanostructures in solution after (a) 0 min, (b) 1 min, (c) 10 min, (d) 2 h, and (e) 4 h of reaction.

As mentioned previously, the photocatalytic efficiency of CdS is dependent on its crystalline phase, with the hexagonal variant exhibiting the highest photocatalytic activity for hydrogen production under visible light irradiation.<sup>6, 10</sup> Thioacetamide is widely used as a sulfur source for the sonochemical synthesis of metal sulfides in the form of films, coatings, etc., because of its slow reaction rate with metal ions.<sup>36, 41</sup> In most reported studies the crystal structure of the materials has not investigated, including the case of bacteria-templated synthesis of CdS. We

have achieved precise control of the crystal phase of the hollow CdS microrods by adjusting the relative molar amount of sulfur in the reactants. Figure 4.7 shows the XRD patterns of three as-prepared microrod samples, with the crystal structure varying from pure hexagonal (Figure 4.7a, JCPDS card No. 41-1049), to a mixture of hexagonal and cubic (Figure 4.7b), to pure cubic phase (Figure 4.7c, JCPDS card No. 10-0454) by decreasing the sulfur/cadmium molar ratio. In general, the CdS precipitation reaction is rapid as long as sulfide ions are present in the solution since the CdS has a very small  $K_{sp}$ . The decomposition rate of thioacetamide is not expected to change under constant process conditions such as reaction temperature, pH value, and ultrasound power. Thus, for the synthesis at a high sulfur/cadmium molar ratio, we can either increase the concentration of thioacetamide so that a suitable amount of hydrogen sulfide is produced rapidly, or decrease the concentration of  $Cd^{2+}$ .

The crystal structure of the product depends sensitively both on its intrinsic stability and the growth environment. CdS has two common crystal structures (hexagonal and cubic) with the former being thermodynamically more stable. For hexagonal CdS the polar axis along the [001] direction is the preferred growth orientation, while cubic CdS grows preferentially along the [111] direction.<sup>42-43</sup> It should be noted that one hexagonal cell consists of at least two layers of  $CdS_4$  tetrahedra stacked along the [001] direction, while at least four tetrahedral layers are needed along the [111] direction to constitute one cubic cell. Furthermore, the binding energy of cubic CdS is lower than that of hexagonal CdS so that the cubic phase is not thermodynamically favored. In our synthesis, it is likely that the variations in the crystalline phase results from differences in the symmetry of the first coordination sphere of Cd with S in the thioacetamide and the corresponding growth conditions. A lower symmetry of the complex, in a low sulfur/cadmium molar ratio solution, favors the formation of cubic phase with growth along [111]

direction. In contrast, the formation of CdS with hexagonal structure is thermodynamically favored at higher sulfur/cadmium molar ratios. Thereby, during the initial stage, especially under non-equilibrium conditions affected by external conditions, crystal nuclei may develop into seeds in a preferable form (either low symmetry or high symmetry), resulting in the different crystalline phases in the products.

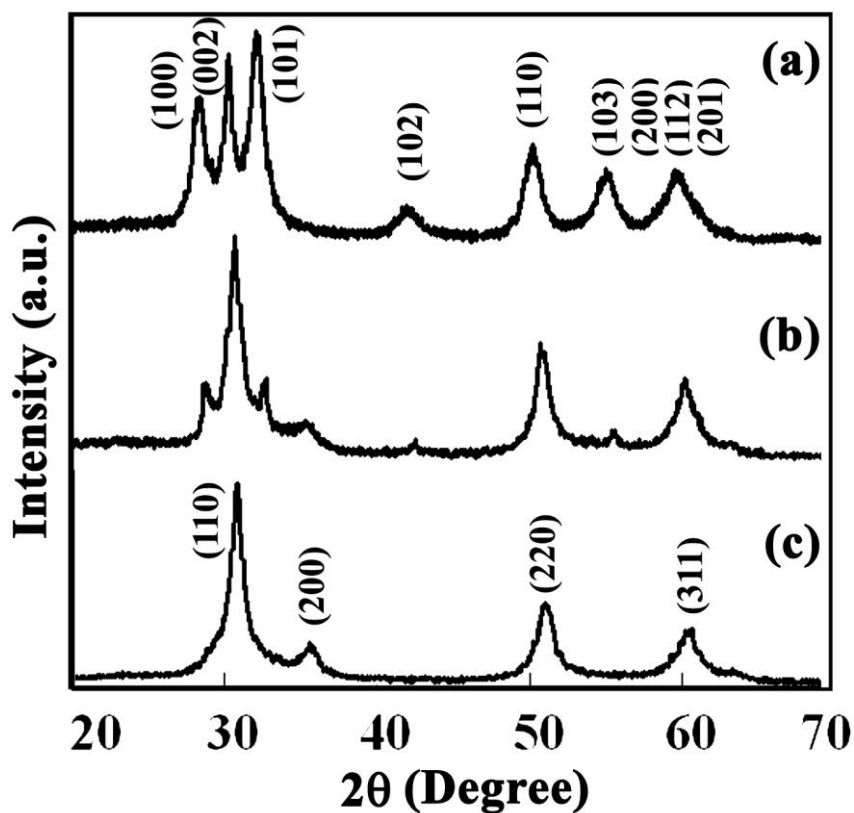


**Figure 4.7** XRD patterns of *E. coli*-templated CdS nanostructures with (a) hexagonal phase, (b) mixture of hexagonal and cubic phases, and (c) cubic phase, obtained with the sulfur/cadmium molar ratio at 2.5, 1, and 0.25, respectively.

We have tested the *E. coli*-templated nanoporous hollow CdS microrods as photocatalysts for hydrogen production. To investigate their photocatalytic activity, the as-synthesized CdS nanostructures with hexagonal phase was deposited in the form of a coating on an ITO-coated

glass substrate and annealed at 300 °C for 0.5 h. We have confirmed that the hollow microrod structure is retained after the annealing process (Figure 4.8). The photoelectrochemical properties of the fabricated CdS photoanodes are then measured in a 1 M Na<sub>2</sub>S-0.5 M Na<sub>2</sub>SO<sub>3</sub> electrolyte under global AM 1.5 illuminations with a conventional three-electrode system comprising a Ag/AgCl reference electrode and Pt foil counter electrode. From these measurements the photoconversion efficiency of light energy to chemical energy is calculated by using the photoelectrochemical cell efficiency, as has been reported previously.<sup>38-39</sup> A photoconversion efficiency of 4.33 % is obtained, as shown in Figure 4.9. This value is much higher than the 1.16 % efficiency obtained using CdS nanoparticles synthesized with the same procedure in the absence of *E. coli*. In our experiments, the light reflection and adsorption by the reactor wall and the reaction solution can result in an error or standard deviation for measurements of photoconversion efficiency, which usually accounts for minus 15 % error. In addition, the photoelectrochemical cell efficiency values vary depending on the errors and deviation involved in the assumptions and measurement procedures, such as the instruments' measurement deviation, the mismatch between the measured spectrum and the actual spectrum at the time of measurement, etc. As for the instruments and the measurement procedure used in the present work, a duplicate experiment showed good reproducibility for the photoelectrochemical cell efficiency measurement, and a standard deviation of less than 7 % for 5 repetitive measurements.

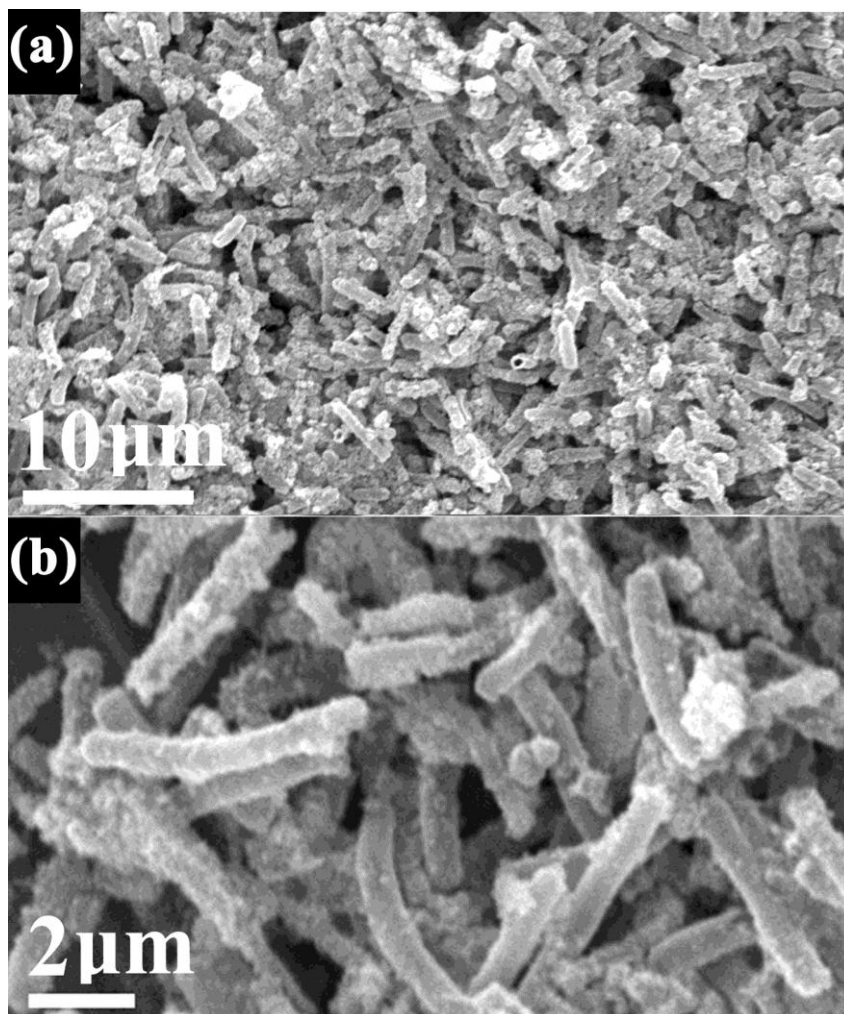


**Figure 4.8** (a) Low-magnification and (b) high-magnification SEM images of *E. coli*-templated hollow CdS microrods after annealing at 300 °C for 0.5 h.

The enhanced photoconversion efficiency in the case of the CdS microrods is attributed both to enhanced light absorption and fast electron-transfer due to the porous structure and thin rod wall thickness. Electron-transfer and electron/hole recombination are critical issues for photocatalytic applications of bulk materials. Nanopores in the hollow CdS microrods provide an ideal pathway for electron-transfer so that the ejected electrons can be transported rapidly to reduce recombination. This is similar to the transport process reported in CdS-coated TiO<sub>2</sub> nanotube array photoelectrodes in which photoexcited electrons can rapidly migrate to the TiO<sub>2</sub>

nanotubes, thereby decreasing the electron-hole recombination.<sup>38</sup> The likely reaction mechanism for photocatalytic hydrogen production over CdS in the presence of  $S^{2-}$  and  $SO_3^{2-}$  has been described previously.<sup>10</sup> Briefly, when a photon is absorbed by CdS on the photoanode in the presence of  $S^{2-}$  and  $SO_3^{2-}$ , an electron/hole ( $e^-/h^+$ ) pair is generated. The  $h^+$  can oxidize the adsorbed  $SO_3^{2-}$  and  $S^{2-}$  on the surface of the photoanode to form  $SO_4^{2-}$  and  $S_2^{2-}$ , while the  $e^-$  migrates to the Pt counter electrode and reduces water to form  $H_2$ .

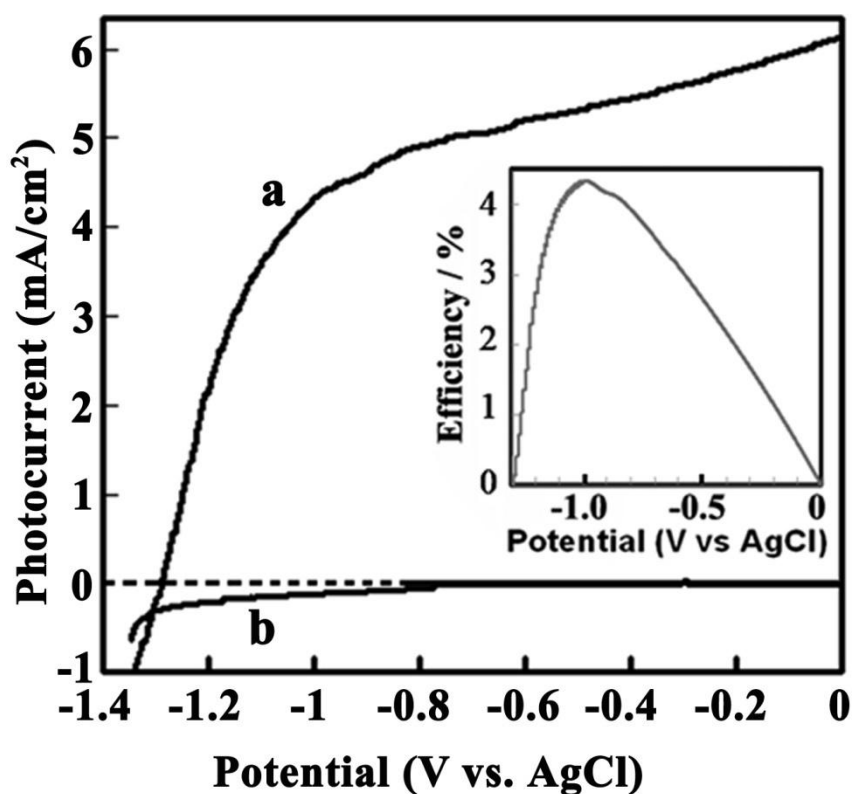


**Figure 4.9** (a) Photocurrent density (b) dark current, and corresponding photoconversion efficiency (the inset) of a photoelectrode fabricated using *E. coli*-templated nanoporous CdS hollow microrods with the hexagonal phase structure.

The simple synthetic strategy of using ethanol-treated *E. coli* as template has been extended to the preparation of other sulfide nanostructures, including PbS, HgS, and ZnS, as shown in

Figure 4.10. It is thus promising to use this method for synthesizing some mixed chalcogenide nanostructures with enhanced photoconversion efficiencies.

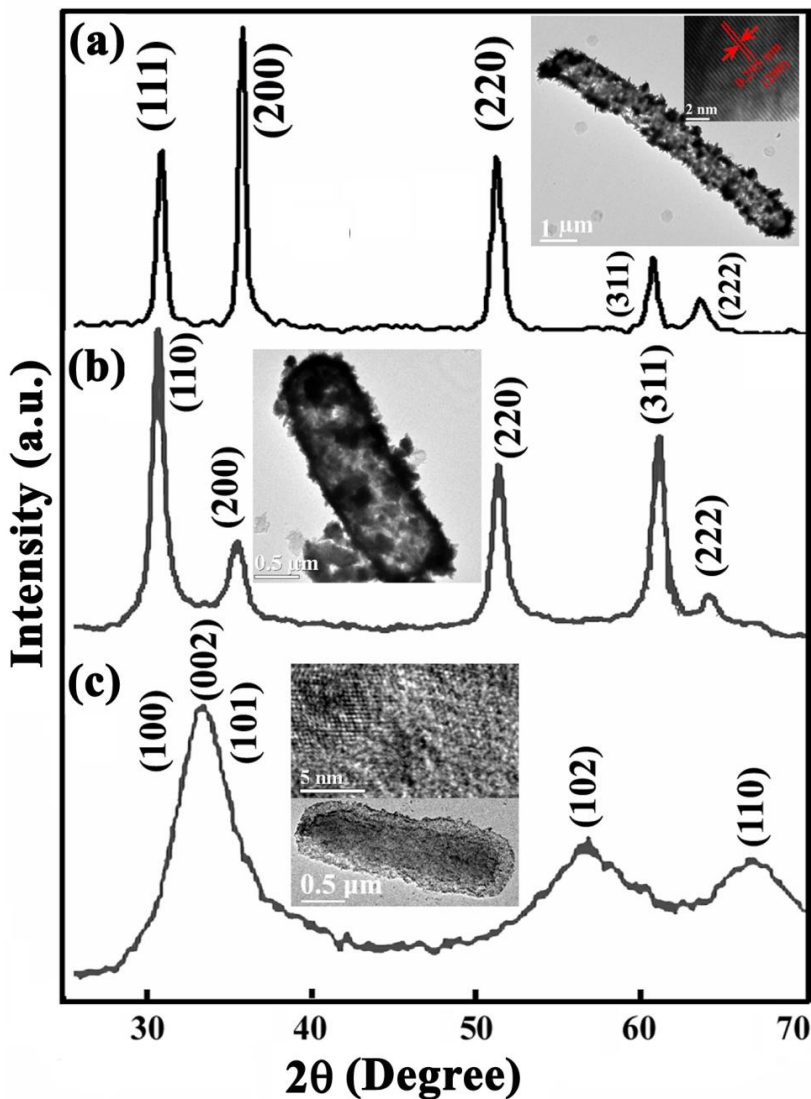


**Figure 4.10** XRD patterns and TEM images of *E. coli*-templated nanoporous hollow microrods of (a) PbS, (b) HgS, and (c) ZnS sonochemically synthesized after 4 h of reaction.

#### 4.4 Conclusion

In summary, we have used ethanol-treated *E. coli* bacteria as templates to promote controllable growth of nanoporous hollow CdS microrods via a simple sonochemical synthetic

method. The crystal phase, morphology, micro/nanostructure, optical absorption, and photocatalytic properties of the CdS nanostructures have been tailored over a wide range by simply changing the synthetic conditions, including the sulfur/cadmium molar ratio of the reactants, the reaction time, and the growth condition of *E. coli* bacteria. A significant improvement in the photoconversion efficiency has been achieved by utilizing the unique nanoporous hollow structures, resulted from the effective kinetic separation of photogenerated carriers. The facile synthesis procedure can be extended to the fabrication of other sulfides and core-shell nanostructures that will potentially lead to further improvements in the photoconversion efficiency. Controlled growth of semiconductor nanorod antennas utilizing the *E. coli* pili provides another avenue for increased efficiency by aiding in the energy harvesting process.

#### 4.5 References

1. Zong, X.; Yan, H.; Wu, G.; Ma, G.; Wen, F.; Wang, L.; Li, C. *J. Am. Chem. Soc.* **2008**, *130*, 7176-7177.
2. Tsuji, I.; Kato, H.; Kudo, A. *Angew. Chem. Int. Ed.* **2005**, *44*, 3565-3568.
3. Tsuji, I.; Kato, H.; Kobayashi, H.; Kudo, A. *J. Am. Chem. Soc.* **2004**, *126*, 13406-13413.
4. Nanu, M.; Schoonman, J.; Goossens A. *Nano Lett.* **2005**, *5*, 1716-1719.
5. Matsumura, M.; Saho, Y.; Tsubomura, H. *J. Phys. Chem.* **1983**, *87*, 3807-3808.
6. Bao, N.; Shen, L.; Takata, T.; Domen, K.; Gupta, A.; Yanagisawa, K.; Grimes, A. C. *J. Phys. Chem. C* **2007**, *111*, 17527-17534.
7. Kudo, A.; Kato, H.; Tsuji, I. *Chem. Lett.* **2004**, *33*, 1534-1539.
8. Arai, T.; Senda, S.; Sato, Y.; Takahashi, H.; Shinoda, K.; Jeyadevan, B.; Tohji, K. *Chem. Mater.* **2008**, *20*, 1997-2000.
9. Zheng, N.; Bu, X.; Vu, H.; Feng, P. *Angew. Chem. Int. Ed.* **2005**, *44*, 5299-5303.

10. Bao, N.; Shen, L.; Takata, T.; Domen, K. *Chem. Mater.* **2008**, *20*, 110-117.
11. Agrawal, M.; Pich, A.; Zafeiropoulos, N. E.; Gupta, S.; Pionteck, J.; Simon, F.; Stamm, M. *Chem. Mater.* **2007**, *19*, 1845-1852.
12. Chen, M.; Wu, L. M.; Zhou, S. X.; You, B. *Adv. Mater.* **2006**, *18*, 801-806.
13. Wang, Y.; Wang, G.; Wang, H.; Cai, W.; Zhang, L. *Chem. Commun.* **2008**, 6555-6557.
14. Du, N.; Zhang, H.; Chen, J.; Sun, J.; Chen, B.; Yang, D. *J. Phys. Chem. B* **2008**, *112*, 14836-14842.
15. Ahmad, J.; Dickerson, M. B.; Cai, Y.; Jones, S. E.; Ernst, E. M.; Vernon, J. P.; Haluska, M. S.; Fang, Y.; Wang, J.; Subramanyam, G.; Naik, R. R.; Sandhage K. H. *J. Am. Chem. Soc.* **2008**, *130*, 4-5.
16. Kisailus, D.; Truong, Q.; Amemiya, Y.; Weaver, J. C.; Morse, D. E. *Proc. Natl. Acad. Sci.* **2006**, *103*, 5652-5657.
17. Ma, N.; Dooley, C. J.; Kelley, S. O. *J. Am. Chem. Soc.* **2006**, *128*, 12598-12599.
18. Sharma, J.; Chhabra, R.; Andersen, C. S.; Gothelf, K. V.; Yan, H.; Liu, Y. *J. Am. Chem. Soc.* **2008**, *130*, 7820-7821.
19. Whaley, S. R.; English, D. S.; Hu, E. L.; Barbara, P. F.; Belcher, A. M. *Nature* **2000**, *405*, 665-668.
20. Prozorov, T.; Palo, P.; Wang, L.; Nilsen-Hamilton, M.; Jones, D.; Orr, D.; Mallapragada, S. K.; Narasimhan, B.; Canfield, P. C.; Prozorov, R. *ACS Nano* **2007**, *1*, 228-233.
21. Sanchez, C.; Arribart, H.; Guille, M. M. G. *Nat. Mater.* **2005**, *4*, 277-288.
22. Niemeyer, C. M. *Angew. Chem. Int. Ed.* **2001**, *40*, 4128-4158.
23. Zhang, S. *Nat. Biotechnol.* **2003**, *21*, 1171-1178.
24. Douglas, T.; Young, M. *Adv. Mater.* **1999**, *11*, 679-681.
25. Yoo, P. J.; Nam, K. T.; Qi, J.; Lee, S. K.; Park, J.; Belcher, A. M.; Hammond P. T. *Nat. Mater.* **2006**, *5*, 234-240.
26. Nam, K. T.; Kim, D.; Yoo, P. J.; Chiang, C.; Meethong, N.; Hammond, P. T.; Chiang, Y.; Belcher, A. M. *Science* **2006**, *312*, 885-888.

27. Nam, K. T.; Wartena, R.; Yoo, P. J.; Liau, F. W.; Lee, Y. J.; Chiang, Y.; Hammond, P. T.; Belcher, A. M. *Proc. Natl. Acad. Sci.* **2008**, *105*, 17227-17231.
28. Vriezema, D. M.; Aragonés, M. C.; Elemans, J. A. A. W.; Cornelissen, J. J. L. M.; Rowan, A. E.; Nolte, R. J. M. *Chem. Rev.* **2005**, *105*, 1445-1489.
29. Mandal, D.; Bolander, M. E.; Mukhopadhyay, D.; Sarkar, G.; Mukherjee, P. *Appl. Microbiol. Biotechnol.* **2006**, *69*, 485-492.
30. Levinson, W. E. in *Review of Medical Microbiology & Immunology*, Tenth Ed., McGraw-Hill Companies, Inc. New York, 2008.
31. Sweeney, R. Y.; Mao, C.; Gao, X.; Burt, L. L.; Belcher, A. M.; Georgiou, G.; Iverson, B. L. *Chem. Biol.* **2004**, *11*, 1553-1559.
32. Kang, S. H.; Bozhilov, K. N.; Myung, N. V.; Mulchandani, A.; Chen, W. *Angew. Chem. Int. Ed.* **2008**, *120*, 5264-5267.
33. Mehra, R. K.; Winge, D. R. *J. Cell Biochem.* **1991**, *45*, 30-40.
34. Vido, K.; Spector, D.; Lagniel, G.; Lopez, S.; Toledano, M. B.; Labarre, J. *J. Biol. Chem.* **2001**, *276*, 8469-8474.
35. Zhou, H.; Fan, T.; Zhang, D.; Guo, D.; Ogawa, H. *Chem. Mater.* **2007**, *19*, 2144-2146.
36. Cassler, M. R.; Grimwade, J. E.; McGarry, K. C.; Mott, R. T.; Leonard, A. C. *Nucl. Acids Res.* **1999**, *27*, 4570-4576.
37. Dhas, N. A.; Zaban, A.; Gedanken, A. *Chem. Mater.* **1999**, *11*, 806-813.
38. Sun, W. T.; Yuan, Y.; Pan, H. Y.; Gao, X. F.; Chen, Q.; Peng, L. M. *J. Am. Chem. Soc.* **2008**, *130*, 1124-1125.
39. Tak, Y.; Hong, S.; Lee, J. S.; Yong, K. *J. Mater. Chem.* **2009**, *19*, 5945-5958.
40. Beard, J.; Howe, T.; Richmond, M. *J. Bacteriol.* **1972**, *111*, 814-820.
41. Gao, T.; Li, Q.; Wang, T. *Chem. Mater.* **2005**, *17*, 887-892.
42. Yong, K.; Sahoo, Y.; Swihart, M. T.; Prasad, P. N. *J. Phys. Chem. C* **2007**, *111*, 2447-2458.
43. Chen, M.; Kim, Y. N.; Li, C.; Cho, S. *Cryst. Growth Des.* **2008**, *8*, 629-634.

## CHAPTER 5

### SUMMARY AND FUTURE PLAN

We have identified CdS- and TiO<sub>2</sub>-binding peptides using the phage display biopanning technique and analyzed the specific binding affinity between organic groups of the amino acids and inorganic components based on their chemical and physical properties. The CdS-binding peptides show preference for positively charged R groups that competitively attach to the surface of CdS substrate (cleaned using diluted HCl) through electrostatic interaction with the exposed S ions. Furthermore, proline (P) groups in these peptides cause kinks in the chain, enabling the functional amino acids to approach closer to the substrate surface than possible without their presence. Single crystal rutile TiO<sub>2</sub> substrates possess crystalline defects on the surface even after cleaning and the surface of TiO<sub>2</sub> substrate can be easily hydrolyzed in aqueous solutions. Amino acids with polar uncharged R groups and positively charged R groups thus can bind to the hydroxyl groups on the surface of TiO<sub>2</sub> substrates through hydrogen bonds. Furthermore, these functional amino acids tend to be spaced apart in the dominant sequence so as to offer a good match with the crystal structure of the TiO<sub>2</sub> substrate. The recognition ability of CdS-specific peptides to the substrate has been examined with the aid of labeled antibodies. The successful growth of CdS nanowires over genetically engineered M13 phages indicates that the selected peptides can be engineered onto other organisms to template various architectures with desired components.

As a demonstration, we have fabricated ordered nanostructures of sulfide nanocrystal assemblies over self-assembled genetically engineered P22 coat proteins. This biotemplated construction involves two steps: (1) the self-assembly of spherical protein templates from

genetically engineered P22 coat proteins; and (2) the nucleation and growth of nanocrystals on the self-assembled protein templates. The high-affinity ZnS- and CdS-binding peptides identified by phage display biopanning enable selective nucleation and growth of sulfides over self-assembled genetically engineered P22 coat proteins. The structure and morphology of the protein-directed sulfide growth can be suitably controlled by changing the reaction time and reactant concentration. For example, ordered spherical nanocrystal assemblies are formed during the early stage of growth that eventually develop into spherical hollow nanostructures for longer growth periods. We have used ZnS and CdS grown on the engineered P22 coat protein assembly as a model system since binding peptides with strong affinity for these sulfides have previously been identified. Furthermore, the structure and assembly of the P22 coat proteins is reasonably well understood. The synthetic strategy is quite general and can be extended to the fabrication of a variety of other nanostructures.

Finally, we have developed a simple sonochemical route for the synthesis and assembly of CdS nanostructures with a high yield under ambient conditions by exploiting the chemical characteristics and structure of permeabilized *E. coli* bacteria. The novelty of the method lies in the use and modification of *E. coli* for the templating growth of CdS with controllable material properties. The crystal phase, morphology, micro/nanostructure, optical absorption, and photocatalytic properties of the CdS nanostructures have been tailored over a wide range by simply changing the synthetic conditions, including the sulfur/cadmium molar ratio of the reactants, the reaction time, and the growth condition of *E. coli* bacteria. Photoanodes fabricated using the nanoporous hollow CdS microrods of hexagonal structure exhibit an excellent performance for the photocatalytic hydrogen production; with a maximum photoelectrochemical cell efficiency of 4.33 % under global AM 1.5 illumination. The significant improvement in the

photoconversion efficiency can be attributed to the effective kinetic separation of photogenerated carriers through the unique nanoporous hollow structures. This facile synthesis procedure can be readily extended to the fabrication of other sulfides and core-shell nanostructures that will potentially lead to further improvements in the photoconversion efficiency.

To date, most of the materials that have been synthesized via virus- and protein-templated approaches are restricted to simple binary compounds such as ZnS, CdS, CoO, CoPt, FePt, etc. These materials have low solubility product constants and can thus be synthesized in solutions using relatively simple chemistry from stable precursors under ambient conditions. The synthesis of more complex multi-component photocatalyst materials, such as heterogeneous nanostructures of quantum dot sensitized TiO<sub>2</sub> nanocrystals, is likely to be more challenging and remains to be explored. In the future, we plan to use P22 as a platform to prepare a wide range of semiconductor nano-architectures utilizing both the interior and exterior of the protein cages. A single P22 procapsid contains 420 copies of the P22 coat protein and 300 copies of the scaffolding protein (described in Chapter 3, 3.3 Fabrication of Ordered Nanostructures of Sulfide Nanocrystal Assemblies over Self-Assembled Genetically Engineered P22 Coat Protein). Our preliminary data indicates that scaffolding-GST fusion proteins can polymerize onto procapsid particles. This indicates that it is possible to build procapsids with altered scaffolding proteins. Consequently, specific peptide sequences responsible for binding to different materials can be engineered onto coat proteins and scaffolding proteins. A possible nanoarchitecture built on a single P22 bacteriophage is shown in Figure 5.1. The unique recognition peptides on the interior and exterior surface of the genetically engineered protein cage can be exploited not only for the nucleation of light harvesting semiconductor nanocrystals, but also preferentially direct the growth of a specific crystal type and orientation, and possibly stabilize metastable phases.

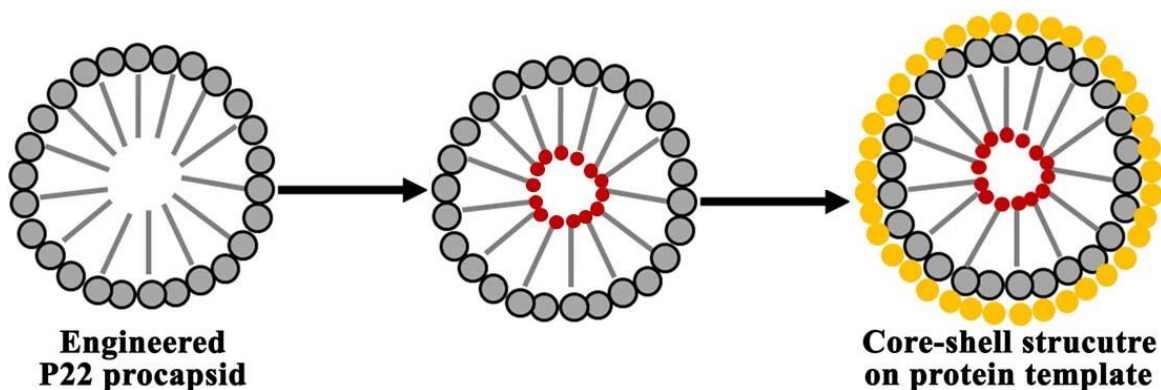


**Figure 5.1** A schematic core-shell nanostructure grown over the genetically modified P22 procapsid.

CdS(Se) are narrow band gap materials with desirable band structures for the water splitting under visible light irradiation. PbS(Se) have the optical absorption wavelengths extending to the infrared wavelength and also offer the possibility of multiple exciton generation for single photon absorption that can result in much improved quantum efficiencies. All these chalcogenides can be used as sensitizers to enhance the conversion efficiency of sun light over  $\text{TiO}_2$ , a well-known wide bandgap semiconductor. We plan to engineer P22 coat protein with specific peptide sequences responsible for binding to sulfide materials with efficient absorption in the visible, while  $\text{TiO}_2$ -binding peptides engineered onto the scaffolding proteins. Thus, core-shell nanostructures with multi-component can be prepared on P22 after biomineralization. For practical applications, these core-shell nanostructures will be prepared in the form of monolayered or multilayered films, as depicted in Figure 5.2 (each unit of the assembly is one nanostructure shown in Figure 5.1). We can use different methods such as spin coating, dip coating, or evaporation induced self-assembly to prepare these films on different substrates. The size and thickness of the films will be controlled by adjusting the process parameters. Alternatively, specific peptides will be conjugated with other structural linkers (peptides or nucleic acids) to form self-assemblies of multi-dimensional nanoarchitectures. Interval distance

amongst individual nanostructures can be controlled by varying the chain length of peptides or nucleic acids. Both the protein template for the core-shell structure and the linker can subsequently be removed by a heat treatment to prepare a well-dispersed catalyst efficiently coupled to a light harvesting semiconductor matrix.

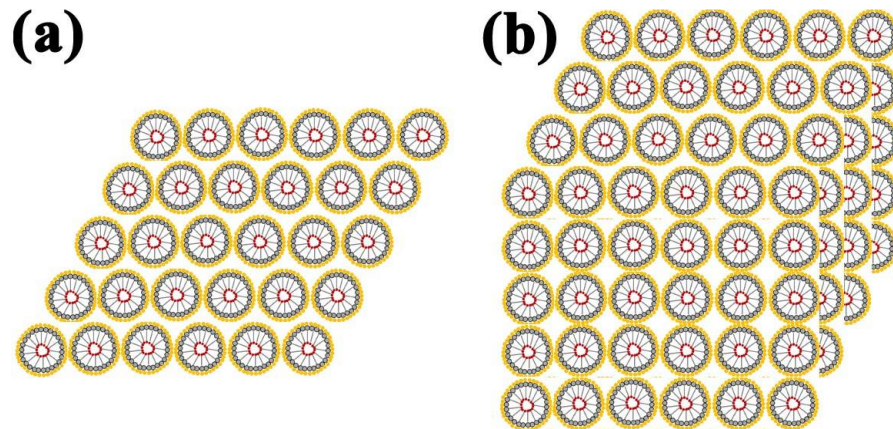


**Figure 5.2** (a) Monolayered and (b) multilayered films of the core-shell nanostructures grown over the genetically modified P22 procapsid.